

**Ultra-Compliant Transverse Intrafascicular Electrode Arrays  
for Electro-Pharmaceutics**

*Final Report*

Reporting Period: 31 March 2015 – 31 March 2017

Sponsored by  
Defense Advanced Research Projects Agency (DARPA)  
Microsystems Technology Office  
ElectRx Program [Seedling]

Issued by  
Defense Advanced Projects Agency (DARPA)  
Contracts Management Office under  
Cooperative Agreement No. HR0011-15-2-0009

Technical Agent:  
U.S. Navy  
Space and Naval Warfare Center (SPAWAR)

Name of Grantee: Carnegie Mellon University  
Principal Investigator: Gary K. Fedder  
Business Address: 5000 Forbes Ave., Pittsburgh, PA 15213-3890  
Phone Number: (412) 268-8443  
Effective Date of Grant: 31 March 2015  
Grant Expiration Date: 31 March 2017

Distribution unlimited. Fundamental research exempt from prepublication controls.

**DISCLAIMER**

The views and conclusions contained in this document are those of the authors and should not be interpreted as representing the official policies, wither expressed or implied, of the Defense Advanced Projects Agency, the U.S. Navy, or the U.S. Government.

**DESTRUCTION NOTICE**

For unclassified documents, destroy by any method, which precludes reconstruction of the document.

## Contents

Ultra-Compliant Transverse Intrafascicular Electrode Arrays for Electro-Pharmaceutics	1
1 Project Description .....	1
2 Task 1.1 – Electrical Impedance Stability .....	2
2.1 Objectives .....	2
2.2 Accomplishments .....	2
2.3 Assessment .....	3
3 Task 1.2 – Needle Micromolding and Insertion .....	3
3.1 Objectives .....	3
3.2 Accomplishments .....	4
3.3 Assessment .....	4
4 Task 1.3 – Single Recording Probes.....	5
4.1 Objectives .....	5
4.2 Accomplishments .....	5
4.3 Assessment .....	6
5 Task 2.1 – Single Stimulation Probes.....	6
5.1 Objectives .....	6
5.2 Accomplishments .....	7
5.3 Assessment .....	8
6 Task 2.2 – Multi-Probe Array .....	8
6.1 Objectives .....	8
6.2 Accomplishments .....	9
6.3 Assessment .....	9
7 Project Results.....	9
7.1 Probe design .....	9
7.1.1 Single probe design .....	9
7.1.2 Probe stress modeling.....	10
7.1.3 Multi-probe design .....	12
7.1.4 Insulation test structure design .....	12
7.1.5 Probe crosstalk modeling .....	14
7.2 Probe fabrication processes .....	17
7.2.1 Parylene fabrication process.....	17

7.2.2	ALD ceramic thin-film encapsulant processes.....	19
7.2.3	Electrode fabrication .....	24
7.2.4	Iridium oxide electrodes .....	25
7.2.5	Protruding electrodes.....	27
7.2.6	Probe transfer process.....	31
7.3	Silicon surrogate probe.....	36
7.4	Electrical stability studies.....	38
7.4.1	Lumped-element impedance modeling .....	38
7.4.2	Finite-element impedance modeling .....	40
7.4.3	Electrochemical Impedance Spectroscopy setup.....	42
7.4.4	Insulation leakage tests at 0.1 Hz .....	42
7.4.5	Wiring insulation impedance at 1 kHz .....	45
7.4.6	High temperature testing .....	46
7.4.7	High voltage insulation tests .....	49
7.4.8	Electrode impedance tests .....	51
7.4.9	Iridium oxide stimulation electrode tests.....	51
7.4.10	Protruding electrode impedance tests .....	53
7.4.11	<i>In vitro</i> probe insulation and impedance tests .....	55
7.5	Bio-dissolvable needles .....	57
7.5.1	Needle material mechanical properties.....	57
7.5.2	Needle-probe molding process .....	59
7.5.3	Needle-probe assembly .....	63
7.5.4	Insertion into agarose phantom .....	69
7.5.5	Insertion into sciatic nerve tissue .....	72
7.5.6	Experimental force modeling .....	79
7.5.7	Vibration assisted insertion .....	83
8	Conclusions .....	85
9	Patents and Invention Disclosures.....	86
10	Publications .....	86
10.1	Journal papers.....	86
10.2	Thesis.....	86
10.3	Conference Papers .....	86



## 1 Project Description

The project is an advanced study to create ultra-compliant thin-film transverse intrafascicular multi-channel electrodes that interface locally and intimately to fascicles in the peripheral nervous system (PNS), specifically targeting the human vagus nerve. The final goal is to provide a coupled design and fabrication technology for PNS multi-probe arrays that supports both recording and stimulation, is selective to specific fascicles, is scalable in electrode count and location to cover the entire cross section of major branches of the vagus nerve, has low invasiveness after insertion relative to competing intrafascicular probes, and whose functionality is validated through *in vitro* and *ex vivo* testing. The overall concept is depicted in Figure 2.

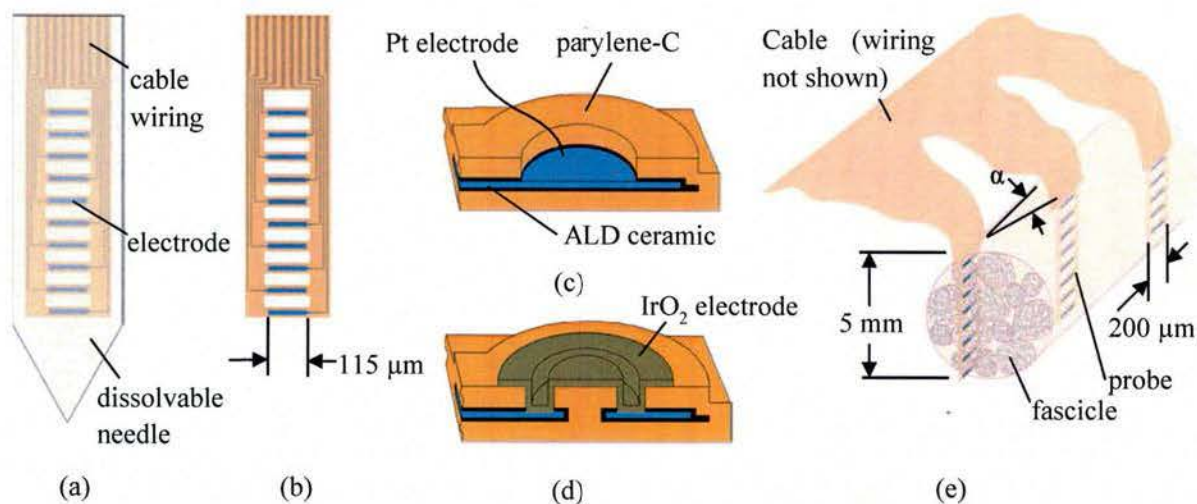


Figure 1. Canonical probe design. (a) Single probe with micromolded needle with 10 electrodes (or 8 possible tri-poles). (b) Single probe without needle. (c) "Regular" platinum electrode. (d)  $\text{IrO}_2$  protruding electrode. (e) Probe array inserted into a nerve at a slight angle  $\alpha$  to the nerve axis.

The project is partitioned into five major tasks (T) over two one-year phases (P), with numbering syntax "P.T":

- 1.1) Electrical impedance stability studies, where characterization of leakage and electrode impedance occurs for probes and surrogate test structures;
- 1.2) Needle micromolding and insertion studies, where development of materials and processes for creation of sharp, bio-dissolvable needles occurs, along with methods for insertion into tissue and phantom tissue;
- 1.3) Single recording probes, where development of processes for creation of parylene probes with platinum (Pt) electrodes and ceramic insulation occurs;
- 2.1) Single stimulation probes, where further development of processes for creation of parylene probes with iridium oxide ( $\text{IrO}_2$ ) and protruding electrodes occurs; and
- 2.2) Multi-probe array, where design and development of multi-shank probes and corresponding needle arrays occurs.



The first sections of this report describe the objectives and accomplishments of each major task, along with a short assessment comparing the accomplishments to the original goals of the project. The bulk of the remainder of the report is a "Project Results" section that provides details of the completed work, spanning a) probe design and fabrication processes, b) *in vivo* validation of parylene probe function with a surrogate silicon needle, c) electrical leakage, electrode impedance, and electrode stimulation studies, and d) needle design, fabrication, attachment, and insertion methods.

## **2 Task 1.1 – Electrical Impedance Stability**

### **2.1 Objectives**

Design, fabrication and measurement of thin-film test structures allows validation and quantification of wiring and electrode electrical impedance performance over different encapsulation enclosure schemes. Parylene-C is the preferred encapsulating material, with embedded platinum wires. Encapsulation exploration includes thin-film alumina, along with other ceramic films once alumina was proven unsuitable. Long-term leakage and impedance tests of nominally six-month duration in both 37°C and 60°C normal saline environments provide an assessment of the probe durability. The task has three measurable objectives:

- 1) To quantify electrical leakage for wiring with and without alumina encapsulation by performing short-term experimental measurements of the low-frequency impedance (i.e., resistance) of insulated wiring versus time. The target for leakage resistance is greater than 1 G $\Omega$  for specific wiring insulator designs.
- 2) To quantify electrode impedance stability by performing short-term experimental measurements of electrical impedance versus time for suitable insulators that meet the first objective. The target electrode impedance stability at 1 kHz is to change less than 5% with respect to an initial reference impedance over a 12 hour duration for specific designs.
- 3) To quantify mean time to failure for wiring completely encapsulated by alumina and parylene-C by performing long-term electrical leakage and impedance tests.

### **2.2 Accomplishments**

- 1) We successfully fabricated electrode test structures to measure the ability of parylene-C encasement and alumina encasement as electrical insulators. While individually other groups have tested these insulating materials for feasibility, this is the first quantitative measurement to our knowledge of alumina-encased thin film wiring with subsequent parylene-C encasement.
- 2) Sealing at the interface of parylene-C to parylene-C layers requires 300°C annealing, validating earlier work in the literature. Careful attention to cleaning after etch processes prior to application of the second parylene-C layer is important to seal the parylene-C (see Task 1.3).
- 3) The alumina encasement around wiring results in greater than 5 G $\Omega$  leakage resistance that is stable in phosphate buffered saline (PBS) for 520 h (>21 days). However, in both short and long-term tests, alumina encapsulation resulted in more rapid degradation of impedance of the insulation in PBS than simply having parylene encapsulation alone. We believe this is due to two issues: 1) the adhesion of alumina to parylene is relatively poor and 2) alumina etches in PBS.

- 4) The negative findings of the alumina tests inspired exploration of atomic layer deposition (ALD) of alumina/titania nanolaminate for sealing. This work is the first nanolaminate encasement of neural probe wiring. Both parylene-C encapsulated wiring and nanolaminate-encapsulated parylene-C wiring with or without TiO<sub>2</sub> adhesion layer provide greater than 1 GΩ leakage resistance after 5000 h.
- 5) Electrical impedance change is less than 5% over 500 h periods on electrodes with parylene-C encapsulated wiring and on electrodes with nanolaminate-encapsulated parylene-C wiring.
- 6) We completed six-month testing of wiring and electrodes with parylene-C, alumina, titania, and nanolaminate encasement as insulator options. The parylene-Pt-parylene test structures have the best performance at room temperature with impedance above 10 GΩ that gradually decreases with an exponential time constant of 6.6 months (measured over 6 months). However, the parylene-Pt-parylene structures have poor performance at 60°C. These accelerated long-term aging tests indicate that anomalous failure modes occur that are not present when operating at body temperature. Performance is also poor in the few samples of released probes made to date, though that may be due to micro-cracking.
- 7) Nanolaminate coatings with the titania adhesion layer were tested to 5000 h in test structures where the titania is removed between wiring to eliminate residual resistive paths. The results indicate lower impedance at 0.1 Hz than the parylene only structures; however, the impedance is adequately high (>5 GΩ) for probe applications, and it is capacitive not resistive. The most important motivation for the NL-TiO<sub>2</sub> encapsulation is for higher voltage stimulation, which will not tolerate any resistive leakage.
- 8) Exploration of ALD TiO<sub>2</sub> alone as a sealing layer validated that it does not etch in PBS and it has excellent adhesion to parylene and to platinum. However, titania has a finite conductivity, albeit small compared to platinum, which results in it being a poor choice for electrical insulation in neural probes.

## 2.3 Assessment

Successful completion of the intended short-term and long-term electrical leakage and impedance tests led to meeting all of the original objectives. The effort explored well beyond the original proposed plan, uncovering a novel application for titania/alumina nanolaminate insulation.

## 3 Task 1.2 – Needle Micromolding and Insertion

### 3.1 Objectives

The primary objective is the validation of biocompatible dissolvable needle materials by assessing performance *in vitro* and *ex vivo* for appropriate dissolution time and mechanical strength for insertion into the epineurium of peripheral nerves. Needle designs appropriate for use with the probes mate with suitable micromolding techniques to enable their fabrication. Development and analysis of vibration-assisted needle insertion may provide for lower insertion force into nerve tissue. The task has these measurable objectives:

- 1) To measure the elastic and failure characteristics of candidate dissolvable material combinations of carboxymethylcellulose (CMC) and sugars (e.g., glucose, sucrose, dextrose). Needle materials properties to characterize are elastic modulus, yield stress, and ultimate strength.



- 2) To quantify dissolution rates for candidate materials and corresponding needles from timed *in vitro* insertion tests in a tissue phantom in order to provide more information for best needle material selection.
- 3) To quantify the necessary needle insertion force and validate successful insertion from *in vitro* needle insertion tests in a tissue phantom and from *ex vivo* insertion tests in nerve tissue.
- 4) To design a vibration-assisted insertion device, to identify associated optimal conditions and needle geometries, and to quantify corresponding insertion force through *in vitro* needle insertion tests in a tissue phantom and from *ex vivo* insertion tests in nerve tissue. The goal is to demonstrate significant reduction on insertion forces and a higher factor of safety for needle insertion.
- 5) To create a computational model for vibration assisted needle insertions into tissues, with validation from insertion force data from the experiments in this task.

### 3.2 Accomplishments

- 1) Measured mechanical properties of five prospective material combinations of CMC and sugar provided guidance for choosing the best material for bio-dissolvable needles. Material stress-strain curves for all potential CMC/sugar alloys indicate that an 85% CMC / 15% glucose combination is the best material for use in needle formation. The CMC/glucose has the highest geometric fidelity and suitable hardness.
- 2) Agarose acts as a suitable *in vitro* model for insertion of bio-dissolvable needles. PDMS and PVS as a surrogate model do not allow for dissolution of the needle. Lower insertion velocities lead to lower average forces but higher damage in the agarose.
- 3) Load-deflection insertion tests of surrogate needles into agar indicate geometric factors (needle-tip shape and shank shape) for best needle mold geometry. The needle-tip type (wedge vs. point, along with the tip angle(s)) greatly influences the insertion force, based on observations of needles inserted into *ex vivo* tissue (fresh goat sciatic nerve). Very sharp 3D shaped tips are successful and are required for insertion into nerve tissue.
- 4) A trial CMC/glucose needle with a 10-electrode probe inserted successfully into goat sciatic nerve tissue. Wire imaging with a nanoscale x-ray computer tomographic (Nano-CT) system verifies the successful mechanical insertion.
- 5) Vibration assisted needle insertion, to date, did not result in a reduction in insertion force nor in a reduction in damage.

### 3.3 Assessment

Successfully completed objectives include measurement of needle materials properties, dissolution rates and insertion forces. Partial completion of the vibration insertion studies show no substantial benefit in use of vibration for needle insertion; the team did not have continued time and resources to follow up with improved vibration testbed for insertion to collect further data. Needle design and fabrication took more effort in phase 1 than anticipated; as a result, the team decided not to pursue a computational model for vibration assisted needle insertion. We estimate that development of a computational model, using finite-element analysis, requires several months of PhD-level effort at a minimum.



## 4 Task 1.3 – Single Recording Probes

### 4.1 Objectives

The objective of this task is the design and fabrication of thin-film single-shank (“single”) neural probes with transverse intrafascicular multi-channel electrodes. The work leverages past efforts in our group on cortical probes using batch microfabrication techniques with thin-film platinum electrodes and wiring. Best practices learned from the Electrical Impedance Stability Study in task 1.1 drives the choice of materials and design rules for encapsulation and electrical insulation. The designed probes mate with bio-dissolvable needles from task 1.2. The task has three main objectives:

- 1) To design and fabricate single-shank recording probes with over 50% functional yield.
- 2) To obtain stability of probe electrode impedance at 1 kHz with changes of less than 5% with respect to an initial reference impedance over a 12-hour duration in short-term electrical impedance tests.
- 3) To demonstrate successful insertion with retention of the probe inside the medium, as observed from *in vitro* needle insertion tests in an agarose tissue phantom and from *ex vivo* insertion tests in nerve tissue.

### 4.2 Accomplishments

- 1) The single-shank recording probe design evolved to accommodate high-yield fabrication. The reference design has ten electrodes placed equal distances apart with curved outlines throughout to reduce mechanical stress concentration points. Design guidelines were formed for ALD nanolaminate (NL) encapsulation.
- 2) The fabrication process for the single-shank recording probe evolved in parallel with the design. Highlights include the ALD NL development, cleaning of platinum electrodes for lower impedance, parylene fusion at 300°C, and dry chlorine-based plasma etching of the NL enabling better parylene fusion.
- 3) A revision to the nanolaminate patterning step substituted a dry Cl<sub>2</sub> ICP-RIE etch for the wet hydrofluoric (HF) acid etch. The HF acid left residue on the parylene surface, which compromised the ability of the later 300°C anneal to seal the parylene. Results from the long-term leakage test with the dry-etched samples indicate similar leakage performance to parylene alone.
- 4) O<sub>2</sub> reactive-ion etch to etch parylene-C, the state-of-the-art method for processing parylene-C, oxidizes a surface layer of platinum, which results in high electrochemical impedance of the exposed platinum electrodes. By introducing an Ar<sup>+</sup> ion-milling step, the electrochemical impedance of the electrode reduces by an order of magnitude. The measured surface roughness (Ra) of the electrodes using this method of de-insulation is 13.1 nm.
- 5) The ALD NL with interspersed layers of TiO<sub>2</sub> and Al<sub>2</sub>O<sub>3</sub> succeeded in suitably encapsulating the platinum wiring with a near-hermetic ceramic coating. The titanium layers keep the alumina from etching in saline, while the alumina layers maintain an overall electrically insulating property (as titania has a finite electrical conductivity).
- 6) We achieved a breakthrough in the overall probe release process by adding an intermediate release and transfer step prior to needle attachment. An issue we had to surmount was that the 300°C parylene-C anneal simultaneously created excellent adhesion of the probe to the silicon substrate. The adhesion was so great that the probe would not detach after the micromolding

step. Compatibility of needle attachment to the probes required transfer of the fabricated probes from the silicon substrate to an intermediate substrate. A new process using a liquid wax (BGL7080, AI Technology Inc., Princeton Junction, NJ) as a transfer adhesive achieves the necessary conditions for process compatibility with the bio-dissolvable needle material. BGL7080 proved to be the best intermediate adhesive material choice, after parallel exploration of several other candidate intermediate adhesive materials. The overall transfer process result yields over 75%.

- 7) Measured electrode impedance at 1 kHz changes less than 5% after 16 h for a 10  $\mu\text{m}$ -thick parylene-platinum probe with a bonded needle.
- 8) Nano-computer tomography images of the probe in agarose medium show that the probe is successfully delivered using a CMC/glucose needle.
- 9) Prof. Aryn Gittis' group at CMU inserted a parylene-platinum probe connected to an integral silicon shank (in place of a CMC/glucose needle) 4 mm deep in a mouse brain to validate neural signal pickup in an acute measurement setup and performed through independent Gittis Lab research funding and animal protocol. The probe successfully picked up neural spikes, establishing the viability of the parylene-platinum process flow.

### **4.3 Assessment**

The project met all of the original objectives for this task. ALD alumina originally proposed for encapsulation etched in saline, so exploration of other ALD material combinations led to adoption of the  $\text{TiO}_2/\text{Al}_2\text{O}_3$  nanolaminate as a successful solution. The originally proposed direct micromolding of needles onto the probes resulted in low yield, and subsequent development of the probe transfer process led to a high yield solution.

## **5 Task 2.1 – Single Stimulation Probes**

### **5.1 Objectives**

The objective of this task is the design and fabrication of thin-film single-shank (“single”) neural probes with transverse intrafascicular multi-channel stimulating electrodes. Best practices learned from the Single Recording Probes task 1.3 drive the choice of process and materials, with the addition of stimulating electrodes made of thin-film iridium/iridium oxide and electrodes protruding from the probe surface. Stimulation/impedance characterization stems from long-term tests of nominally six-month duration conducted in both 37°C and 60°C normal saline environments. The task has four main objectives:

- 1) To design and fabricate single-shank stimulation probes with over 50% functional yield.
- 2) To obtain stability of probe electrode impedance at 1 kHz with changes of less than 5% with respect to an initial reference impedance over a 12-hour duration in short-term electrical impedance tests.
- 3) To quantify charge injection capacity with a target of greater than or equal to 2  $\text{mC}/\text{cm}^2$ .
- 4) To quantify mean time to failure through long-term stimulation/impedance testing.



## 5.2 Accomplishments

- 1) Design and fabrication of single-shank stimulation probes follow the successful design and process flow of the recording probes, with an additional electrode layer of iridium/iridium oxide.
- 2) Motivation for the effort to design and fabricate protruding electrodes came from a hypothesis of improved neural connection to the surrounding tissue. Iterations in the design of protruding electrodes led to adoption of a ring-shaped platinum electrode base that enables the parylene-C protrusion to fuse with the underlying parylene layer, thus locking it into place. This avoids the risk of insufficient adhesion of the parylene deposited directly on top of platinum. However, samples inserted in room temperature saline for 2 months did not show any delamination in either case. A subsequent iridium oxide deposition creates the protruding electrode with connection to the platinum wiring. The design modification to form parylene protruding electrodes was successful, leading to protrusions of 1.4  $\mu\text{m}$ , equal to the thickness of the second parylene layer. Impedance tests of parylene protruding electrodes indicate the impedance is about four times smaller than without protrusions.
- 3) A two-layer platinum wiring process enables the protruding base for the iridium electrode and eliminates the need for thick iridium deposition, which is more expensive than platinum. Interconnects in the two-layer platinum process indicate successful connection of vias that connect the two layers.
- 4) The stimulation electrode impedance is stable after iridium oxide activation, as demonstrated on test structures.
- 5) Deposition of iridium oxide produced working electrodes; after C-V cycling to activate the  $\text{IrO}_2$ , the charge storage capacity (CSC) increases to around 0.5  $\mu\text{C}$  for 50  $\mu\text{m}$  by 50  $\mu\text{m}$  test electrodes, which is around the size of the 115  $\mu\text{m}$  by 15  $\mu\text{m}$  probe electrodes. The charge injection capacity (CIC) reached 2  $\text{mC}/\text{cm}^2$  after activation for 25  $\mu\text{m}$  by 25  $\mu\text{m}$  electrode.
- 6) Test structures show long-term stability in simulated stimulation conditions with 1 V peak-to-peak applied.
- 7) The probe-transfer process relieves significant stress compared to direct micromolding of the needle onto the probe. However, manual procedures in needle bonding result in microcracking of parylene and of platinum wiring in selective locations, believed due to shear stress during manual attachment of the needle to the probe, where a magnet placed above the needle generates the attachment force.
- 8) Identification of issues with manual needle assembly led to the solution automated die bonding for assembly of the needle. The probe-needle bonding process that applies the gelatin glue *in situ* inside the die bonder equipment works successfully to attach the CMC/glucose needle to the probe.
- 9) A design of experiments on the probe-needle bonding process led to an initial conclusion that relatively high temperatures (80°C) are required to bond needles to the probes using gelatin as an adhesive; unfortunately thermal expansion mismatch issues led to significant cracking of the parylene. Oxygen plasma treatment of the parylene greatly enhances adhesion to the gelatin glue and CMC/glucose needle and eliminating needle delamination at low bonding temperatures.
- 10) Use of 4.5  $\mu\text{m}$ -thick layers of parylene-C creates a more robust probe and cabling that is less prone to breakage. (The prior parylene layer thickness was 2.2  $\mu\text{m}$ .)



- 11) Insertion studies continued from Task 1.2. Stick-slip behavior and corresponding force quantification extracted from a series of needle insertion tests into agarose samples indicate that average insertion forces increase with increase in velocity. However, at low speeds, the needle sticks to the tissue phantom and creates a large volume of damage. As the speed is increased, such damage decreases and eventually disappears above 5 mm/s insertion velocity. Hence, lower average insertion forces do not necessarily correspond to lower tissue damage, and the peak-to-peak amplitude of the stick-slip (force-displacement) waveform plays an important role in determining the damage in the surrounding tissue.
- 12) The continuation of the vibration-assisted insertion study included a series of needle insertion tests into agarose samples to quantify the stick-slip behavior and corresponding necessary insertion force. Insertion carried out using ultrasonic vibration assistance resulted in no improvement (*i.e.*, reduction) in slip-stick effects. However, the ultrasonic drive slips in its mount and so diminished vibration amplitude is likely, warranting further improvement and re-test.

### 5.3 Assessment

Fabrication of stimulation probes was incomplete due to lack of time left in the project. Therefore, all electrical tests employed surrogate test structures comprising parylene-C sealed electrodes on glass substrates. The project resulted in successful probe-needle assemblies, setting the stage for future use of these ultra-compliant probes in medical research applications. The goals of this task expanded to create new protruding probes with improved impedance.

## 6 Task 2.2 – Multi-Probe Array

### 6.1 Objectives

The objective of this task is the design and fabrication of thin-film multi-shank neural probes (“multi-probe arrays”) with transverse intrafascicular multi-channel stimulating electrodes. Best practices learned from the Single Recording Probes task 1.3 and Single Stimulation Probes task 2.1 drive the choice of process and materials. Custom designed bio-dissolvable needle geometries mate with the probe array. Electrical impedance characterization results arise from short-term tests of 12-hour duration. Insertion characteristics of needle arrays follow from *in vitro* and *ex vivo* insertion tests. The task has four main objectives:

- 1) To design and fabricate multi-probe arrays having at least four probe shanks (*i.e.*, needles) with over 50% functional yield.
- 2) To obtain stability of probe electrode impedance at 1 kHz with changes of less than 5% with respect to an initial reference impedance over a 12-hour duration in short-term electrical impedance tests.
- 3) To verify charge injection capacity with a target of greater than or equal to 2 mC/cm<sup>2</sup>.
- 4) To demonstrate successful insertion with retention of the probe inside the medium, as observed from *in vitro* needle insertion tests in an agarose tissue phantom and from *ex vivo* insertion tests in nerve tissue.

## 6.2 Accomplishments

- 1) A four-shank, 40-electrode probe design has its sizing informed by discussions with Prof. Rob Gaunt of U. Pittsburgh for eventual possible future insertion and stimulation studies in cats.
- 2) Two-shank and four-shank “multi-probe arrays” with total thickness of 9  $\mu\text{m}$  (parylene-Pt-parylene) and with total thickness of 4.4  $\mu\text{m}$  were successfully fabricated.
- 3) Successful transfer of two-shank and four-shank probes from a silicon handle wafer to a BGL7080 wax coated glass substrate represents an important step forward in the full process to form multi-shank probes attached to corresponding needle arrays.
- 4) Micromolding of needle arrays is successful for designs with two and four shanks (needles).

## 6.3 Assessment

The needle array bonding process remains to be fully developed. Fabrication of the multi-probe arrays was incomplete due to lack of time left in the project. Impedance stability and charge injection capacity meet targets in the single-shank probes, and so similar success should occur readily with the multi-shank probes once fabricated.

# 7 Project Results

## 7.1 Probe design

### 7.1.1 Single probe design

The sizing of electrode length of 115  $\mu\text{m}$  roughly mates with the axial spacing between nodes of Ranvier in the peripheral nerve, while also being constrained by the desire to minimize the probe shank and needle widths to minimize tissue damage. The electrode width is 15  $\mu\text{m}$ , providing an electrode area of 1725  $\mu\text{m}^2$ , which is roughly equivalent area to a circular electrode having 47  $\mu\text{m}$  diameter. The probe shank length choice is application dependent; the chosen probe length of 3 mm is arbitrary and fits ten electrodes with a spacing of 100  $\mu\text{m}$  between electrodes. The initial single-shank probe design has three distinct regions (cable, transition and needle) as shown in Figure 2. The transition region gradually transitions in width with the aim to eliminate stress concentration issues and so enhance mechanical robustness. Each peripheral probe has 10 electrodes of dimensions 115  $\mu\text{m}$  by 15  $\mu\text{m}$ . The pitch between the electrodes is 100  $\mu\text{m}$ .

The parameterized design of the transition region, shown in Figure 3, assumes that the width of the cable region ( $w_c$ ) is constrained by a need for manual handling by the user while the width of the needle region ( $w_n$ ) is constrained by electrode size and tissue insertion considerations. This leads to the constraint:

$$2r(1 - \cos(\theta)) = w_c - w_n$$

Hence, for a larger bend radius,  $r$ , the bend angle,  $\theta$ , has to be smaller. If the transition region length,  $L_t$ , is given as an independent variable, then the bend angle and radius are:

$$\theta = \tan^{-1} \left( \frac{w_c - w_n}{L_t} \right); r = \frac{w_c - w_n}{2 \sin \theta / 2}$$

Choosing a large  $r$  and small  $\theta$  results in lower maximum stress concentration, as discussed next.



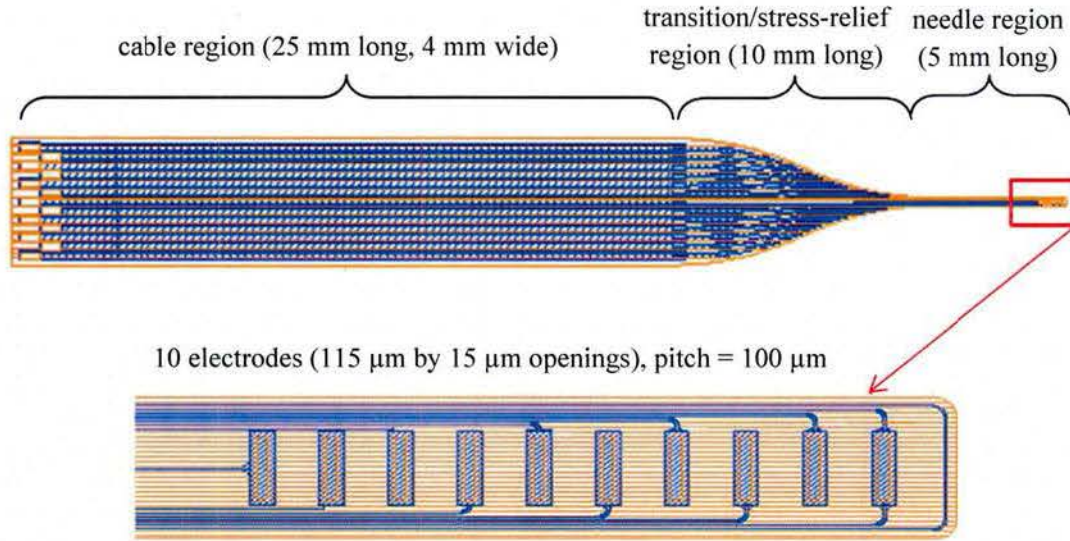


Figure 2. Design of initial single-shank 10-electrode peripheral nerve probe. Blue represents platinum. Orange represents parylene-C.

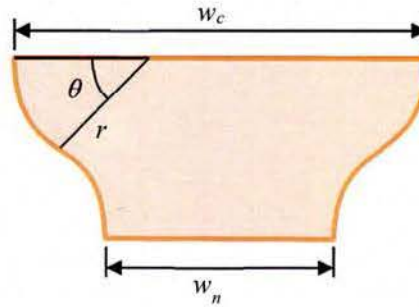


Figure 3. Parameterized design of cable transition region.

### 7.1.2 Probe stress modeling

For the parametric design of neural probes as described in Section 7.1.1, finite-element simulations of tensile stress on the probe verify that using a large  $r$  and small  $\theta$  results in lower maximum stress. The stress distribution in the primary probe design is shown in Figure 5 for a 1 Pa load acting at the end of the probe. Such tensile end loading may occur in probe release during fabrication or from manual handling during insertion. In the initial design,  $w_n = 255 \mu\text{m}$ ,  $w_c = 4 \text{ mm}$ ,  $L_t = 10 \text{ mm}$ ,  $r = 15.2 \text{ mm}$ , and  $\theta = 41^\circ$ . There are no stress concentration areas in the transition region. The metal interconnect in the needle experiences some stress concentration, which is evenly distributed and limited to three times the load.

An analytic analysis on the effect of bending stress on the flexible probe is especially of importance for ALD-encapsulated probes. The ALD ceramics are relatively brittle and have low elongation at break. To determine if the ALD-encapsulated probe will be able to withstand significant amounts of bending, the maximum stress in each layer of the parylene-NL-TiO<sub>2</sub> layer encapsulation scheme is analyzed for varying probe radius of curvature and plotted in Figure 4. The maximum stress is compared with the yield strength



of each of the materials. The results of the analysis indicate that the first failure point is the NL-TiO<sub>2</sub> films, occurring at approximately 100  $\mu\text{m}$  radius of curvature. This very small curvature indicates that it is unlikely for the layers to reach the elastic limit during probe use in insertion into nerves. However, the critical radius of curvature is around that of the vagus nerve in mice. Therefore, ALD yield strength is important to consider when designing for possible cuff applications in small animal models where the probe wraps around the nerve.

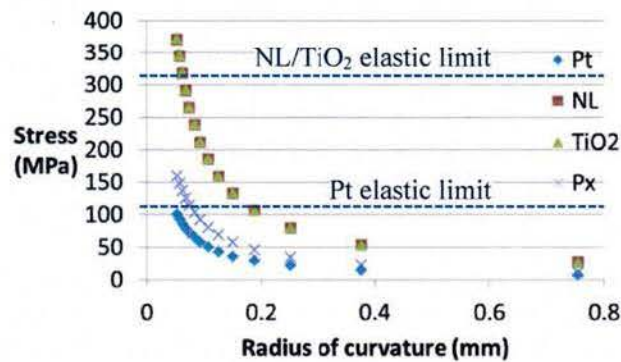


Figure 4. Maximum stress in each layer of the parylene-NL-TiO<sub>2</sub> design versus radius of curvature.

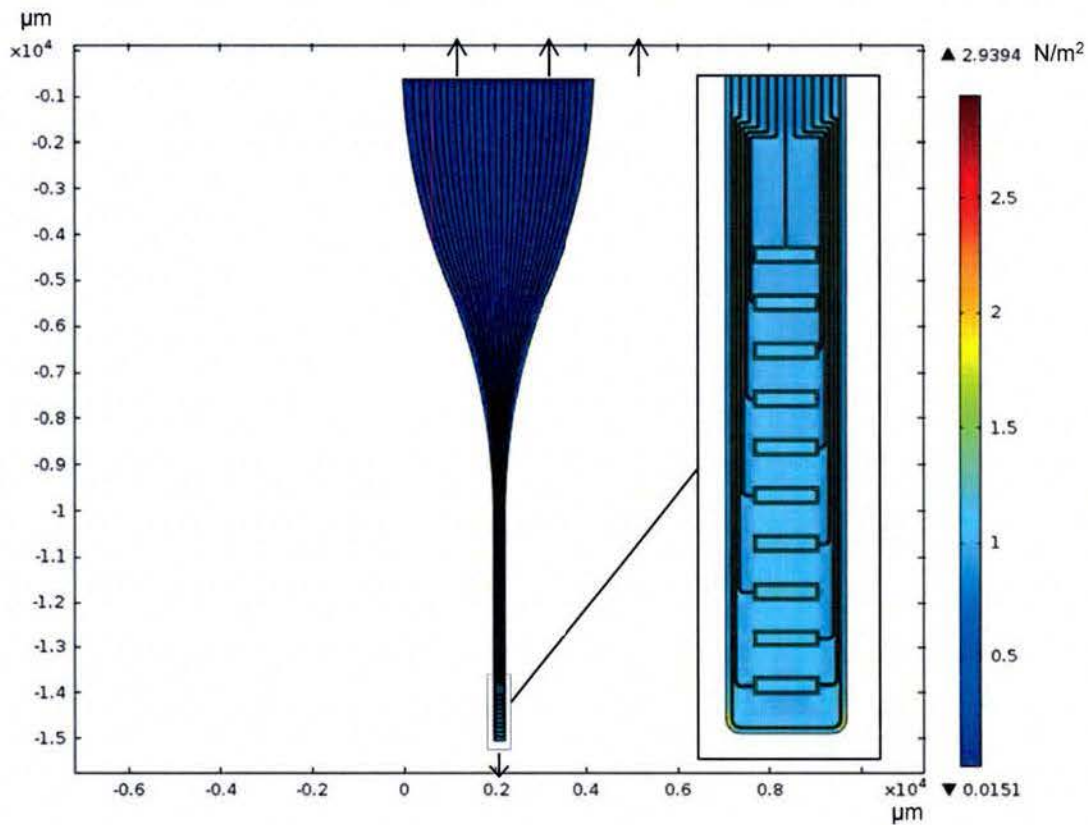


Figure 5. Finite-element simulation of von Mises stress distribution in the designed probe for a 1 Pa normal tensile load.

### 7.1.3 Multi-probe design

The multi-probe array shown in Figure 6 is designed for acute use in a cat model in consultation with Professor Rob Gaunt of the University of Pittsburgh. Practical considerations set the electrode size, spacing, needle length and cable length. Each shank of the multi-probe array has three distinct regions (cable, transition and needle) and are designed similarly to the single probe design variants. Multi-probe arrays with two and four shanks were designed.

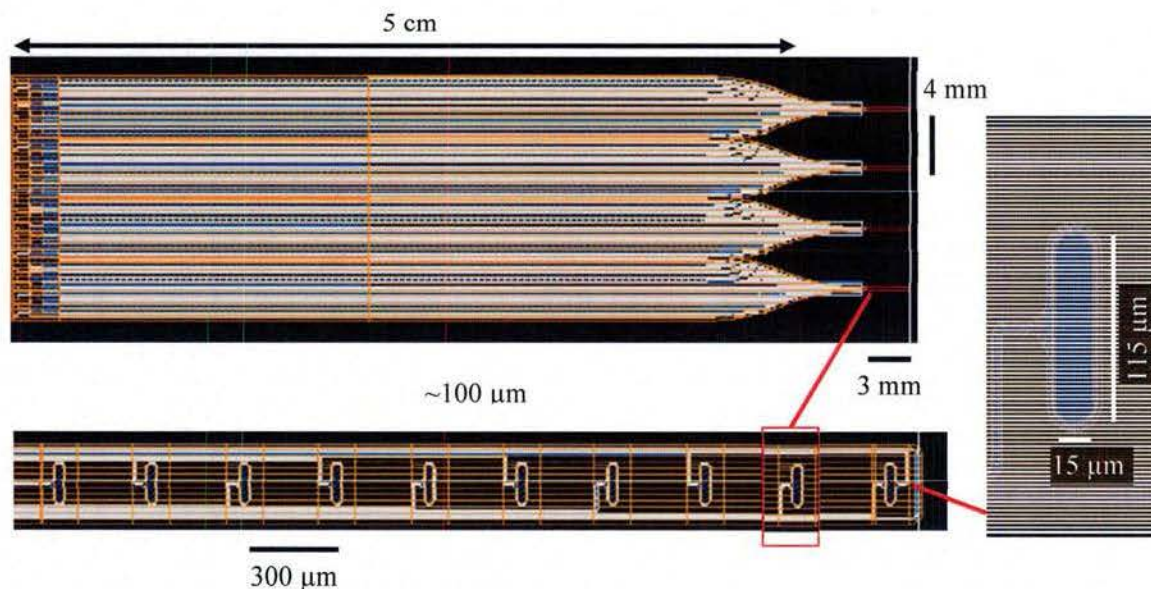


Figure 6. Design of multi-shank probes using 5 cm cable length and 3 mm-long probe shanks.

### 7.1.4 Insulation test structure design

A known issue with parylene-C encapsulated probes is degradation of the insulation in aqueous media, which can lead to complete loss of the insulation over time. A series of test structure designs enable measurement of the electrochemical insulation and extraction of characteristics of the probes arising from the fabrication process variants. Three chip-size designs each comprise an array of 16 test structures. All chips include a large area (60 mm<sup>2</sup>) counter electrode to allow independent electrochemical measurements. The three different chip setups in the “version 1” set of designs are:

- 1A. Small metal electrodes with or without ALD insulation. The test structures include various electrode sizes and aspect ratios to identify the electrode impedance scaling and variation with time for different geometries. Two fully encapsulated wire structures are included for insulation failure monitoring.
- 1B. Large metal electrodes with or without ALD insulation. The test structures include the same size exposed electrodes as in the 1A test structure, but the insulated metal area surrounding the electrode covers a larger fixed area. This design is to identify the effect of the insulated metal on the electrode impedance degradation.
- 1C. Fully encapsulated wiring with or without ALD insulation. The test structures include fully insulated metal wires with varying parylene-C encapsulation overlap and varying alumina



encapsulation overlap (*i.e.*, enclosure widths). If insulation failure happens across the interface between the two parylene-C layers, the insulation impedance change with time is hypothesized to vary with the encapsulation width.

Table 1 provides sizing of the test structures on the chip designs. The layouts are shown in Figure 7(a) through (d). The presence or absence of ALD encapsulation creates variants of each chip design.

Table 1. Test structure designs (“version 1”) for characterizing electrochemical performance.  
All values are in units of  $\mu\text{m}$ , unless specified.

#	<b>1A: Small metal</b> (metal size = electrode size + 20 $\mu\text{m}$ insulation overlap)	<b>1B: Large metal</b> (metal size = 470 $\mu\text{m}$ $\times$ 3 mm)	<b>1C: Fully encapsulated;</b> all wires 10 $\mu\text{m}$ (W), 3.5 mm (L)	
	Exposed electrode size:		Parylene encapsulation enclosure:	ALD encapsulation enclosure:
1	20 $\times$ 20		100	5
2	40 $\times$ 40		100	5
3	80 $\times$ 80		100	10
4	160 $\times$ 160		100	50
5	10 $\times$ 40		100	90
6	20 $\times$ 80		5	5
7	40 $\times$ 160		10	5
8	80 $\times$ 320		10	5
9	10 $\times$ 160		20	0
10	20 $\times$ 320		20	5
11	40 $\times$ 640		20	10
12	10 $\times$ 640		20	15
13	20 $\times$ 1280		60	5
14	10 $\times$ 1280		60	5
15	10 $\mu\text{m}$ $\times$ 3.5 mm encapsulated wire, 10 $\mu\text{m}$ encapsulation enclosure		60	10
16	10 $\mu\text{m}$ $\times$ 3.5 mm encapsulated wire, 50 $\mu\text{m}$ encapsulation enclosure		60	50

A revised “version 2” design of the test structures mitigates the effect of crosstalk when using ALD nanolaminate (NL) encapsulation with  $\text{TiO}_2$  by preventing  $\text{TiO}_2$  connection between independent wires, as shown in Figure 7. The size of the counter electrode was slightly reduced compared to the first version in order to accommodate a larger spacing between the wires. Three additional chip designs (2A, 2B, 2C) provide permutations on the 1C insulation test structures, with the following characteristics:

- 2A: Individual Px (parylene): Both the ALD and parylene layers are etched between the different wires on the same chip, resulting in completely disconnected wires. This arrangement is similar to the bottom of the chip in the 1C structure.
- 2B: Individual Ox (ALD): Only the ALD layers are etched between the wires. A continuous parylene layer covers all the wires. This arrangement is similar to the design of the probe wiring (see section 7.1.1).

- 2C: Continuous Ox (ALD): Neither ALD nor parylene layers are etched between the wires. This arrangement is similar to the upper portion of the chip in the 1C structure. The crosstalk should nonetheless be reduced by the larger spacing between the wires.

For 2A and 2B, the parylene and ALD encapsulation enclosure were changed across the 16 test structures on the chip as indicated in Table 2.

Table 2. Enclosure sizing for 2A and 2B revised test structure designs (“version 2”) for characterizing electrochemical leakage. All values are in units of  $\mu\text{m}$ , unless specified.

#	2A: Individual Px (parylene)		2B: Individual Ox (ALD)
	Parylene encapsulation enclosure	ALD encapsulation enclosure	ALD encapsulation enclosure
1	20	10	10
2	200	100	50
3	60	10	100
4	20	10	10
5	110	10	50
6	150	50	100
7	20	10	10
8	110	100	50
9	110	10	100
10	20	10	10
11	200	100	50
12	110	100	100
13	20	10	10
14	150	100	50
15	60	10	100
16	20	20	10

### 7.1.5 Probe crosstalk modeling

Due to the relatively high electrical conductance of  $\text{TiO}_2$ , even at a layer thickness of 5 nm, as opposed to  $\text{Al}_2\text{O}_3$  and NL, there is a possibility of significant electrical crosstalk. The triple-layer encapsulation scheme is shown in Figure 8(a). A schematic of the crosstalk simulation setup is shown in Figure 8(b). Material property values in the simulations include the electrical conductivity of  $\text{TiO}_2$ ,  $\sigma_{\text{TiO}_2} = 0.001 \text{ S/m}$ , the relative permittivity of  $\text{TiO}_2$ ,  $\epsilon_{r,\text{TiO}_2} = 100$ , the electrical conductivity of NL,  $\sigma_{\text{NL}} = 10^{-8} \text{ S/m}$ , the relative permittivity of NL,  $\epsilon_{r,\text{NL}} = 14.6$ , the electrical conductivity of parylene-C,  $\sigma_{\text{Px}} = 1.7 \times 10^{-17} \text{ S/m}$  and the relative permittivity of parylene-C,  $\epsilon_{r,\text{Px}} = 3.15$ .

The lumped-parameter circuit model in Figure 9 provides a means of explaining crosstalk behavior. Given the values of electrical conductivities and relative permittivity, the titania layer is modeled as a resistance. As in the leakage model, the parylene-C and NL layers are modeled as capacitors between the probe wiring and the saline solution. Values for the lumped parameters are indicated in Figure 9.



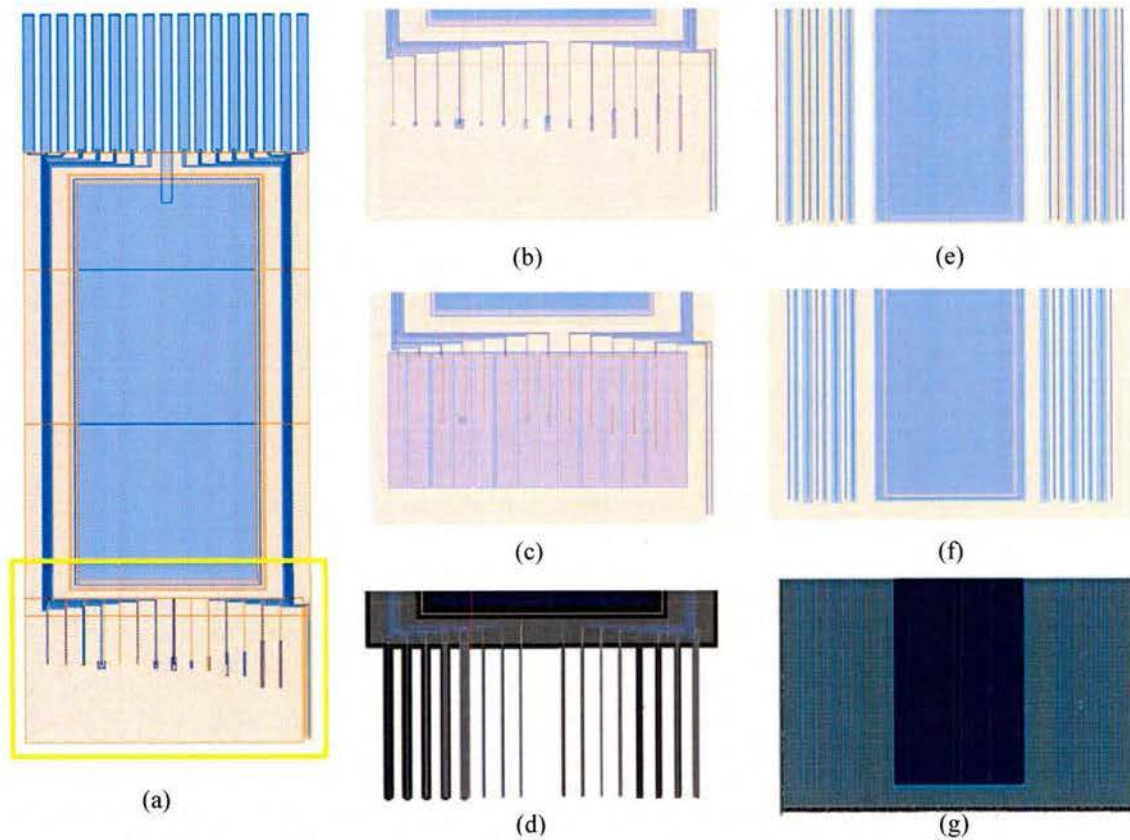


Figure 7. Layout of the different impedance test chips. Pt is represented in blue, parylene in orange, Al<sub>2</sub>O<sub>3</sub> in grey, and NL in green. (a) Full layout of the revision 1A chip. (b)–(g) Detail of the electrode region for the six design variations: (b) small electrodes (1A), (c) large electrodes (1B), (d) insulation (1C), (e) individual parylene (2A), (f) individual ALD (2B), (g) continuous ALD (2C)

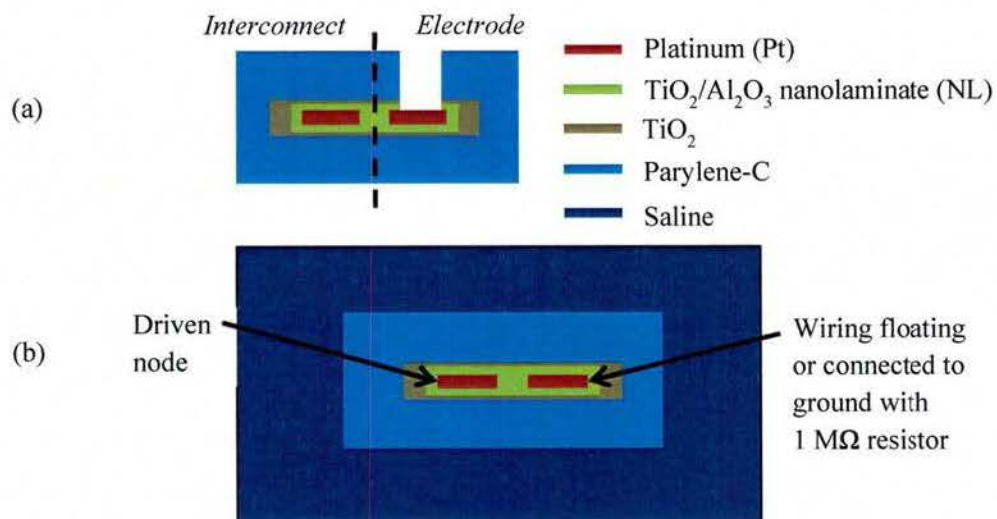


Figure 8. (a) Parylene-NL-TiO<sub>2</sub> encapsulation scheme. (b) Crosstalk simulation setup.

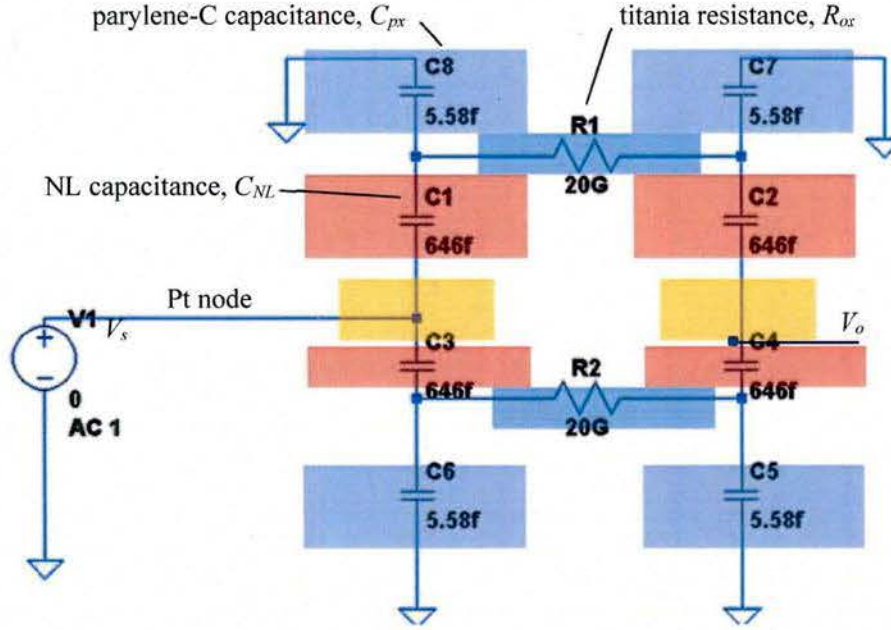


Figure 9. Lumped parameter circuit model for assessment of crosstalk.

The transfer function is:

$$\frac{V_o}{V_s} = \frac{\frac{sR_{ox}}{4C_{px}} + \frac{1}{2C_{px}^2}}{sR_{ox} \left( \frac{1}{4} \left( \frac{1}{C_{px}} + \frac{1}{C_{NL}} \right) \right) + \left( \frac{1}{4C_{px}^2} + \frac{1}{2C_{px}C_{NL}} \right)} \quad (1)$$

A zero in the transfer function occurs at:

$$s = -\frac{2}{R_{ox}C_{px}} \quad (2)$$

and a pole occurs at:

$$s = -\frac{\left( \frac{C_{NL}}{C_{px}} + 2 \right)}{R_{ox}(C_{px} + C_{NL})} \cong -\frac{1}{R_{ox}C_{px}} \quad (3)$$

For values used in the simulation, the calculated pole is at 1.43 kHz and the calculated zero is at 2.85 kHz. The circuit simulation using the lumped parameter model and a corresponding finite-element simulation match the analytic pole-zero behavior.

This initial analysis indicates that there is significant coupling at the frequencies of interest with a cutoff at 1.43 kHz followed by flattening of the frequency response past 2.85 kHz. However, the analysis assumes a worst-case scenario of one electrical line (*i.e.*, the electrode) being driven with zero source resistance and the other line (*i.e.*, the phosphate buffered saline (PBS) solution) floating. In reality, the source is better represented using a Norton current source with finite source resistance. To be more realistic, the undriven line (*i.e.*, the saline and/or nerve tissue) acts as a load resistance. This more realistic lumped parameter model is shown in Figure 10. For the simulations,  $R_M$  is 100 M $\Omega$ ,  $R_s$  is 10 k $\Omega$ , and  $R_L$  is 10 k $\Omega$ .



The current source,  $I$ , is set to 10 nA. The values approximate typical membrane resistance and source resistances. Finite-element simulation indicates that under this condition, the crosstalk coupling is less than  $11 \mu\text{V/V}$  for frequencies of interest (*i.e.*, less than 1 kHz).

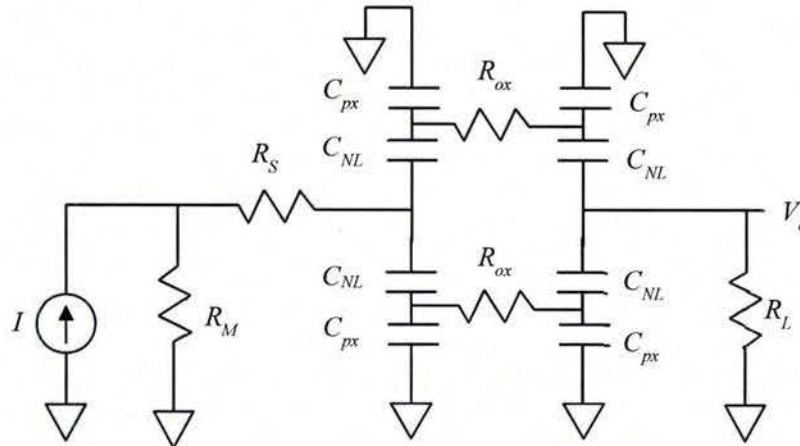


Figure 10. Lumped parameter model with a Norton current source modeling the electrode drive and a load resistance modeling the PBS.

## 7.2 Probe fabrication processes

### 7.2.1 Parylene fabrication process

The initial process used to fabricate single-shank neural probes on Si is shown in Figure 11. A  $2 \mu\text{m}$  layer of parylene-C is first deposited on a Si wafer that was treated with A174 silane. A 120 nm-thick layer of Pt is then deposited and patterned using lift off. A second layer of parylene-C ( $2 \mu\text{m}$ ) is then deposited. The parylene is then patterned and etched using an  $\text{O}_2$  reactive-ion etch (RIE). A fabricated probe is shown in Figure 12. A process with alumina was also designed, with the alumina layer extending throughout the probe except for  $5 \mu\text{m}$  from the edges of parylene-C.

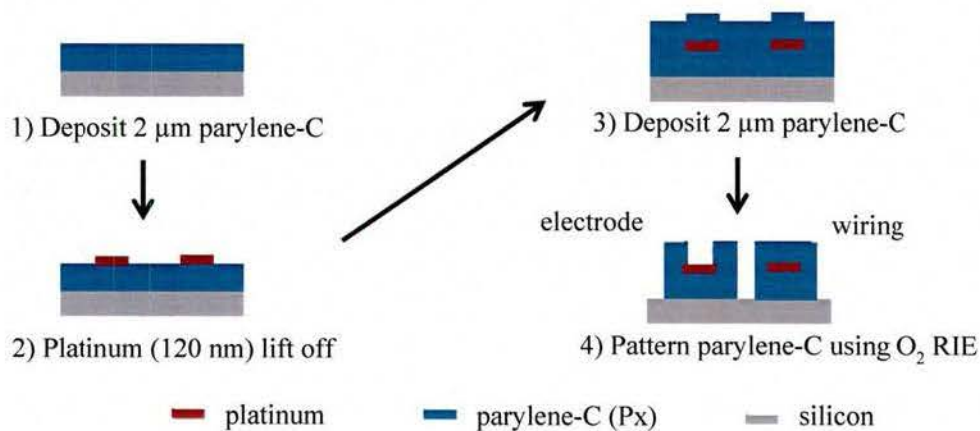


Figure 11. Neural probe fabrication process.

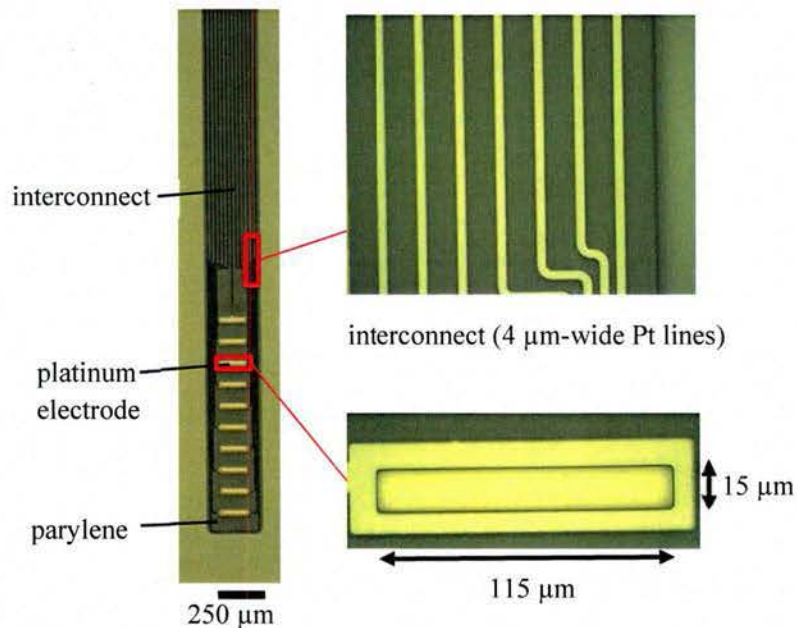


Figure 12. Fabricated neural probe on a silicon substrate. Cable not shown.

Thermal annealing improves the parylene-parylene interface by heating the parylene-C above its melting point of 290 °C. The annealing conditions are 3 h at 300°C under a 10 mT vacuum with N<sub>2</sub> backflow. All results for parylene samples employ this annealing step; without annealing, the electrical leakage properties are poor.

A revised process that creates thicker parylene-C probes avoids wrinkling issues during the needle assembly and release process (see section 7.5.3.2). Devices were fabricated using two layers of 4.5 μm-thick parylene-C (instead of 2.2 μm-thick) requiring increased parylene-C etch times (80 min versus 40 min) and Cr hard mask thicknesses (33 nm versus 20 nm). A more viscous resist (AZ4620) is used for grayscale lithography (as compared with AZ4210 for the process with 2.2 μm-thick resist), with subsequent modification in exposure and descum times. The thick parylene devices include multi-shank probe arrays (arrays of 2 and 4 probes). The process has to be fine-tuned because of a more aggressive critical dimensions (*i.e.*, 2 μm Pt line width versus 4 μm Pt line width and thin NL-TiO<sub>2</sub> lines separated for each probe shank versus wide contiguous alumina encapsulation). Further thick-parylene process development involved protruding electrode development in parallel, as discussed in section 7.2.5 and including optical images of fabricated thick-parylene devices.

The test structure fabrication process is similar to the one for probes described in Section 7.2.1, but on glass rather than a silicon substrate and without the probe transfer process. The test structure substrate is glass in order to prevent possible electrical coupling through the substrate. The simplified process flow, with additional ALD ceramic encapsulation, is described in Figure 13. Example fabricated test structures and associated process results are shown in the following section 7.2.2.

Three additional modifications to the process flow explore further potential to improve the parylene-parylene interface properties. These exploratory modifications are:

- A-174: Application of an A-174 silane liquid treatment before each alumina deposition
- IM: Replacement of the O<sub>2</sub> plasma descum step by an ion mill descum



- F: Inclusion of an O<sub>2</sub> RIE followed by SF<sub>6</sub> plasma step potentially improves adhesion by modifying the parylene surface chemistry by fluorinating the surface of the parylene.

Electrical leakage test results for these exploratory modifications are found in section 7.4.4 (see Figure 47).

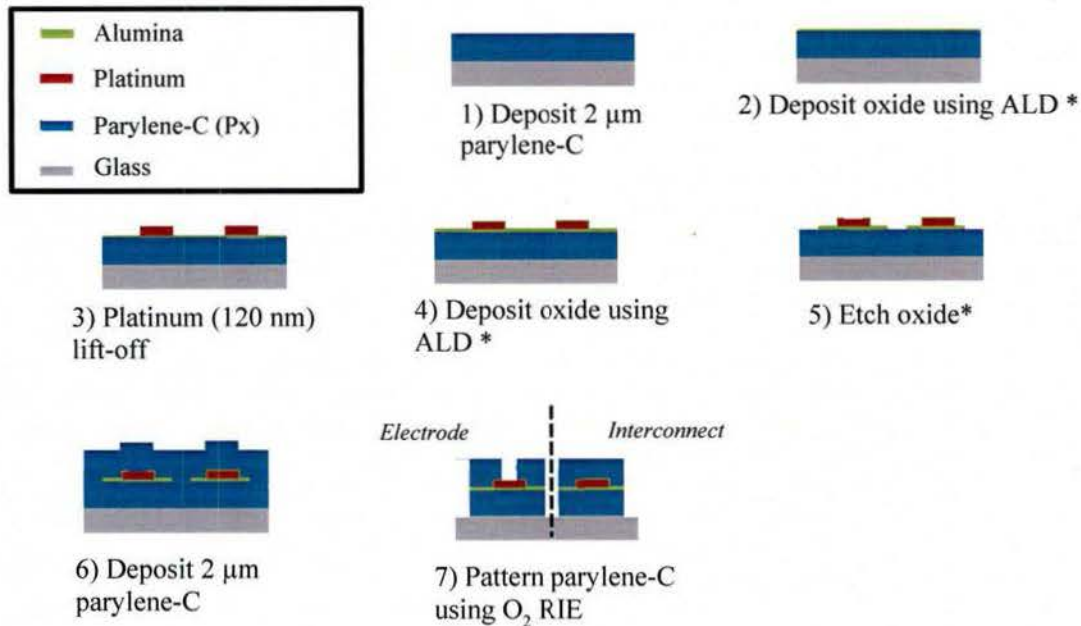


Figure 13. Simplified process flow for the impedance test structure fabrication. Steps denoted by \* are only used for structures including an oxide insulation layer. The additional exploratory modifications (A-174 and SF<sub>6</sub>) are performed between steps 5 and 6.

### 7.2.2 ALD ceramic thin-film encapsulant processes

Based on impedance test results that show that alumina is a poor encapsulation material, more promising candidates as long-term insulators lie in other ceramic encapsulants that are deposited using atomic layer deposition (ALD). Exploration of insulation stacks included several ceramic insulation layers: 50 nm-thick ALD Al<sub>2</sub>O<sub>3</sub>, 40 nm-thick ALD TiO<sub>2</sub>, 80 nm thick ALD Al<sub>2</sub>O<sub>3</sub>-TiO<sub>2</sub> nanolaminate (NL), and 80 nm thick ALD Al<sub>2</sub>O<sub>3</sub>-TiO<sub>2</sub> nanolaminate with an outer 5 nm TiO<sub>2</sub> adhesion layer (NL-TiO<sub>2</sub>). Test structure samples consist of wiring encapsulated with these ALD materials. The general process flow is shown in Figure 14. Optical images of example fabricated structures are shown in Figure 15.

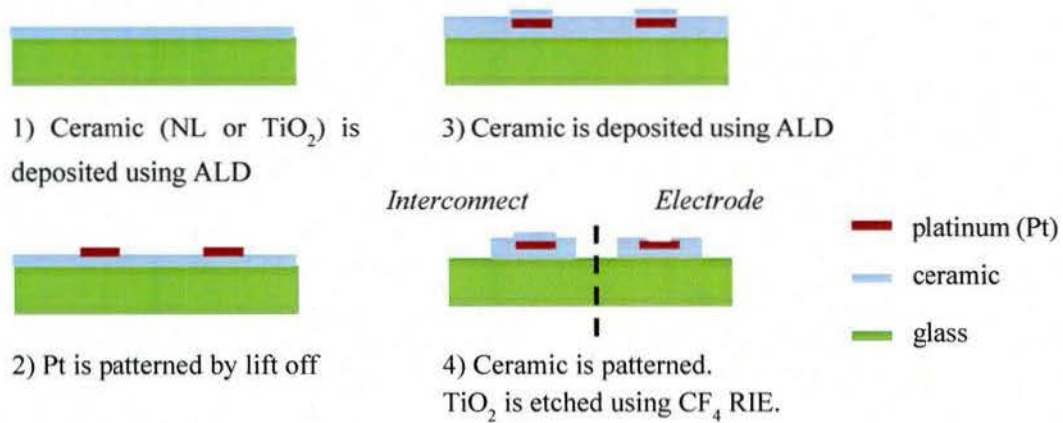
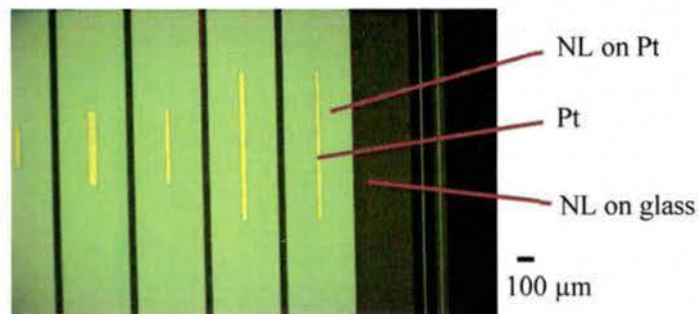
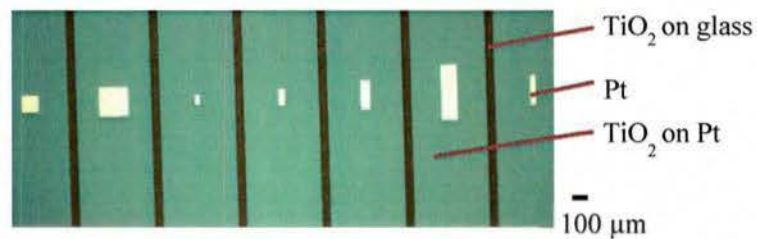


Figure 14. Fabrication flow of ceramic test structures



(a)



(b)

Figure 15. Optical images of example fabricated test structures with ceramic encapsulation, on glass substrates. (a) Nanolaminate (NL) encapsulation. (b)  $\text{TiO}_2$  encapsulation.



Significant process development encompasses the etching of the various ALD ceramics since there is little literature on the etching of these ceramics. The result of the etch rate measurements are tabulated in Table 3.

Table 3: Measured etch rates for ALD films and their corresponding etchants. All etch rates are in units of nm/min.

Etchant \ ALD film	TiO <sub>2</sub>	Al <sub>2</sub> O <sub>3</sub>	NL
BHF	Not etched	~40	~40
Trion RIE SF <sub>6</sub> plasma	~10	Not etched	Not etched
Versaline ICP-RIE (Cl <sub>2</sub> plasma)	~40	~50	~30
Ion Mill	~5	~5	~4

Buffered hydrofluoric acid (BHF) etches Al<sub>2</sub>O<sub>3</sub> and NL. CF<sub>4</sub> RIE etches TiO<sub>2</sub>. For NL-TiO<sub>2</sub>, different methods of etching were investigated. Etching NL using BHF leaves residue on the wafer. The etch residue lowers the adhesion of the parylene layer and results in a lower impedance (~10x lower initially at 0.1 Hz). Using a dry Cl<sub>2</sub> ICP-RIE etch followed by piranha (H<sub>2</sub>SO<sub>4</sub>:H<sub>2</sub>O<sub>2</sub>) to remove resist exposed to Cl<sub>2</sub> plasma results in a much cleaner etch. Optical images comparing the two methods of etching are shown in Figure 16. Electrochemical Impedance Spectroscopy (EIS) tests comparing the two methods of etching show significant differences in encapsulation performance with the dry etch being far superior (Figure 17).

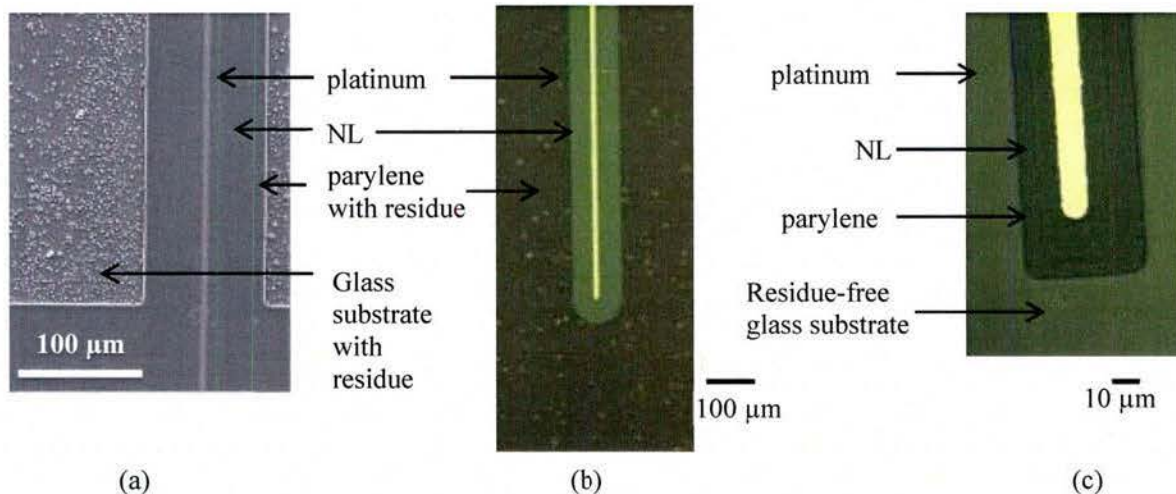


Figure 16. Comparison of the NL-TiO<sub>2</sub> etching process. Test structures fabricated using BHF etching (a) after the final parylene etch and (b) before the final parylene etch. Both images show residue on the parylene, which is subsequently transferred to the glass. (c) Test structure fabricated using the dry etch, revealing a residue-free surface after the final parylene etch.

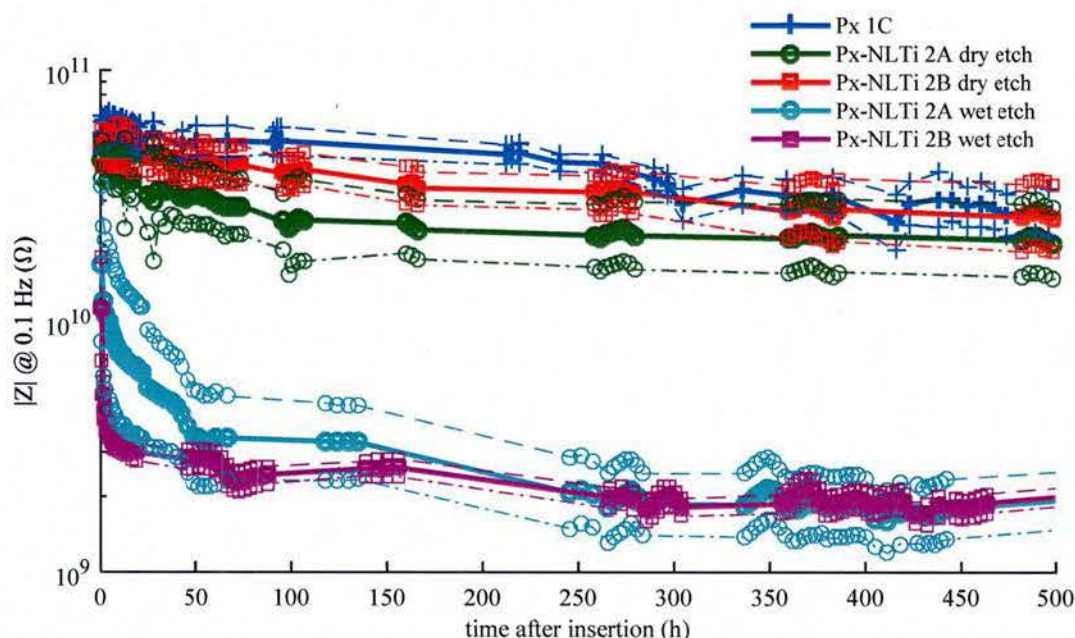


Figure 17. Impedance of insulation test structures for different etch processes for parylene-NL-TiO<sub>2</sub> and parylene-only encapsulant shown for comparison. The wet etch using BHF reveals lower impedance, signifying a low quality insulation.

Following initial electrochemical impedance studies on the various ceramics (see section 7.4), the ‘triple-layer’ parylene-NL-TiO<sub>2</sub> encapsulation scheme achieves flexibility and compliance using parylene-C, good encapsulation properties using TiO<sub>2</sub>/Al<sub>2</sub>O<sub>3</sub> nanolaminates (NL) upon probe release and good adhesion between the various layers using TiO<sub>2</sub>. The encapsulation properties of TiO<sub>2</sub> alone and of NL alone reveal less corrosion in PBS than with the Al<sub>2</sub>O<sub>3</sub> encapsulation. However, the NL-only film has poor adhesion to parylene-C, leading to rapid degradation in the capacitive impedance of the wiring. Hence, a layer of TiO<sub>2</sub> is deposited between the parylene-C and NL films as an intermediate adhesion layer.

The resulting process flow to fabricate the parylene-NL-TiO<sub>2</sub> test structures is described in Figure 18. A 2 μm layer of parylene-C is first deposited using chemical vapor deposition (CVD) followed by 5 nm of ALD TiO<sub>2</sub> and 80 nm of ALD NL. A stack of Ti/Pt/Ti (10 nm, 125 nm, 10 nm) is then deposited by sputtering and patterned using lift off. Following that, a second 80 nm layer of ALD NL is deposited followed by 5 nm of TiO<sub>2</sub>. A second layer of 2 μm parylene-C is then deposited using CVD. The parylene is then patterned using a Cr hard mask and etched using O<sub>2</sub> RIE. An Ar<sup>+</sup> etch is then performed to remove PtO<sub>2</sub> formed during the O<sub>2</sub> RIE. Given the problem of crosstalk coupling because of the low resistivity of TiO<sub>2</sub>, revised “version 2” test structure designs (see section 7.1.4 and Figure 7) that separate the TiO<sub>2</sub> between wires are used in EIS studies and provide a guide to design probes with this ‘triple layer’ encapsulation. Example fabricated test structures using the new design are shown in Figure 19.



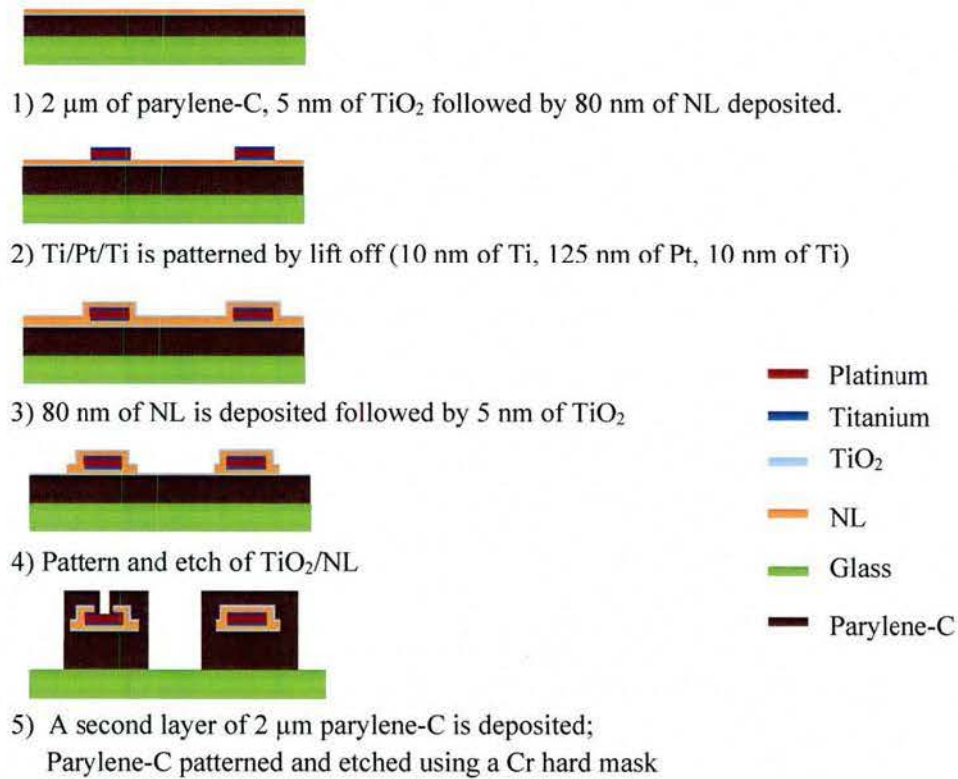


Figure 18. Fabrication flow of parylene-NL- $\text{TiO}_2$  ceramic test structures.

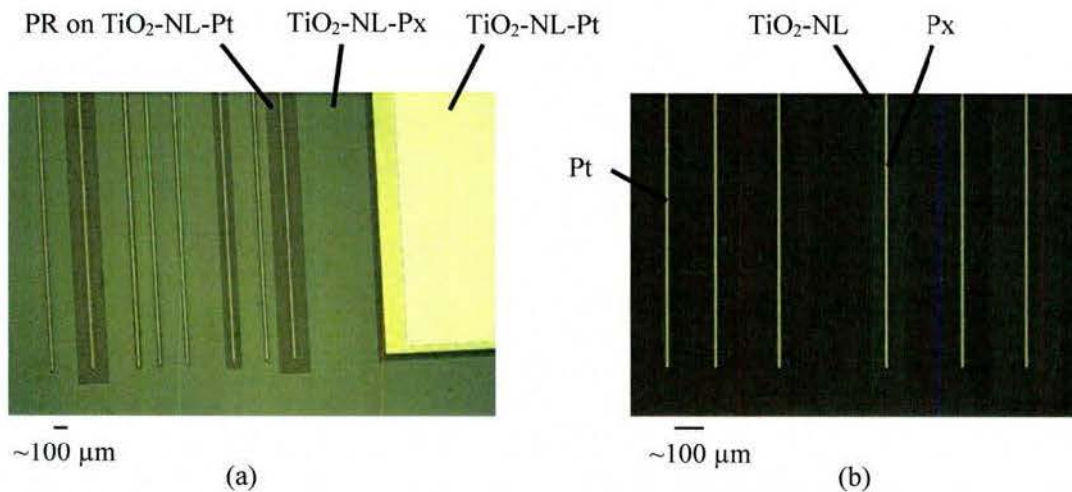


Figure 19. Optical microscope images of fabricated 'version 2' test structures with parylene-NL- $\text{TiO}_2$  encapsulation. (a) After photoresist (PR) patterning of the NL- $\text{TiO}_2$  layer. (b) After etching of the NL- $\text{TiO}_2$  between wiring, and after removal of the PR.

### 7.2.2.1 Oxide film ellipsometry

Ellipsometric measurements of thickness and refractive index of the ALD-deposited oxides (*i.e.*, ceramics) on Si, shown in Figure 20, provide data toward a better understanding of their degradation mechanism in saline. Somewhat surprisingly, the measured thickness of all three films considered *increases* over time in PBS, which does not match expectations of film etching. Instead, water penetration might be causing corrosion that creates an increase in overall film thickness. Nonetheless, the stability of NL is much greater than either  $\text{Al}_2\text{O}_3$  or  $\text{TiO}_2$ , as evidenced by the smaller variation in both thickness and refractive index (thickness varies  $\sim 1.5$  times less for NL than  $\text{TiO}_2$  and  $\sim 8$  times less than for  $\text{Al}_2\text{O}_3$ ;  $n_r$  varies  $\sim 6$  times less than  $\text{TiO}_2$  and  $\sim 20$  times less than  $\text{Al}_2\text{O}_3$ ).

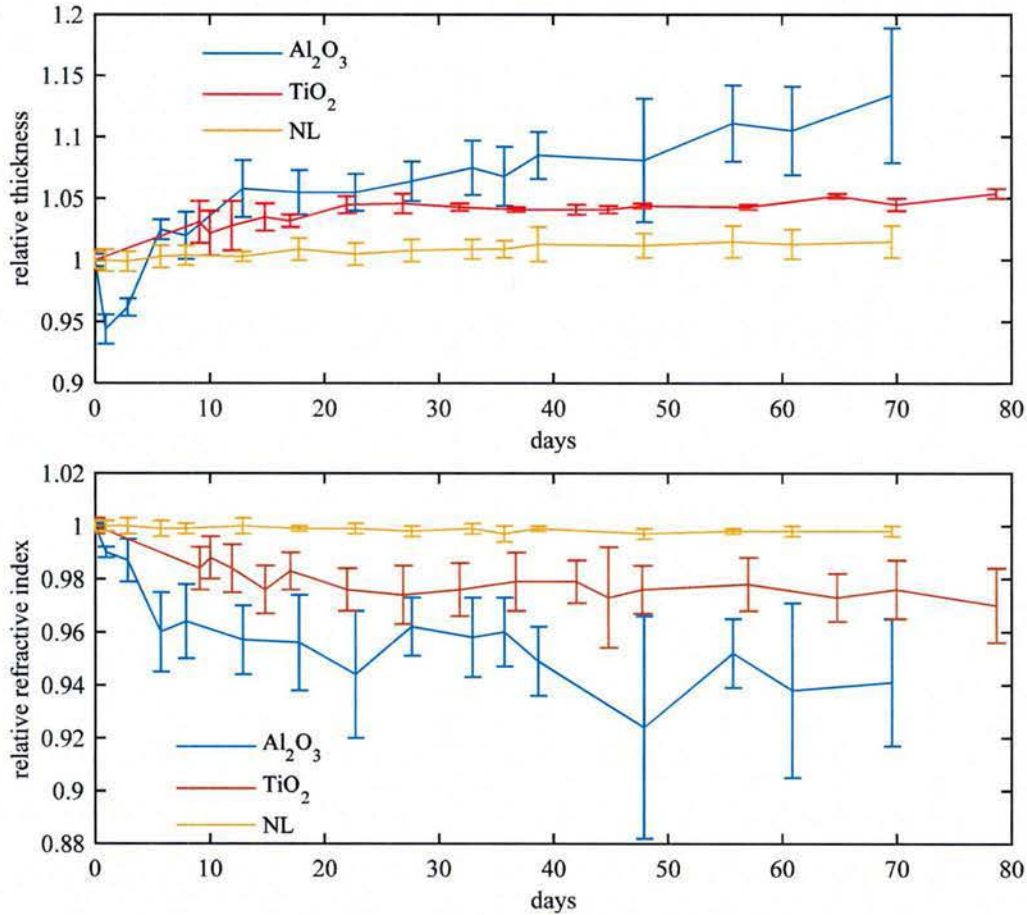


Figure 20. Ellipsometric measurements on ALD oxides in 1x PBS at 60 °C, showing relative variations in film thickness (top) and refractive index (bottom). Initial values of thickness are:  $t_{\text{Al}_2\text{O}_3}=48.5$  nm,  $t_{\text{TiO}_2}=49.4$  nm,  $t_{\text{NL}}=86.9$  nm; and initial values of refractive index are:  $n_{\text{Al}_2\text{O}_3}=1.63$  nm,  $n_{\text{TiO}_2}=2.35$  nm,  $n_{\text{NL}}=1.93$  nm.

### 7.2.3 Electrode fabrication

Impedance testing in phosphate buffered saline (PBS) solution at room temperature indicates a higher than expected measured impedance for the first prototypes of platinum electrodes. Material characterization of the electrode surface using X-ray Photoelectron Spectroscopy (XPS) reveals the



presence of a thin (<5 nm) layer of oxidized platinum (PtO or PtO<sub>2</sub>). The platinum oxide layer creates an additional capacitive barrier to charge transfer. The Pt is more oxidized than normal due to the O<sub>2</sub> reactive-ion etch of the parylene film that creates the opening to the electrode. The addition of an Ar<sup>+</sup> ion milling step as the last step of our fabrication process removes this layer. The effects on electrode impedance are shown in Figure 21. The comparison of measurements before and after Ar<sup>+</sup> ion milling verifies the increase of the impedance of the platinum electrodes by ~10x due to the presence of platinum oxide.

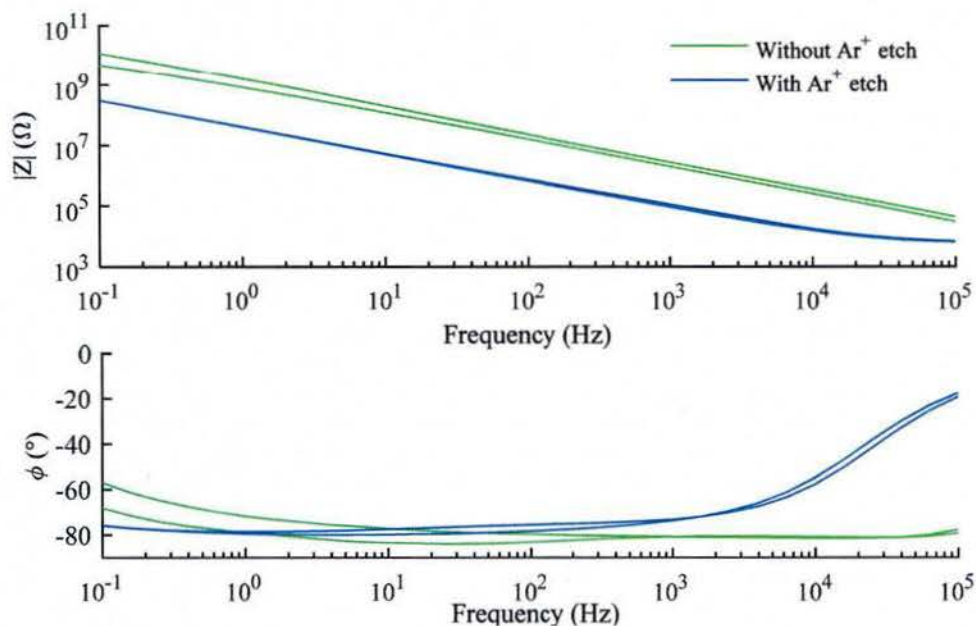


Figure 21. EIS spectra for four 80μm x 80μm Pt electrodes. Ar<sup>+</sup> etch was performed on 2 of the samples, showing a ~10x decrease in impedance at all frequencies below ~10 kHz (where the wiring and PBS resistance dominate the impedance).

#### 7.2.4 Iridium oxide electrodes

An in-house activated iridium oxide film (AIROF) process provides the basis for iridium stimulation electrodes. As a test, 120 nm layer of iridium is first deposited on a silicon wafer. After cleaving the wafer, a part of the wafer is immersed in 1X PBS and 2000 cycles of +0.9 V and -0.6 V are applied. The subsequent measured Charge Storage Capacity (CSC) is plotted in Figure 22. The increase in magnitude of CSC indicates that the activation was successful. The immersed portion of the piece changed in color; however, no change in thickness was observed as measured using a profilometer.

An XPS survey scan on the AIROF sample indicates that 42% of the surface is iridium and 58% is oxygen, indicating a stoichiometry of IrO<sub>1.4</sub>. The iridium not exposed to PBS has 15% oxygen, indicating that the some iridium is oxidized prior to the PBS experiment. However, the increase in oxidation content after cyclic pulsing indicates that activation is successfully occurring. Performing XPS on another wafer coated with iridium indicates that the thin-film sample does not have detectable oxygen content. It is likely that the iridium target was not adequately conditioned before the deposition of the iridium on the wafer having the 15% oxygen.

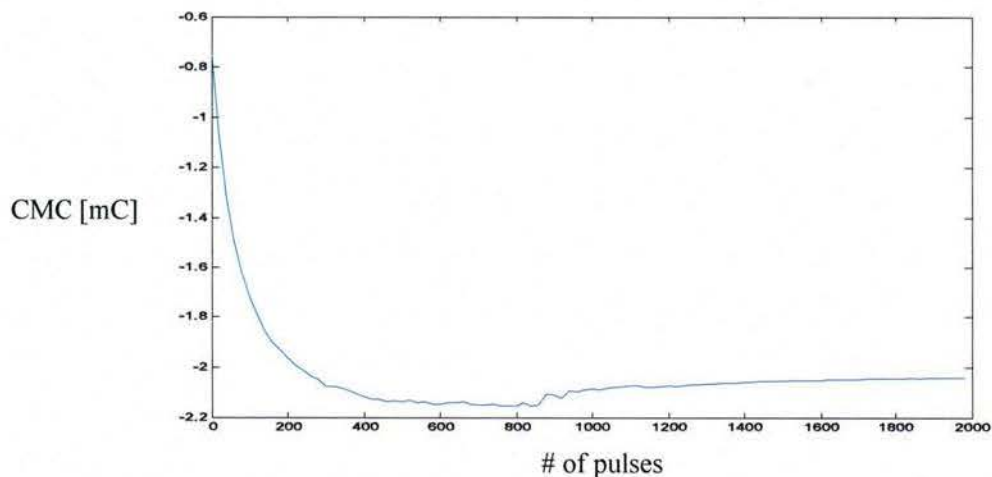


Figure 22. Charge Storage Capacity versus number of pulses for an AIROF test electrode.

A process to fabricate sputtered  $\text{IrO}_2$  (SIROF) electrodes was developed using different pressures while keeping the ratio of Ar:O constant at 3.33 based on process parameters in the literature. At high pressures (14.5 mT), the deposited film is non-uniform. The film is deposited at 100 W DC power and has an O:Ir ratio of 1.76 at the sides and 1.63 at the center, based on energy dispersive x-ray spectroscopy (EDX) measurements. Subsequent RF sputtering and a lower chamber pressure of 6.95 mT creates less mass transport limitation and greater film-thickness uniformity. This second thin-film sample is deposited at 100 W RF power and has an O:Ir ratio of 2.1 across the substrate.

Using the developed  $\text{IrO}_2$  process parameters, test structures were fabricated on a glass substrate. The fabrication of the test devices emulates the steps of the fabrication of protruding electrodes on Si, with the top conductive layer being  $\text{IrO}_2$ . A fabricated test electrode is shown in Figure 23.

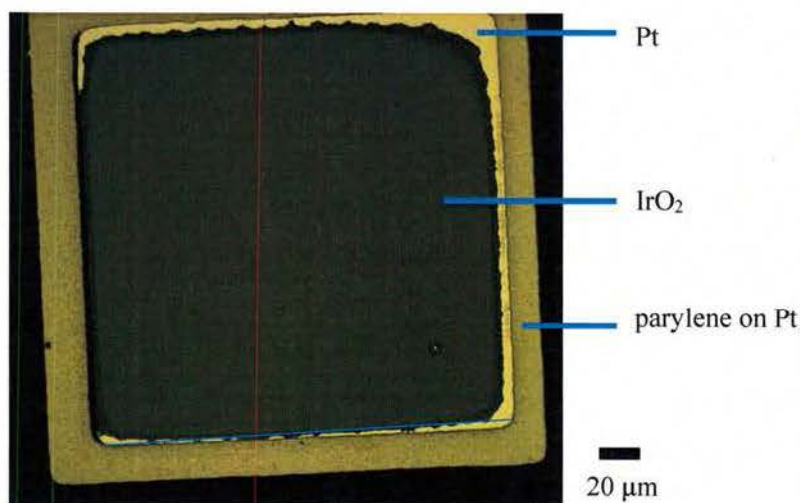


Figure 23. 200  $\mu\text{m}$  by 200  $\mu\text{m}$  SIROF test electrode fabricated on glass to test charge injection capacity.



### 7.2.5 Protruding electrodes

A two-layer platinum process is developed to create protruding electrodes. Via test structures test for functionality of protruding electrodes processed using this method. In the first iteration of the process development, a thick second layer of platinum ensures connectivity between the interconnect metal and the electrode, essentially creating a via, as shown in the process steps in Figure 24(a). In the first step, a 2.2  $\mu\text{m}$ -thick layer of parylene-C is deposited using CVD. Following that, 125 nm of Pt is deposited and patterned using lift off. A second 2.2  $\mu\text{m}$ -thick layer of parylene-C is then deposited. Parylene-C is then patterned using  $\text{O}_2$  RIE with Cr as a hard mask. A second 2.5  $\mu\text{m}$ -thick layer of Pt is then deposited and patterned using lift off. All development and resist stripping steps are followed by a 1 min, 100 W,  $\text{O}_2$  plasma. Fabricated via structures are shown in Figure 24(b).

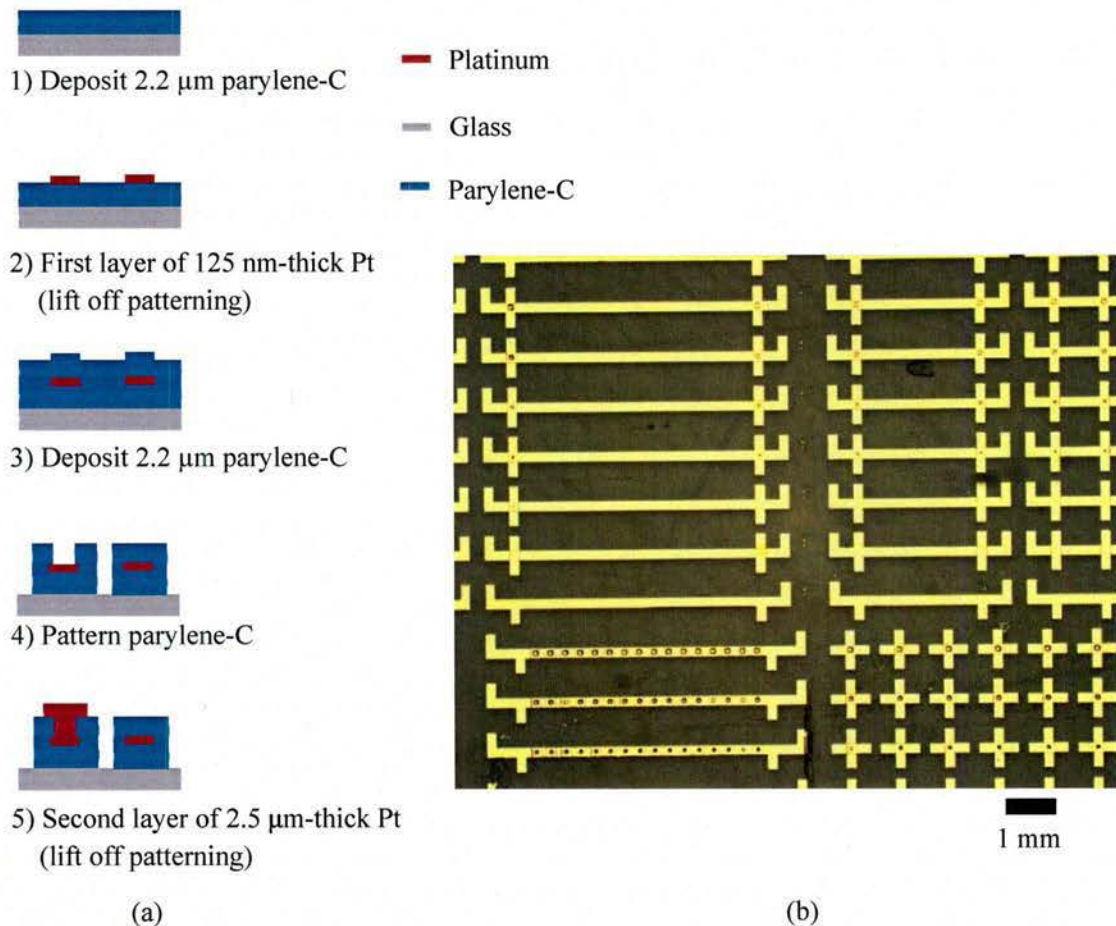


Figure 24. (a) Fabrication steps for vias with protruding electrodes. (b) Fabricated via test structures.

Using this process, the resistance of a 100  $\mu\text{m}$  by 100  $\mu\text{m}$  contact is approximately 1.2  $\Omega$  as seen in Figure 25. However, delamination occurs between the Pt layers at the parylene step interface, which will cause yield issues. In order to address Pt step coverage, sloped sidewalls were developed using grayscale lithography. The gentler slope also eliminates the need for a thick Pt layer. An initial test wafer is fabricated using proximity lithography (150  $\mu\text{m}$  spacing between Si and the mask) and a prior grayscale mask made

by a previous Ph.D. student (Dr. Jason Gao). The resist profile is characterized using SEM and a contact profilometer and is shown in Figure 26. However, for the protruding electrodes, the sidewalls have to be sloped over a shorter distance (10-20  $\mu\text{m}$ ) because of the relatively narrow sizing of the electrodes. In order to address this, new grayscale patterns and designs were developed to achieve such slopes.

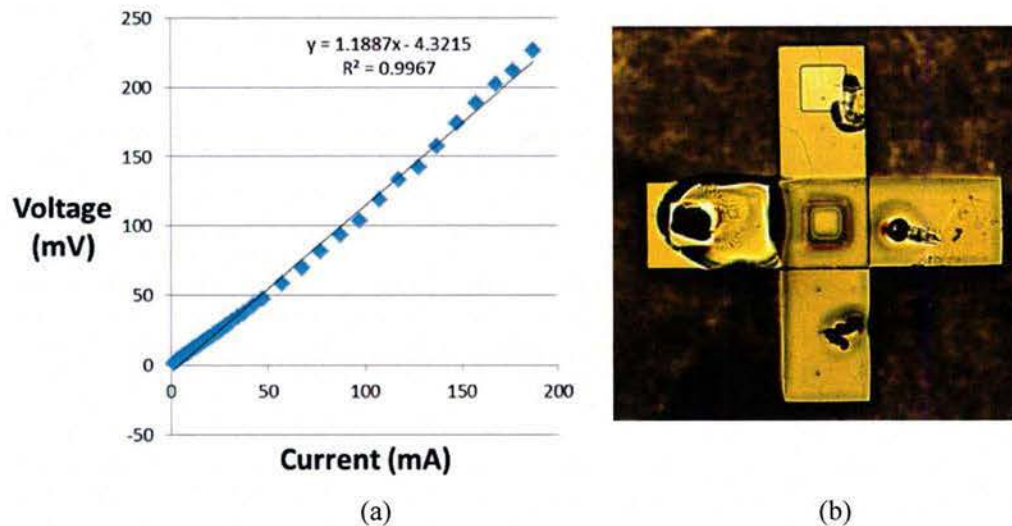


Figure 25. 100  $\mu\text{m}$  by 100  $\mu\text{m}$  platinum-platinum contact. (a) I-V curve with slope of 1.2  $\Omega$  measured using a four-point I-V measurement setup. (b) Optical image of contact after 0.2 A of current is applied, showing melt damage.

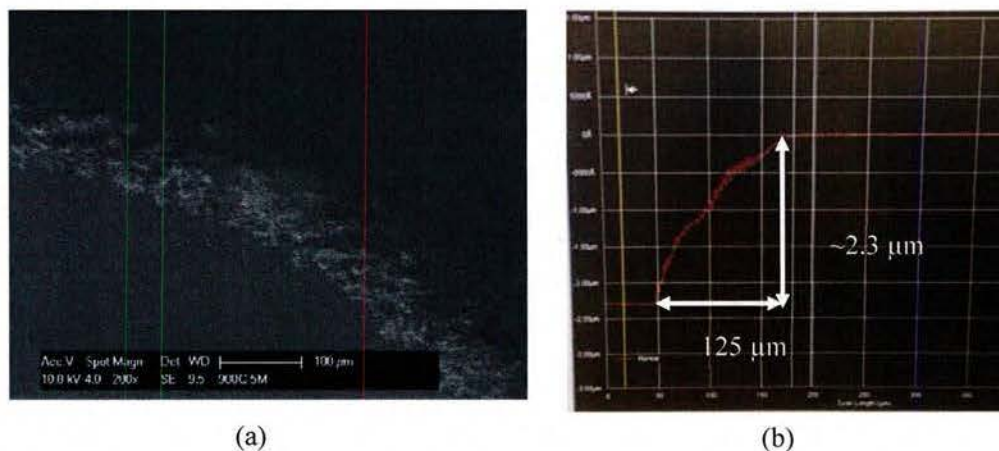


Figure 26. (a) SEM of gradual resist profile fabricated using grayscale lithography. (b) Sidewall profile measured using contact profilometry.

Protruding electrodes were fabricated building on results from initial grayscale lithography tests. Greyscale masks, with “donut” shaped features to accommodate protruding electrodes were fabricated using a Heidelberg Instruments Direct Write Laser (DWL) tool. The pixel size of the mask is approximately 1  $\mu\text{m}$  which is close to the resolution limit of the tool. In order to create the grayscale effect,



photolithography is performed with these masks in proximity mode with the wafer spaced 150  $\mu\text{m}$  from the mask during exposure, resulting in photoresist with gently sloped sidewalls. Figure 27 is an optical photo of a protruding electrode after etch transfer of the greyscale slope from photoresist to the underlying parylene, and then subsequent second-layer Pt deposition and patterning. Sloped sidewalls are transferred from the photoresist to the underlying parylene-C layer when exposed to  $\text{O}_2$  reactive-ion etching, due to the low etch selectivity between parylene-C and photoresist. The second 125 nm-thick layer of Pt is then deposited and patterned using lift off.

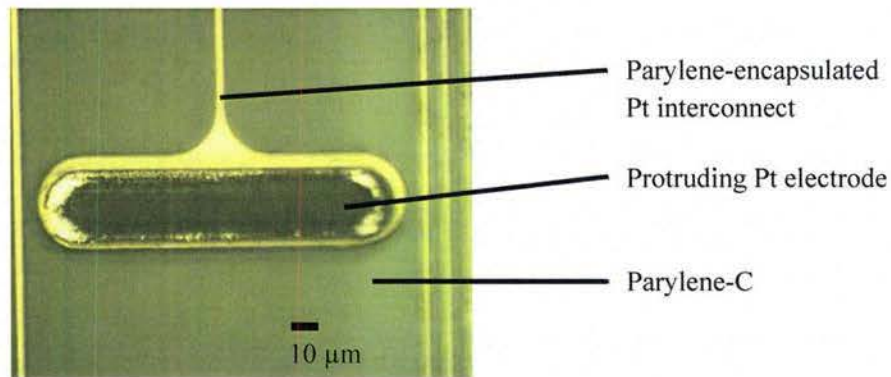


Figure 27. Fabricated protruding electrode with coated Pt.

A white-light optical profilometer (Zygo Corp., Middlefield, CT) and an optical microscope ( Alicona, Graz, Austria) with profile measurement capabilities enabled characterization of the profile of the sloped sidewalls. The protrusion profiles are shown in Figure 28 with the Alicona measurement indicating a 1.4  $\mu\text{m}$  tall protruding electrode.

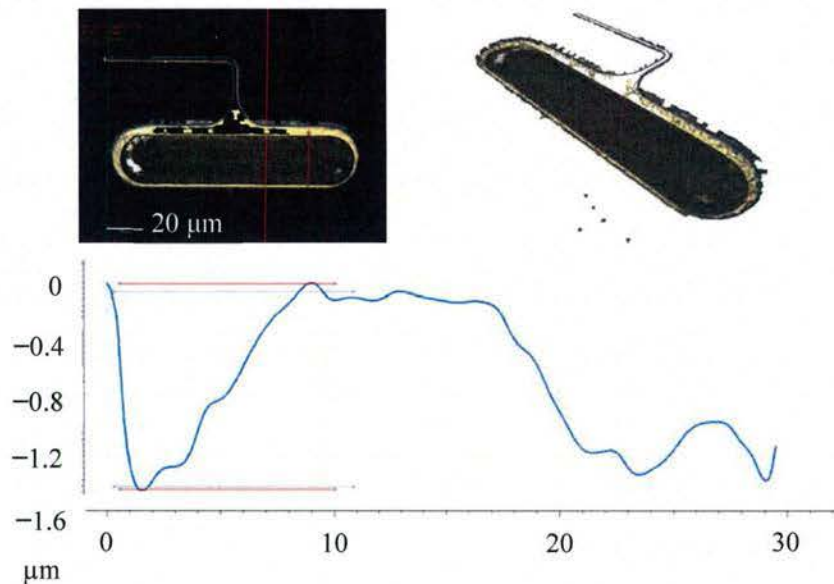


Figure 28. Measurement of protruding electrode surface profile using the Alicona optical microscope.

The partially etched parylene-C is rougher than in the field. AFM characterization in Figure 29 indicates the surface roughness of Pt deposited over roughened parylene-C is 120 nm, compared to a normal parylene roughness of 18 nm in the field. This method of fabrication can potentially result in improved performance of electrodes due to the increased surface area from the surface roughening.

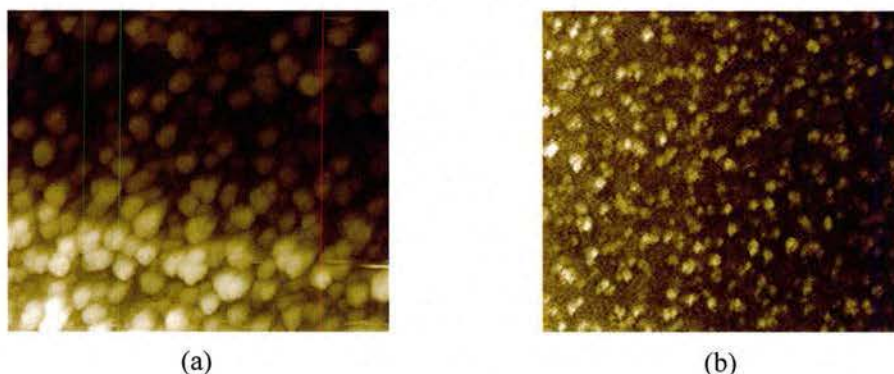


Figure 29. AFM measurements of roughness on parylene. (a) Platinum deposited on roughened parylene on the protruding electrode;  $R_a \sim 120$  nm. (b) As-deposited parylene in the field;  $R_a \sim 18$  nm.

An SEM comparison of the three types of electrodes investigated is provided in Figure 30, along with simplified cross-sectional schematics of the layers. The “with gap” design on the left is believed to provide better adhesion of the parylene protrusion by enabling it to fuse onto the underlying parylene. This adhesion property remains to be tested long term in PBS. Optical images of the “with gap” design of the protruding electrodes is shown in Figure 31(a) prior to the second platinum deposition to show the first-Pt raceway, and in Figure 31(b) after the probe is successfully transferred to a BGL7080-coated glass slide using the transfer process described in the next section 7.2.6.

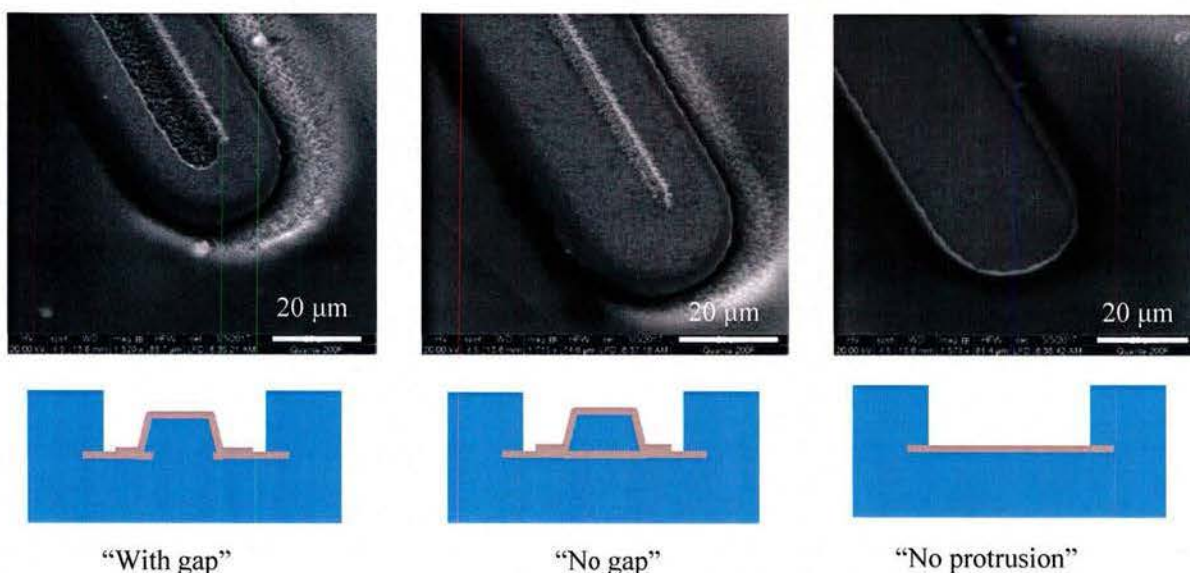


Figure 30. Versions of protruding electrodes. SEM images (top) and cross section schematic (bottom).



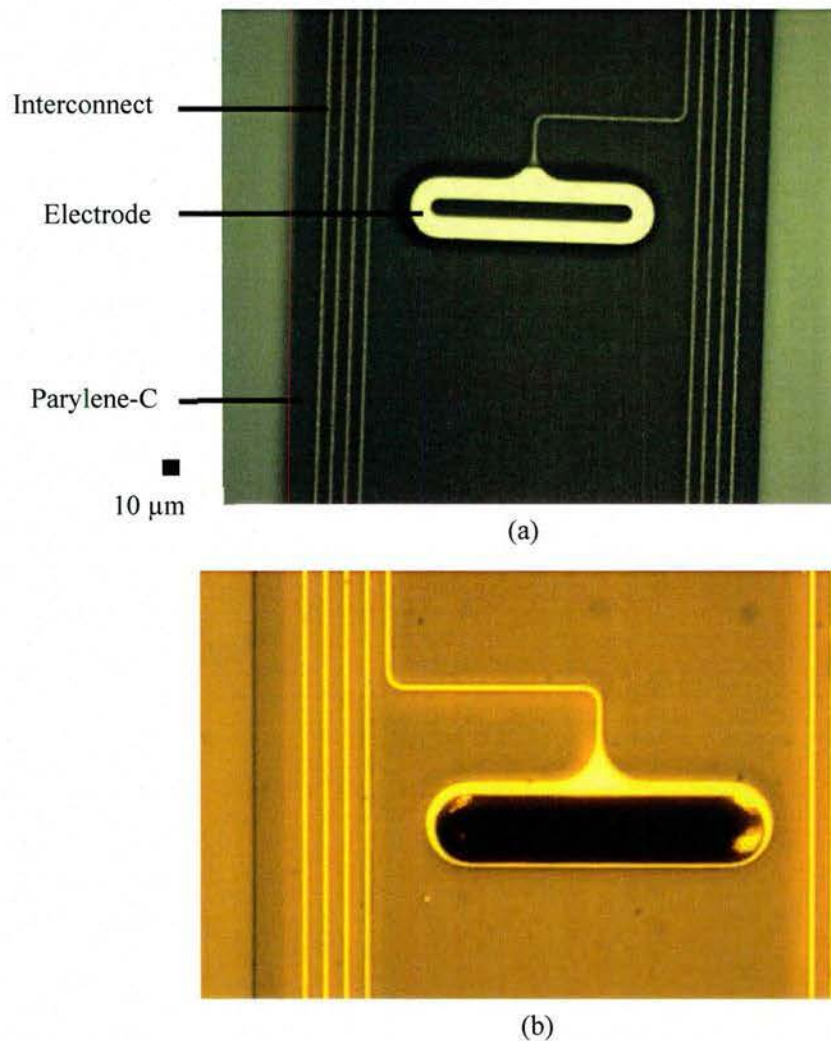


Figure 31. Optical images of fabricated protruding electrodes on Si. (a) After grayscale etch, before patterning and deposition of second layer of Pt; shown is the “raceway” design of the lower Pt layer enabling the interlocking protruding parylene layer. (b) After probe transferred onto BGL7080 coated glass, where the image is taken looking through the glass and transparent BGL7080 coating.

### 7.2.6 Probe transfer process

A process to transfer completed probes from its silicon substrate to a glass handle substrate proves essential for subsequent needle assembly (see section 7.5.3). The process development effort is documented in [2] and this section provides a brief summary. Probes are fabricated on a silicon substrate that acts as a carrier during the process steps. The probes must be released from their carrier substrate at some point to create functional probe-needle assemblies. Probe release prior to needle assembly is not viable as the released probe does not remain flat and is fragile and easily broken when manipulated manually. Thermal annealing techniques to improve parylene-parylene adhesion, which is desired in low leakage probes, also improves parylene adhesion to the silicon carrier substrate. This strong adhesion prohibits probe release

from the silicon substrate after assembly of the needle. The engineering solution is an intermediate process step that transfers the probes from the silicon carrier substrate to a glass handle substrate. A sacrificial adhesive bonds the probes to the handle wafer and releases the probes when exposed to the appropriate adhesive etchant. The key is finding the appropriate adhesive, bonding technique, and etchant that are compatible with the needle and probe materials.

Illustrations of the general transfer processes are shown in Figure 32. (a)-(b) The silicon carrier substrate with the probes is pressed onto the adhesive that is spin cast onto the handle substrate using a device bonder. (c) The silicon is then removed using a combination of reactive-ion etching (RIE) and  $\text{XeF}_2$ . After the transfer step (c), there are three process variants, labelled 1, 2, and 3 in Figure 32. In process variant #1, (d1) the adhesive is etched to release probes, (e1) the probe is manually placed flat onto a separate glass substrate, (f1) a polyurethane mold is attached to the glass substrate, (g1) CMC/glucose is molded to create the needle, and (h1) the probe-needle assembly is manually detached from the glass substrate. In process variant #2, (d2) partial timed etch of the adhesive layer undercuts the needle, (e2) a polyurethane mold is attached to the glass substrate, (f2) CMC/glucose is molded to create the needle, and (g2) the probe-needle assembly is manually detached from the glass substrate. In process variant #3, (d3) a pre-molded needle is attached to the transferred probe using gelatin as an adhesive, (e3) the adhesive layer is etched, releasing the probe-needle assembly.

Table 4. Adhesives and corresponding etchants explored for the probe transfer process.

<b>Trial</b>	<b>Variant</b>	<b>Adhesive</b>	<b>Etchant</b>	<b>Result</b>
A	#1	PDMS	Dynasolve 220	Damages CMC/glucose needle material
B	#2	Crystal Bond	Acetone	Acetone affects polyurethane mold
C	#2	BGL 7080	IPA	Mold is ok; issues with residual stress in needle
D	#3	BGL 7080	IPA	Successful, no damage to needle or probe

The various combinations of process variants, adhesives and corresponding etchants are tabulated in Table 4. The ultimate successful process variant is trial D in Table 4 using BGL 7080 as adhesive, isopropyl alcohol (IPA) as solvent, and needle attachment using methods in section 7.5.3 with  $\text{O}_2$  plasma adhesion improvement in section 7.5.3.4. The following provides a synopsis of the trials.

PDMS as adhesive and Dynasolve 220 as etchant were a first exploratory choice. However, from insertion studies, it was found that the PDMS etchant, Dynasolve 220, significantly reduces the dissolution rate of CMC-glucose. Hence, in order to eliminate the exposure of the CMC-glucose needles to Dynasolve 220, instead of performing molding on the PDMS substrate and releasing the probe after molding, the release was performed in step (d1) in Figure 32 prior to molding. The released device was then placed flat on a glass substrate prior to molding. Although this process resulted in some functional released probes, the manual placement of the released device on the glass substrate followed by subsequent molding resulted in crumpled cables. The process suffered from poor yield due to this step.

Further insertion tests revealed that the dissolution properties of CMC-glucose are unaffected by acetone. As a result, a series of process variants were explored using adhesives that are dissolvable in acetone. Initial work using the photoresist AZ4620 was unsuccessful largely because of poor adhesion between the resist and parylene-C and between the resist and glass when the solvent is in the resist is removed completely. The devices delaminated during the Si etch step. If the solvent is not removed completely, the devices are damaged from the bubbles formed during subsequent processing.



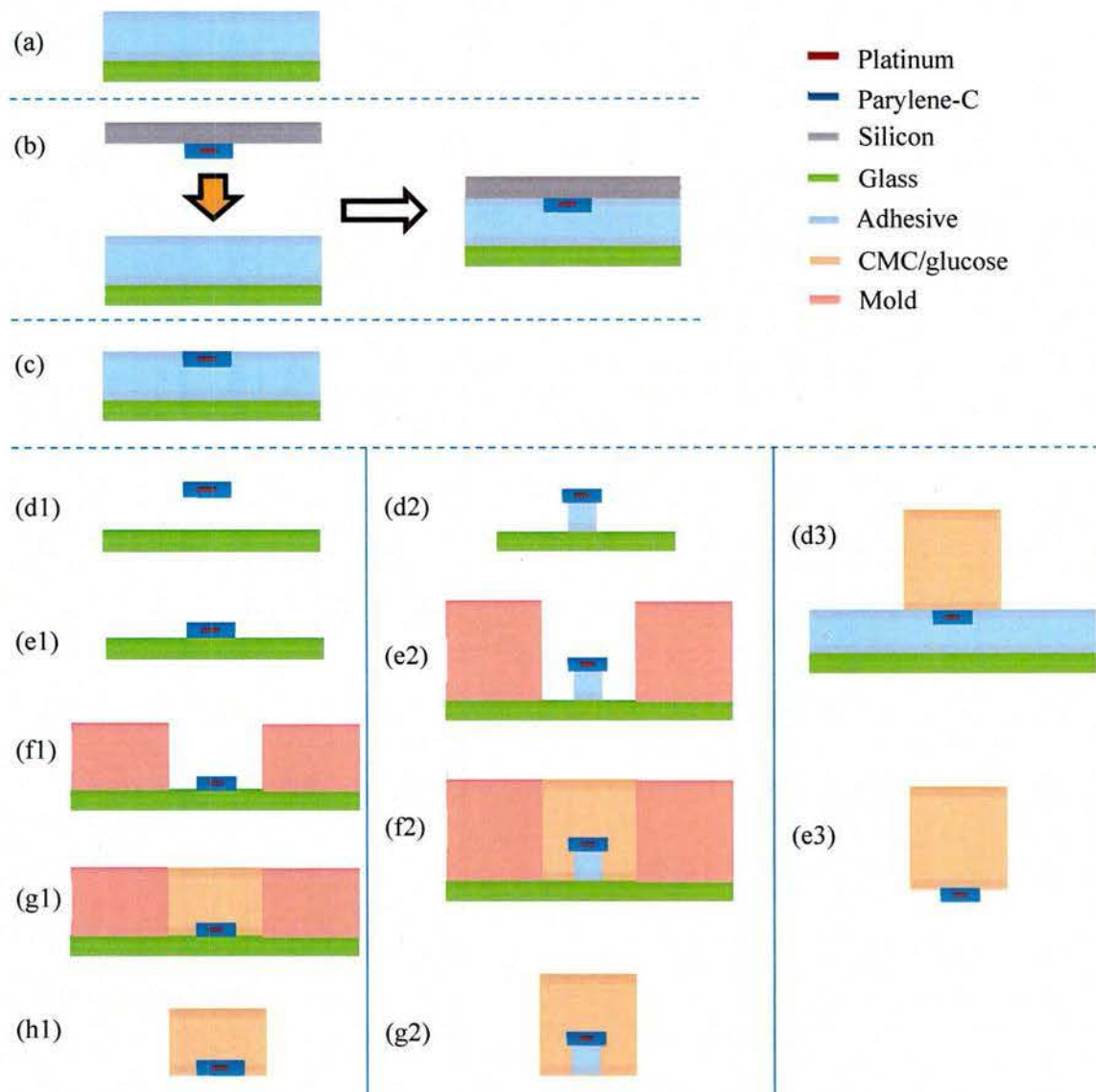


Figure 32. Probe transfer processes. (a) Adhesive is spin cast onto the glass handle substrate. (b) The probe with its silicon carrier substrate is bonded to the glass handle substrate. (c) All silicon is removed using  $\text{SF}_6$  RIE followed by  $\text{XeF}_2$  vapor etch. (d1)–(h1) Process variant #1: Additional transfer, then needle molding. (d2)–(g2) Process variant #2: Adhesive undercut, then molding. (d3)–(e3) Process variant #3: Needle attachment.

Crystal Bond 509 (Aremco Products, Inc., Valley Cottage, NY), an acetone dissolvable mounting adhesive, was explored as a next alternative as the adhesion between Crystal Bond 509 and most materials is good. Process variant #2, with the removal of the release step prior to molding resolved the problem of crumpled cables. A completed device is shown in Figure 33 with its assembly to the printed circuit board to an Omnetics connector (Omnetics Connector Corp., Minneapolis, MN), ready for testing. However, there were significant yield issues with these devices. The use of acetone during the release in step (f2) of Figure

32 resulted in curling of the polyurethane based mold. This curling subsequently resulted in the breakage observed in some devices, resulting in yield loss in functioning electrodes.

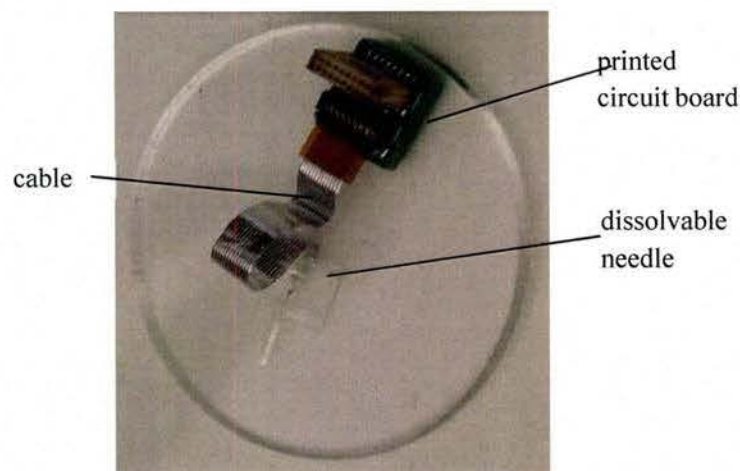


Figure 33. Completed device, assembled with a printed circuit board connected to the cable.

In order to improve on the yield, an IPA dissolvable adhesive, BGL7080 liquid wax (AI Technology Inc., Princeton Junction, NJ) was explored next. The process is identical to the Crystal Bond 509 process variant #2 but with BGL7080 replacing Crystal Bond 509 and IPA replacing acetone. The use of IPA as the release solvent results in a process that is fully compatible with molding. A transferred probe, with parylene-NL-TiO<sub>2</sub> encapsulation of the wiring, is shown in Figure 34 and molded and released devices with parylene-only encapsulation are shown in Figure 35.

The application of the transfer process is not limited to parylene-C only probes. The transfer process is also carried out using BGL 7080 with probes incorporating NL which would aid in improving the barrier properties of the probes. A probe that is transferred is shown in Figure 36.

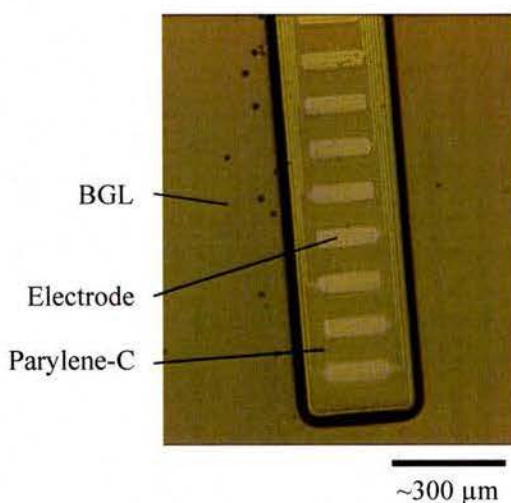


Figure 34. Transferred parylene-NL-TiO<sub>2</sub> encapsulated probe on BGL7080 coated glass.



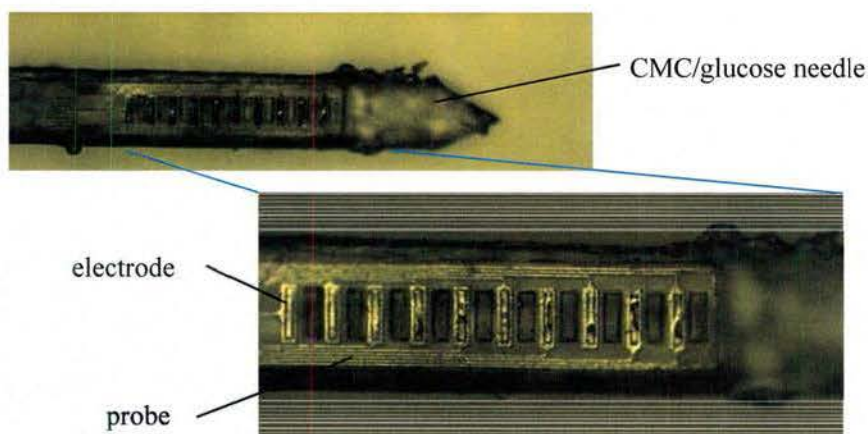


Figure 35. Molded and released probe-needle assembly using BGL7080 and process variant #2.

Preliminary yield using BGL7080 as a release adhesive meets the target yield of 50%. The yield was determined by the integrity of the self-test structures (Pt 'loops'). Four out of five probes were transferred successfully onto the BGL7080 coated glass. Two out of three probes were molded and released successfully. Thus, the yield of this first run in the BGL7080 process is 53%.

A probe-needle assembly was fabricated using BGL7080 as an adhesive layer and a pre-molded 3D-tip needle design (see section 7.5.2.4) attached with the process variant #3. The electrical test loops fabricated with the new process flow are intact after molding and release based on the resistance of the loops. Optical images of the molded and released devices are shown in Figure 36.

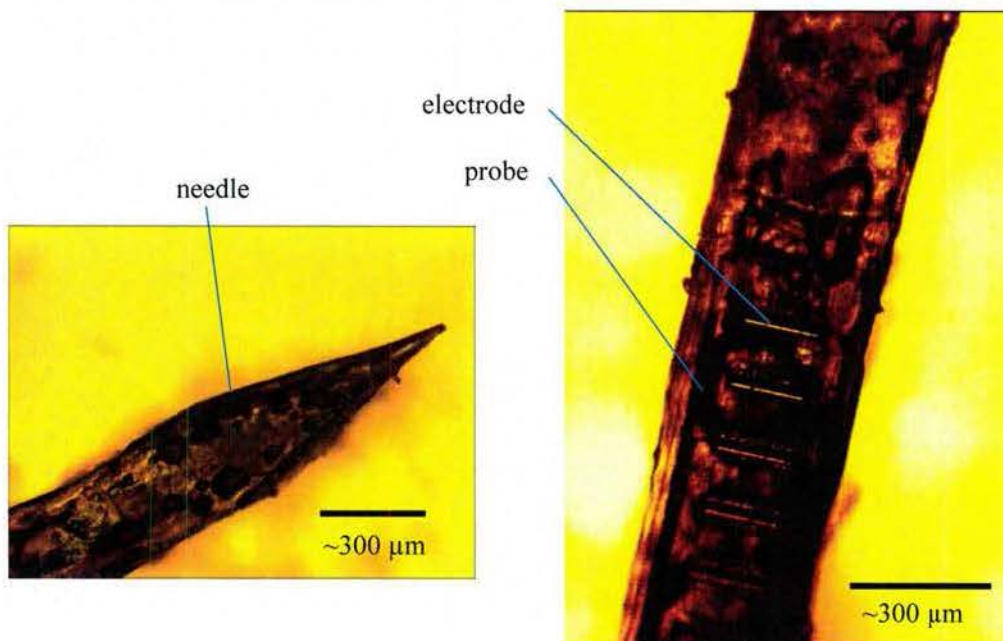


Figure 36. Released needle and probe using BGL7080 as an adhesive and process variant #3. The pre-molded CMC needle design has a 3D sharp tip.

The transfer process is also performed on multi-probe array chips which are much larger in area and with thicker parylene-C. Appropriate process parameters for the transfer of probes onto a glass substrate coated with BGL7080 liquid wax led to successful transfer as shown in Figure 37. After appropriate modification, two-shank probes and four-shank probes of two different thicknesses (two 2.2  $\mu\text{m}$  thick layers and two 4.5  $\mu\text{m}$  thick layers) were transferred successfully. For larger probes, the main difference in processing is the bonding time during transfer and the pressure applied. Since the maximum force allowable by the M9A device bonder is 90 N, the bonding time is increased significantly for these two-shank and four-shank probes.

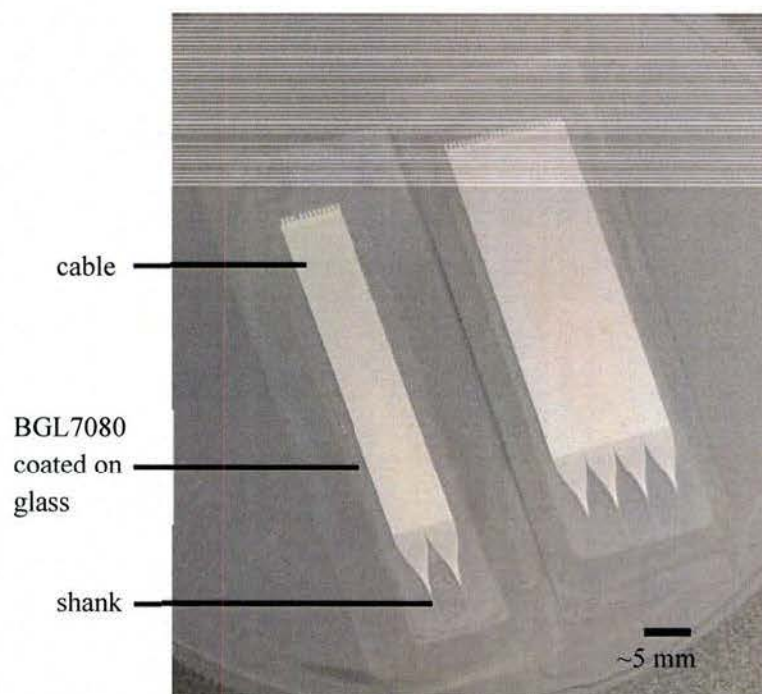


Figure 37. Two-shank probe (with two 4.5  $\mu\text{m}$ -layers of parylene-C) and four-shank probe (with two 2.2  $\mu\text{m}$ -thick layers of parylene) transferred onto BGL7080 coated glass.

### 7.3 Silicon surrogate probe

A probe with platinum interconnect and electrodes, and insulated by parylene-C, was fabricated on a silicon needle as a first step to *in vivo* validation of the parylene-platinum wiring. Results are documents in [5], with a short summary given in this section. The process steps to fabricate the needles are shown in Figure 38. Following fabrication of the probes on Si, the devices on Si (fabricated on a thinned Si substrate which defines the thickness of the substrate) is bonded to glass using BGL7080. Using a Cr hard mask, the devices are then etched by DRIE to define the outline of the probe.

A fabricated probe is shown in Figure 39. The dimensions of the needle (300  $\mu\text{m}$  width) are made to match with the dimensions of the CMC-glucose needle for comparison purposes. The needles were inserted into a mouse. Histology was performed which confirmed insertion into the desired location (substantia nigra). Spikes were recorded successfully as shown in Figure 40.



However, no spikes were recorded for the CMC-glucose needles. This is possibly due to the time required to disperse the CMC-glucose. In order to fully evaluate functionality of probes embedded in CMC-glucose needles, more chronic studies are required.

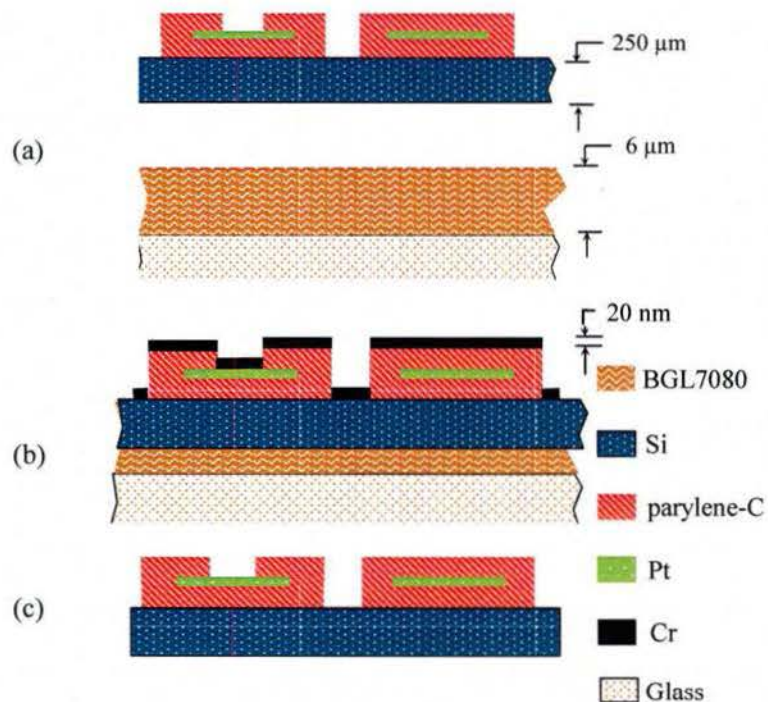


Figure 38. Process for parylene probe on an integral silicon needle. (a) Spin coat BGL7080 on a glass chip and use it as a handle to glue thinned Si chips. (b) Pattern and etch Cr as a hard mask. (c) Etch Si using DRIE and release with IPA.

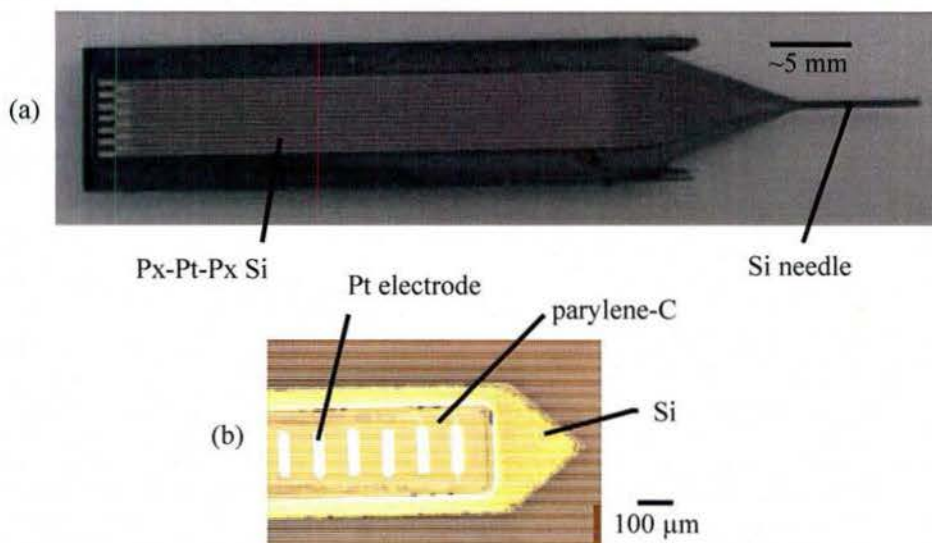


Figure 39. Parylene probe on an integral silicon needle. (a) Full probe sample. (b) Probe tip.

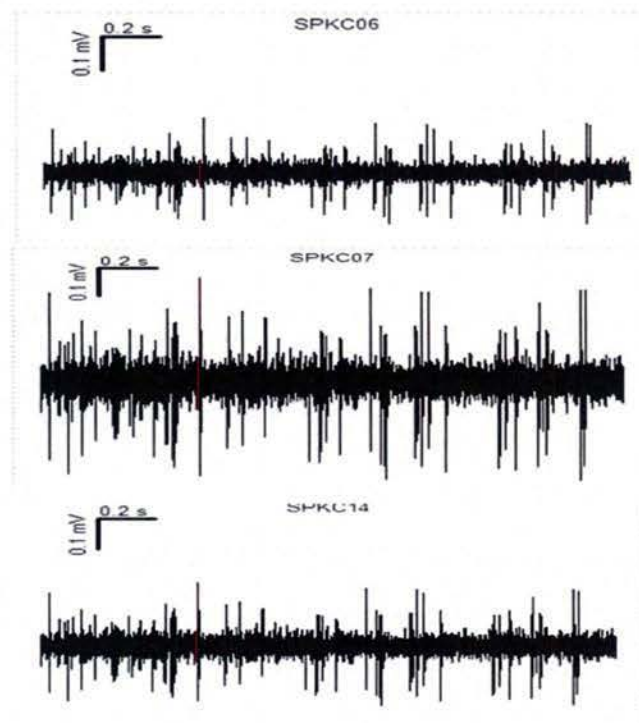


Figure 40. Recordings from three different electrodes on the parylene probe on an integral silicon needle inserted into a mouse brain.

## 7.4 Electrical stability studies

### 7.4.1 Lumped-element impedance modeling

A parametrized lumped-element circuit model allows the effects seen in electrical impedance spectroscopy (EIS) measurements to be understood by fitting measured data and assessing the outcomes. The physical basis of the model is shown in Figure 41. Resistance around 1-2 k $\Omega$  models ionic conduction in the PBS (and also the metal wiring in the test structures). Due to the spatial distribution of the leakage along the wire, the model includes several parallel RC branches. The charge transfer across the parylene layer is ideally purely capacitive, with capacitance  $C_{px} = 1.5$  pF for the test structures. Ideal resistance through the parylene layer corresponding to the resistivity of the dry parylene is  $R_{px} = 200$  T $\Omega$ . The charge transfer to the platinum results in a double-layer capacitance of  $C_{dl} = 50$  nF, and a parallel charge transfer resistance of 100 M $\Omega$ . For the samples with NL, the total capacitance across the NL layer to the 10  $\mu$ m-wide by 1 cm-long platinum wiring is  $C_{NL} = 200$  pF, while the resistance through the NL layer is 80 T $\Omega$ . The resistance of the titania adhesion layer on top of the NL layer is  $R_{Ti} = 1$  G $\Omega/\mu$ m.

A nonlinear least squares fit of lumped parameters to the experimental EIS data is shown in Figure 42. To account for the distributive nature of leakage capacitance, a pseudo-capacitance is used for one of the paths through the parylene. The impedance of this element is characterized by  $Z = 1/((j\omega)^n Q)$ , with  $n$  between 0 and 1 ( $n=1$  corresponds to a normal capacitor).

The capacitive behavior of the cases with and without NL is similar until around 2000 h, with  $C_{px1} \approx 7$  pF. This parylene capacitance is larger than expected and indicates that the parylene dielectric constant might be higher in saline than the theoretical value. For the case with only parylene, the capacitance



reaches a stable value after around 200 h, meaning the dielectric constant has reached steady state after this time. After 2000 h, the capacitance in the NL case starts increasing, which points to the indication of some leakage occurring at the parylene-NL interface. This leakage effect is also evidenced by the larger decrease in the parylene resistance  $R_{Px}$  for the case with NL. In both cases,  $R_{Px}$  has a similar order of magnitude around 10-100 G $\Omega$ , significantly smaller than the calculated value obtained from resistivity of parylene. The conduction through the parylene layer is likely dominated by water-mediated ionic conduction paths through pores or the swollen polymer.

Interestingly, the leakage resistance along the interface, which is modeled by  $R_L$ , increases with time. However the value of  $R_L$  is small compared to the overall system impedance so the changes in its value might be a numerical artifact of the fit and not be an accurate reflection of the physical situation. Finally, the capacitance of the NL layer is on the order of the expected value; one of the paths has a significantly larger capacitance, which indicates that it contributes more strongly to the overall impedance.

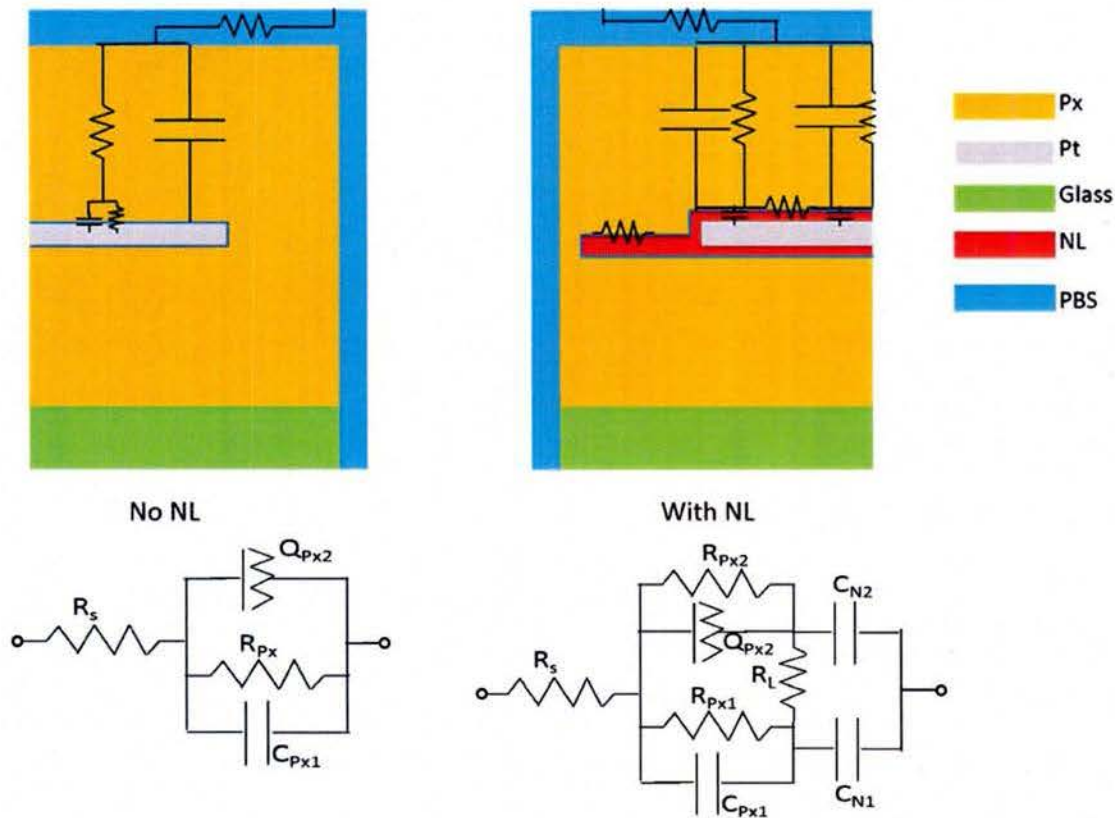


Figure 41. Parylene-only (left) and parylene-NL (right) lumped models indicating the resistive and capacitive couplings from the saline to the metal wiring. Top: cross-sectional schematic diagrams of the probe wiring. Bottom: respective lumped circuits.

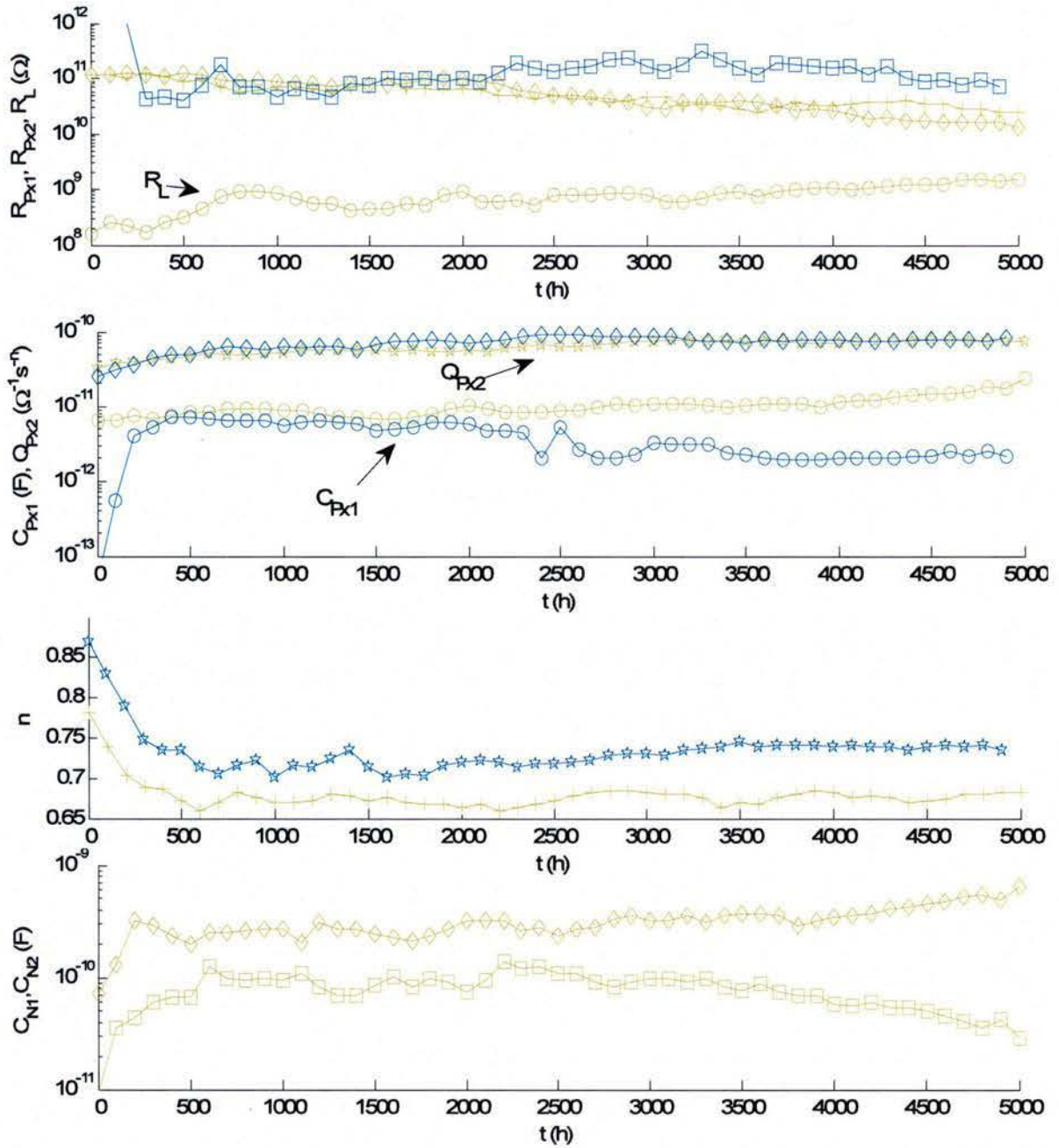


Figure 42. Best fit for the parameters (averaged over 48 channels). Blue lines correspond to parameters for parylene alone, yellow lines correspond to parameters for parylene-NL.

#### 7.4.2 Finite-element impedance modeling

FEA simulations were performed in COMSOL to further the understanding of the relationship between insulation degradation and impedance. A cross-section schematic of the simulation model is shown in Figure 43. The parameters of the simulation are the ionic conductivities of the leakage path through parylene and of the leakage path along the oxide layer ( $\text{Al}_2\text{O}_3$  or NL). Figure 44 shows that proper



adjustment to the leakage-path conductivities leads to a match to the measured impedance, which helps uncover the mechanism of impedance decrease with time. The simulation uses an arbitrary fixed thickness for the width of these leakage paths (set to 10 nm). In reality, this width may change to affect the ionic conductance of the leakage path. In the simulation, the relative changes in PBS leakage path conductivity compound both the effects of conductivity and geometric effects of the leakage path on the impedance. Therefore, the actual values of the conductivities are not necessarily indicative of changes in the actual conductivity, but may be due to changes in the leakage path geometry. The relative variations in conductivities inform the importance of each leakage path on the value of impedance. While this simulation can help understand the mechanism of leakage across the interfaces of the insulation, it does not take into account bulk resistivity, which also may change over the course of the experiment.

In the case of the parylene/Al174-Al<sub>2</sub>O<sub>3</sub> sample shown in Figure 44, the initial leakage path conductivity is significantly smaller than the bulk conductivity ( $S_{\text{alumina}} \sim 10^{-14}$  S/m for Al<sub>2</sub>O<sub>3</sub> and  $S_{\text{parylene}} \sim 10^{-13}$  S/m for parylene-C). The oxide (alumina) leakage conductivity decreases abruptly and reaches a steady value after less than 500 h. The parylene leakage conductivity decreases more gradually until it reaches a steady value after around 2000 h. This behavior matches conclusions that the interface between the parylene and the Al<sub>2</sub>O<sub>3</sub> is the critical interface to improve to achieve long lasting insulation. However, section 7.4.4 indicates that Al<sub>2</sub>O<sub>3</sub> etches in PBS and thus is a very poor long term insulator.

In the case of the parylene-NL/TiO<sub>2</sub> sample, the initial leakage conductivities are higher for both the parylene leakage path and the ceramic encapsulating layer leakage path (the NL/TiO<sub>2</sub> layer in this case). This ‘leakage’ is expected for the NL/TiO<sub>2</sub> layer since the TiO<sub>2</sub> interface is slightly conductive and so acts as a conductive path parallel to the NL, which has the same effect as a leakage path that may occur due to saline penetration. The higher initial conductivity of the parylene leakage path explains the lower low frequency impedance. Possible re-deposition during the NL/TiO<sub>2</sub> etching step might explain the higher conductivity. Over the relatively short time durations (*e.g.*, less than 500 h), the increase in NL/TiO<sub>2</sub> leakage conductivity is more pronounced than that of the Al<sub>2</sub>O<sub>3</sub> leakage conductivity. However, eventual corrosion of the alumina layer, which is sped up at high temperature in PBS, leads to an assessment of better overall leakage performance for NL/TiO<sub>2</sub>.

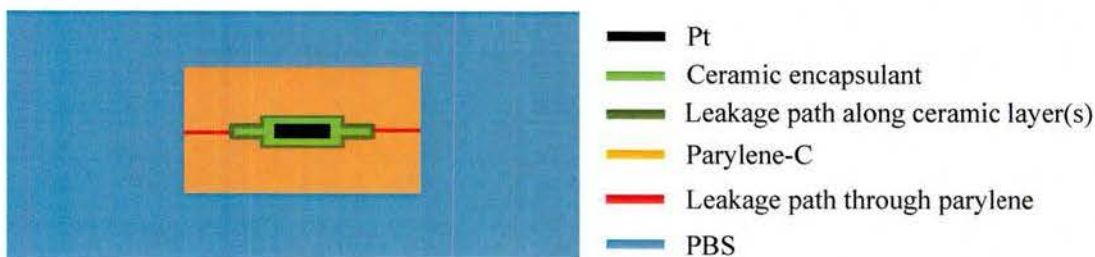


Figure 43. Impedance FEA simulation cross-section model (not to scale). A sinusoidal excitation voltage is applied from a boundary at the edge of the PBS; Pt is electrical ground in the simulation. Insulation loss is considered via a narrow leakage path in the parylene having higher conductivity. A similar high conductivity path can exist surrounding the ceramic encapsulant layer; its effect is similar to that of the TiO<sub>2</sub> layer surrounding the NL.

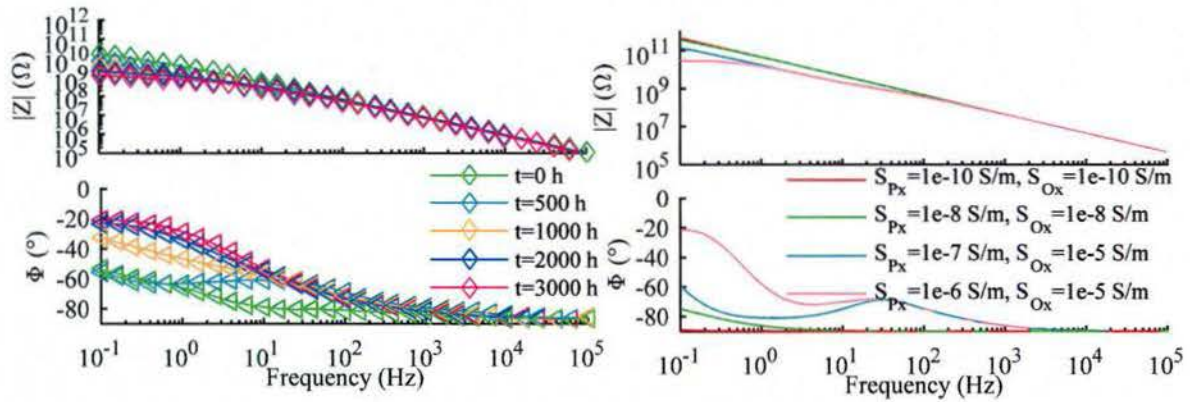


Figure 44. Left: Measured impedance Bode plot of  $\text{Al}_2\text{O}_3$  sample at various time points after insertion in 1x PBS at room temperature. Right: Simulated impedance using different values for the ionic conductivities of the parylene leakage path ( $S_{Px}$ ) and the ceramic (oxide) leakage path ( $S_{Ox}$ ).

### 7.4.3 Electrochemical Impedance Spectroscopy setup

Measurements on test structures described in section 7.1.4 provide results for characterization of the insulation of parylene and parylene/ceramic thin films. To this end, the test structures are attached to a flexible cable and inserted into vials containing 1x PBS. Electrochemical impedance spectroscopy (EIS) is a method of measuring the current amplitude through the electrode under test when a small sinusoidal voltage (30 mV amplitude was used) is applied between the electrode under test and a large counter electrode located in the same vial. The sinusoidal frequency spans between 0.1 Hz and 100 kHz for the measurements. Neural probe impedance is typically characterized at 1 kHz because of its importance in the frequency content of neural spike signals. For insulation characterization, near-DC leakage currents cause a reduction in the low frequency impedance, typically as a result of undesired resistive leakage paths in the insulation. Therefore insulation quality is characterized by the impedance at 0.1 Hz, which is as low of a frequency as is practically considered.

### 7.4.4 Insulation leakage tests at 0.1 Hz

The target low-frequency impedance (at 0.1 Hz) for what are considered ‘low leakage’ films is greater than 10 GΩ. Figure 45 shows the leakage impedance at 0.1 Hz over 6 months for the test structures described in section 7.1.4 for the four primary types of thin-film insulation explored in this project. The best performance is obtained for samples using only parylene-C insulation with no additional modifications. The impedance after 6 months of these test structures is around 15 GΩ ± 5 GΩ. The impedance behavior at 0.1 Hz for the parylene-only wiring decreases exponentially with a time constant of 6.6 months.

Parylene- $\text{Al}_2\text{O}_3$  and parylene-NL structures suffer from low adhesion between the parylene layer and the oxide, resulting in lowered impedance. Delamination is visible for the parylene-NL structures after 6 months in PBS.

Because the design of the Px-NL- $\text{TiO}_2$  test structures is modified from the other insulation samples, an exact quantitative comparison with the previous structures is not possible. Compared to structures using only parylene as an insulation, the impedance at 0.1 Hz and at room temperature is of a similar order of magnitude. The increased adhesion with parylene due to the addition of the  $\text{TiO}_2$  layers results in a significantly larger impedance than compared to parylene-NL (without the  $\text{TiO}_2$  adhesion layers). However,



the impedance of the Px-NL-TiO<sub>2</sub> structures is lower than that of the parylene-only structures. The adhesion of parylene to the TiO<sub>2</sub> layer, while an improvement over the adhesion to Al<sub>2</sub>O<sub>3</sub>, is presumably still not as high as parylene adhesion to platinum. Moreover, TiO<sub>2</sub> has a small but finite DC conductance, which also reduces the overall impedance of the insulation.

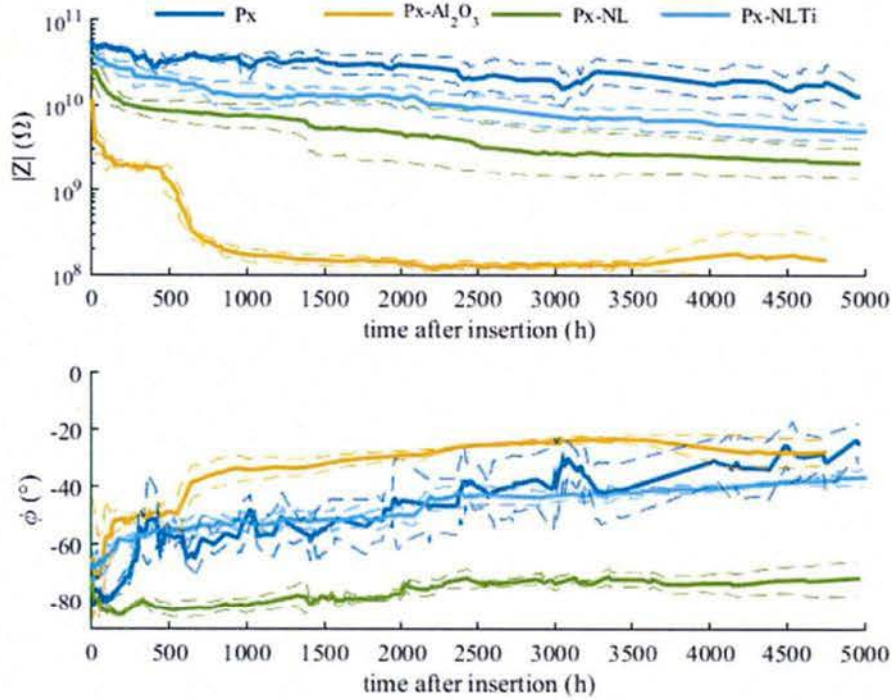


Figure 45. Insulation impedance at 0.1 Hz for four types of insulation over 6 months in PBS. Impedances are averaged over  $n=3$  samples in each case, with dashed lines indicating standard deviation.

While the impedance stability of the parylene-only test structures (fixated to a glass substrate) seems to indicate that parylene alone could be a sufficiently stable insulation for even medium-term experiments, results of released probes show unacceptable leakage levels using only parylene as an insulator (see section 7.4.11). The advantage of the additional NL/TiO<sub>2</sub> insulation is also noticeable at higher temperature (see section 7.4.6) or when high voltage is applied to the electrode as is required for stimulation (see section 7.4.7).

In order to more clearly evaluate the failure behavior of each structure, additional analysis is based on the yield of the structures. Each of the samples tested has 16 channels. The yield of each structure was determined based on the value of the impedance magnitude at 0.1 Hz: if  $|Z| > 10^{10} e^{-t/\tau}$  Ω, with  $\tau = 3000$  h, then the channel in question degrades normally and is considered a success. Otherwise the degradation of the impedance is faster than expected and is considered a fail. The average impedance and yield of the different structures is shown in Figure 46.

As expected, the yield for structures containing alumina (parylene-Al<sub>2</sub>O<sub>3</sub>) is very low, due to the poor adhesion of the parylene to the alumina coupled with the dissolution of alumina in the PBS. Broken or disconnected wires account for the few high magnitude channels reported.

The yield of the nanolaminate structures without the titania adhesion layers (parlylene-NL) is low because of the low overall impedance of the channels. The impedance behavior is not significantly different for the low impedance channels compared to the high impedance ones. The samples with no ALD encapsulation (parlylene-only) have about 25% of channels failing due to defects, leading to significantly lower impedance for those channels. When the nanolaminate-titania encapsulation is added (Px-NL-TiO<sub>2</sub>), there are virtually no defective channels. This enhanced yield might be the result of wafer-to-wafer manufacturing variation as all the data for each insulation type comes from a single wafer. However testing of additional parlylene wafers with the modified (version 2) design still exhibit a lower yield than the Px-NL-TiO<sub>2</sub>, indicating that the additional nanolaminate-titania ALD layer stack does limit the effect of defects in the insulation.

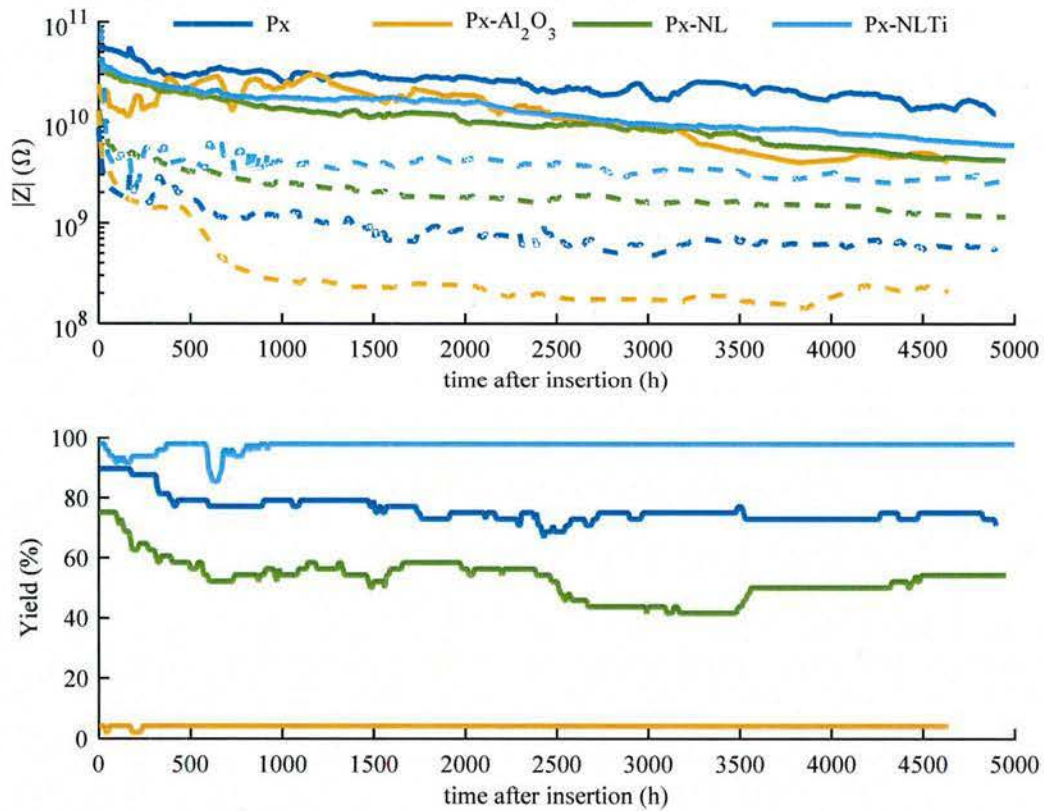


Figure 46. Impedance at 0.1 Hz over 6 months in PBS and yield over  $n=48$  channels for each structure. The average impedance of high magnitude channels is shown in full lines, while the impedance of low magnitude channels is shown in dashed lines.

The magnitude and time constants obtained from fitting the impedances to  $|Z| = Ae^{-t/\tau}$  are shown in Table 5. All insulation types are fit to the high magnitude impedance plots, except for parlylene-Al<sub>2</sub>O<sub>3</sub>, which is fit to its low magnitude plot to reflect the very low yield.



Table 5. Low-frequency leakage performance of four types of thin-film insulation. \*The parylene- $\text{Al}_2\text{O}_3$  time constant is extracted after the magnitude of the leakage resistance falls to unacceptable levels.

	parylene-only	parylene- $\text{Al}_2\text{O}_3$	parylene -NL	parylene -NL- $\text{TiO}_2$
Magnitude $A$ ( $\text{G}\Omega$ )	29.8	0.171	11.2	26.1
Time constant $\tau$ (days)	198	6625*	119	134

The impedance magnitude variation for the exploratory processing modifications is shown in Figure 47. Aside from the ion mill descum (IM) treatment without alumina encapsulation, the samples maintain greater than  $1 \text{ G}\Omega$  impedance at  $0.1 \text{ Hz}$  over the full two month period. With the additional exception of the alumina encapsulation, the variations between the impedance of the different treatments are within the range of inter-sample variation; *i.e.*, it is not clear that any single treatment provides significant benefit.

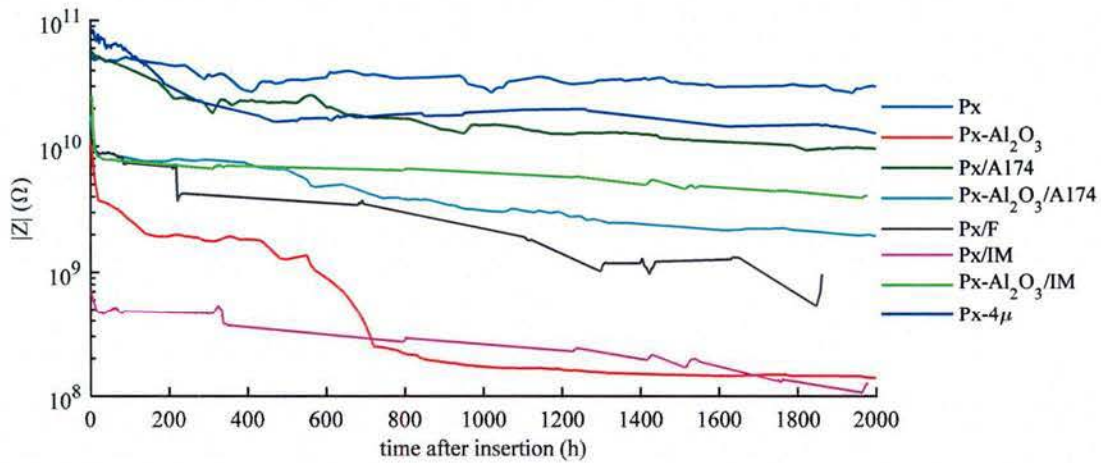


Figure 47. Impedance at  $0.1 \text{ Hz}$  of exploratory modifications on the structures. Typical impedance for  $n=1$  sample is shown. A174 is a pre-treatment adhesion-promotion chemistry between parylene layers. “F” is plasma fluorination of the surface between parylene layers. “IM” is ion-mill descum treatment of the surface between parylene layers. “ $4\mu$ ” denotes the parylene samples with  $9 \mu\text{m}$  overall thickness.

#### 7.4.5 Wiring insulation impedance at $1 \text{ kHz}$

The electrode impedance at  $1 \text{ kHz}$  is typically used to characterize neural probes. However, in the case of the test structures, there is no exposed electrode and the impedance will therefore be high. Low insulation impedance corresponds to a low SNR for neural recordings. The insulation impedance of the test structures at  $1 \text{ kHz}$  is an indicator for the contribution of the probe wiring as compared to the normal electrode impedance. Therefore, high values of the insulation impedance are required otherwise a significant portion of the overall impedance originates from the distributed wiring instead of the electrode, resulting in increased noise for neural recording. Figure 48 shows the insulation impedance at  $1 \text{ kHz}$  over a period of 6 months for the same structures considered previously. Both parylene and parylene-NL- $\text{TiO}_2$  samples perform similarly with impedances at  $1 \text{ kHz}$  of between  $7\text{--}10 \text{ M}\Omega$  over the entire experiment. The parylene- $\text{Al}_2\text{O}_3$  sample experiences some initial decrease over the first  $\sim 1000 \text{ h}$  before stabilizing around  $5 \text{ M}\Omega$ .

The insulation impedance of the parylene-NL sample without any special adhesion layer at 1 kHz decreases dramatically over the first 500 h and then experiences abrupt drops over the course of the experiment; its impedance reaches 500 k $\Omega$  after 3000 h. This poor behavior the parylene-NL is caused by the delamination of the parylene layer from the underlying NL layer; after a short while the insulation is entirely provided by the thin NL layer, which allows significant capacitive coupling to the wire. The impedance is not a direct dc short circuit, but rather exposure of the PBS to the outside interface of the thin NL coating that creates a relatively large coupling capacitance to the wiring.

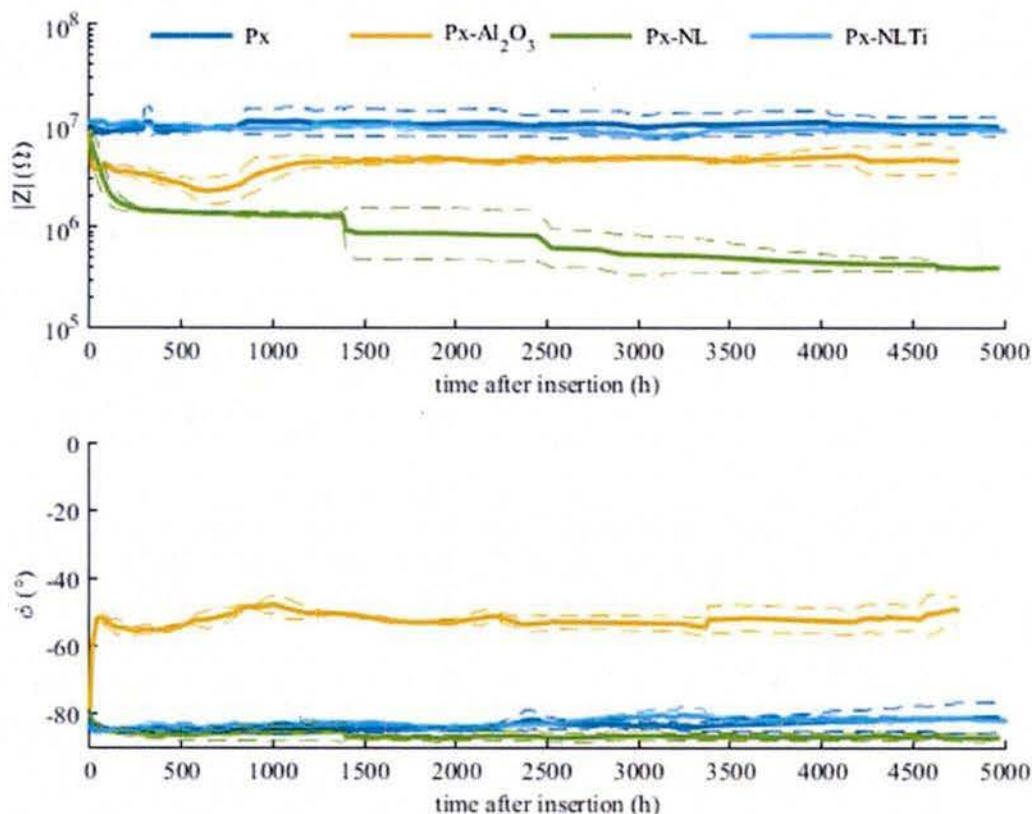


Figure 48. Insulation impedance over 6 months in 1x PBS at 1 kHz. Impedances are averaged over  $n=3$  samples in each case, with dashed lines indicating standard deviation.

#### 7.4.6 High temperature testing

Accelerated impedance studies at higher temperature (60°C) accelerate the degradation of the parylene insulation layer and of the insulation performance of ALD-deposited oxide layers. Samples were inserted in heated PBS and removed periodically to perform impedance measurements at room temperature; results are shown in Figure 49. Under this high temperature aging experiment, the impedance of parylene-only structures drops very rapidly to less than 1 G $\Omega$  within ~50 h. The impedance at 0.1 Hz of structures insulated with Al<sub>2</sub>O<sub>3</sub> is even lower than that of parylene-only structures. This behavior is expected as alumina etches in hot saline solution. Interestingly, the parylene-Al<sub>2</sub>O<sub>3</sub> combination shows worse performance than either parylene or Al<sub>2</sub>O<sub>3</sub> alone; this might be caused by the poor adhesion of Al<sub>2</sub>O<sub>3</sub> to



parlyene (*i.e.*, worse than  $\text{Al}_2\text{O}_3$  to glass), causing delamination and additional mechanical stress on the insulation. After a long time ( $t > 600$  h) the impedance experiences sharp changes from low to high impedance. In this case, the structure is probably mechanically damaged leading to lower total metal area connected.

The leakage impedance of  $\text{TiO}_2$  structures is always very low; this is because the conductivity of  $\text{TiO}_2$  is non-zero and high relative to parlyene-C, making it a poor insulator for neural probe applications. The measured dry resistance from the test structure to the counter electrode is around  $200 \text{ k}\Omega$  (without passing through the saline).  $\text{TiO}_2$  is therefore not appropriate by itself as an additional insulating layer.

The impedance of the alternating  $\text{Al}_2\text{O}_3/\text{TiO}_2$  ALD nanolaminate (NL) encased test structures is more stable, even at high temperature. There is no catastrophic failure at a short time scale, and the impedance decreases gradually relative to the parlyene-only and parlyene-alumina insulation choices. The leakage impedance is  $1 \text{ G}\Omega$  after 600 h in high temperature PBS. However, the adhesion of NL to parlyene is very poor, and therefore the impedance of parlyene-NL test structures reaches values similar to those of NL-only structures after  $\sim 100$  h in PBS. Moreover, visible large-scale delamination occurs for these samples. In order to obtain usable parlyene-NL structures, an additional adhesion layer must be placed between the parlyene and NL. The parlyene-NL- $\text{TiO}_2$  structures maintain a high impedance ( $>10 \text{ G}\Omega$ ) for around 500 h. After 500 h, failure at high temperature occurs due to delamination of the parlyene from the NL/ $\text{TiO}_2$  layer.

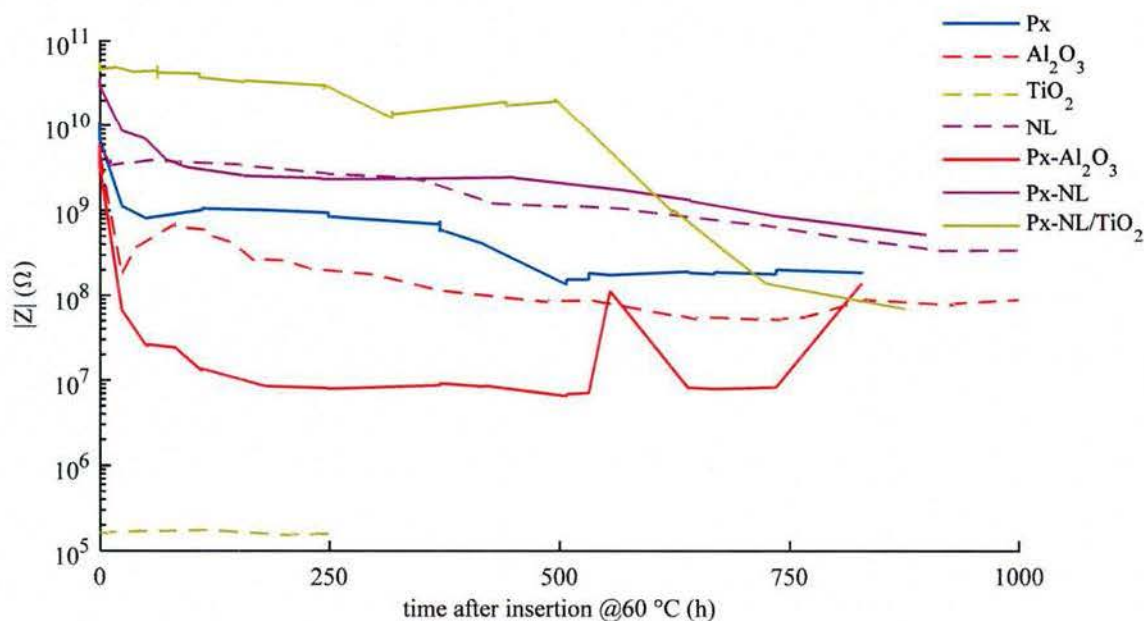


Figure 49. Impedance at 0.1 Hz of various test structures kept in 1x PBS at 60°C. ALD layers were tested alone (dashed lines) as well as combined with an overlay of parlyene (solid lines).

The drastic impedance decrease observed for parlyene under high temperature conditions over the first  $\sim 50$  h of testing does not appear to match the very good stability of parlyene leakage impedance at room temperature for over 5000 h. Given the temperature differential of  $\sim 35^\circ\text{C}$ , the observed acceleration factor of greater than 100x is much larger than the factor  $Q_{10}=2$  commonly used for polymers (we calculate  $Q_{10} > 4.5$ ). Further investigation into high temperature aging is required. As a first step, high temperature

aging of parylene was repeated at the same temperature (60°C) but over a shorter timescale. The results are shown in Figure 50. Drastic jumps from high impedance ( $Z \sim 50 \text{ G}\Omega$ ) to low impedance ( $Z \sim 200\text{--}500 \text{ M}\Omega$ ) indicate that the parylene insulation degrades quickly and unevenly at high temperature. The failure is probably initiated at localized defect sites on the insulation that allow saline penetration. Once saline penetration begins, the failure propagates rapidly along the metal wire. If that is the case, then performing high temperature acceleration might not result in scalable results for the behavior under physiological conditions. That is, the high temperature testing is probably activating failure modalities that will not occur under body temperature.

Additional testing at body temperature (37°C) for parylene-only and parylene-NL/TiO<sub>2</sub> encapsulation yields the results shown in Figure 51. Parylene-NL-TiO<sub>2</sub> performs slightly better than parylene-only insulation after 2000 h. The magnitude and time constants obtained from fitting the impedances to  $|Z| = Ae^{-t/\tau}$  are shown in Table 6.

Table 6. Measurement fit for leakage in parylene-only and parylene-NL-TiO<sub>2</sub> insulation at 37°C.

	parylene-only	parylene-NL-TiO <sub>2</sub>
Magnitude $A$ ( $\text{G}\Omega$ )	37.3	27
Time constant $\tau$ (days)	68	120

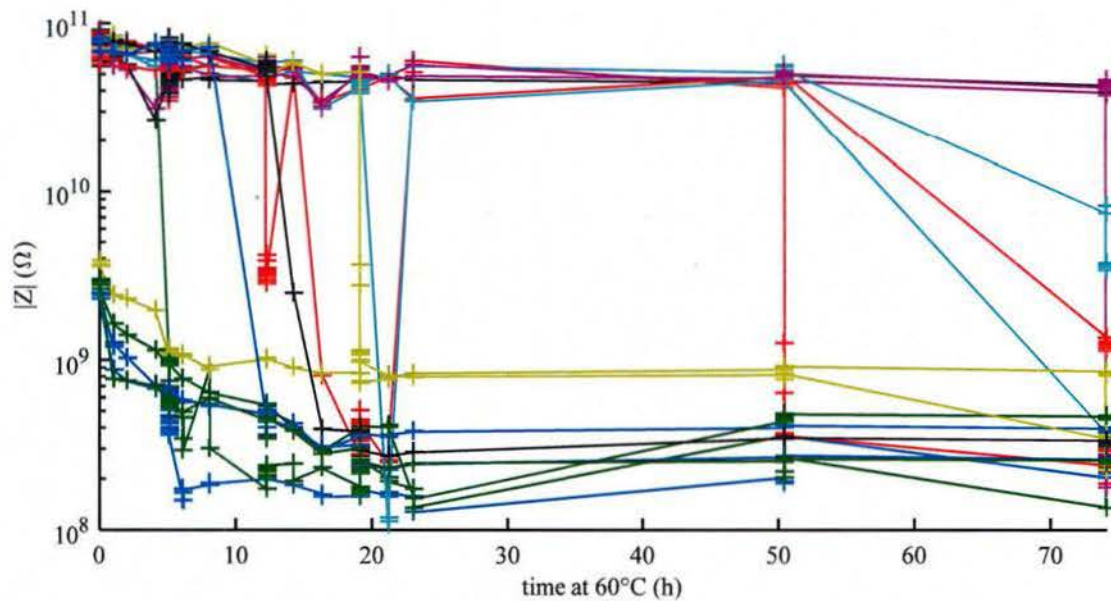


Figure 50. Impedance of parylene encapsulated structures in PBS under accelerated aging at 60°C. All 16 channels in one sample are shown.



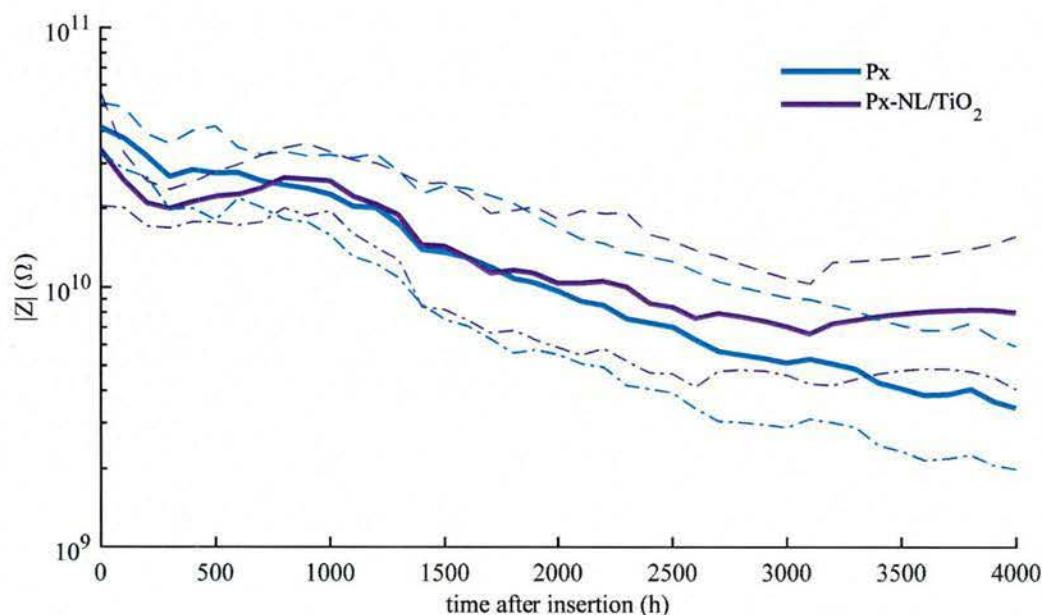


Figure 51. Impedance at 0.1 Hz of structures aged in PBS at 37°C. The impedance shown is the average of high impedance channels ( $|Z| > 10^{10} \Omega$ ) (between 10 and 16 high magnitude channels for each sample).

#### 7.4.7 High voltage insulation tests

In order to validate the probe technology for stimulation, tests were performed on insulation test structures with higher applied voltages. The traditional voltage limit used for stimulation is the water window ( $-0.6$  V to  $+0.8$  V applied with respect to a Ag/AgCl reference), but practical stimulation of nerves might require larger applied voltage at the electrode to ensure sufficient recruitment of the fascicles. ( $\pm 1$  V is frequently used)

If a large enough voltage bias is applied to across the insulation, electrolysis of water will begin at the weakest point in the insulation and gas formation will begin. This will cause mechanical damage to the insulation, further degrading the insulation performance. The comparison between structures having parylene alone as an insulation and structures having an additional NL-TiO<sub>2</sub> ceramic layer is shown in Figure 52. The current across the parylene-only insulated structure starts increasing exponentially above  $\sim 1$  V. Bubble formation is visible using a camera when the current reaches around  $\sim 1$   $\mu$ A. By comparison, even at 5 V, the parylene-NL-TiO<sub>2</sub> provides sufficient insulation to prevent significant degradation of the insulation layer; the current flowing across the insulation is also greatly reduced.

A more realistic test of the effect of neural stimulation on the insulation is to repeatedly apply a voltage in the range used for stimulation. A sinewave with amplitude 0.5 V and frequency 0.1 Hz was therefore applied on test structures insulated with parylene only and parylene-NL-TiO<sub>2</sub> for 2000 h and 4000 h, respectively. The resulting impedance is not significantly different from that of samples left in PBS without the additional voltage applied, as shown in Figure 53. Nonetheless, the applied voltage will accelerate the degradation at defects, which explains the faster decrease in impedance observed for parylene-only insulation. The higher “high magnitude channel” yield (Figure 46) for parylene-NL-TiO<sub>2</sub> means that defects are not as susceptible to occur in these structures.

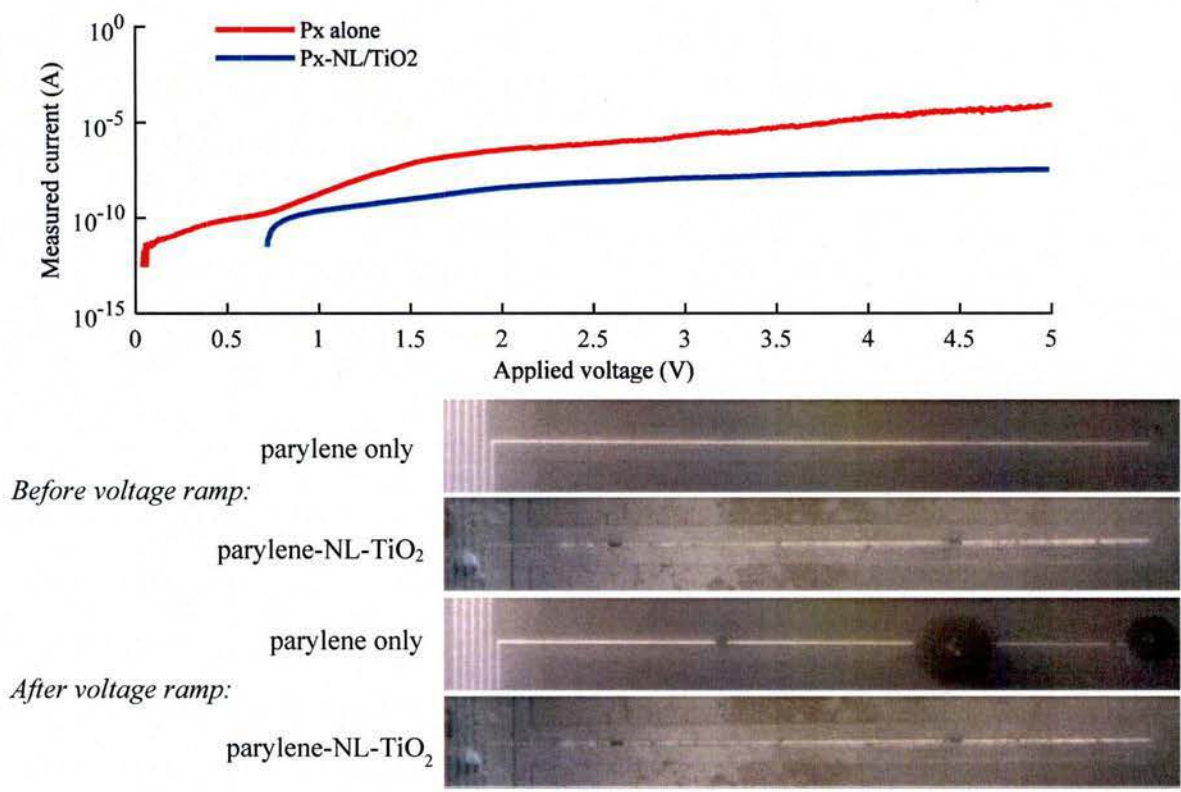


Figure 52. Ramp from 0 V to 5 V at a rate of 0.016 V/s applied between insulated wire and an on-chip Pt counter and. Top: Current measurement. Bottom: Test structures before and after voltage ramping.

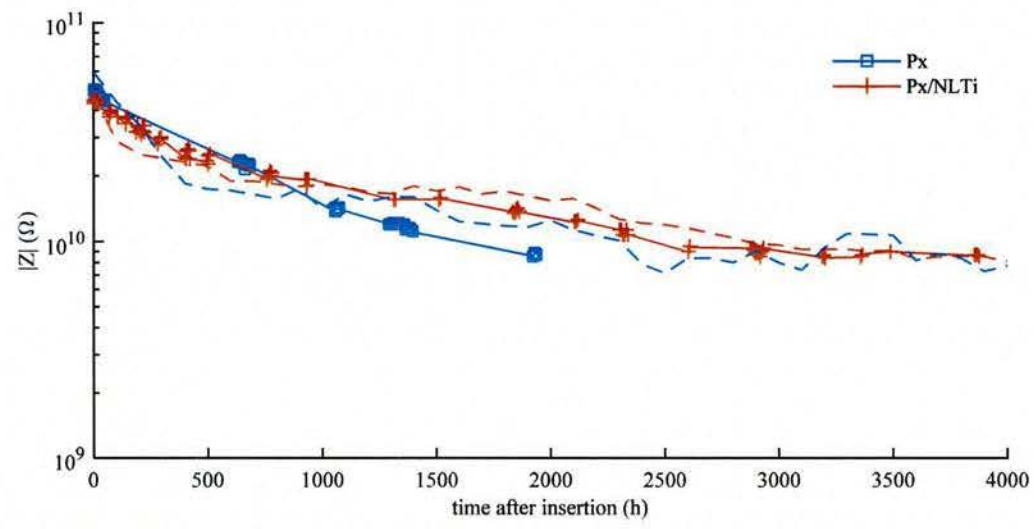


Figure 53. Impedance of test structures in 1x PBS under simulated stimulation voltage conditions at 0.1 Hz. Full lines: samples having 1 V peak-to-peak sinewave applied at 0.1 Hz continuously. Dashed lines: samples without the voltage applied, shown for comparison. All traces correspond to averages of all 16 channels over  $n=3$  samples ( $n=2$  samples for parylene under voltage stimulation).



### 7.4.8 Electrode impedance tests

Electrode impedance test structures as described in section 7.1.4 were tested in 1x PBS. For exposed electrodes, the impedance at 1 kHz scales with area. Figure 54 shows the impedance over time for  $20\ \mu\text{m} \times 20\ \mu\text{m}$  electrodes. The impedance values do not change significantly over time. Except for short excursions likely caused by experimental condition variations, the value stays within 5% of its starting point for over 800 h for the parylene sample and over 600 h for the parylene- $\text{Al}_2\text{O}_3$  sample. As discussed in section 7.4.5, the impedance of insulated test structures at 1 kHz remains high overall over the testing period; therefore, the insulation impedance does not contribute significantly to the impedance at 1 kHz when exposed electrodes are present.

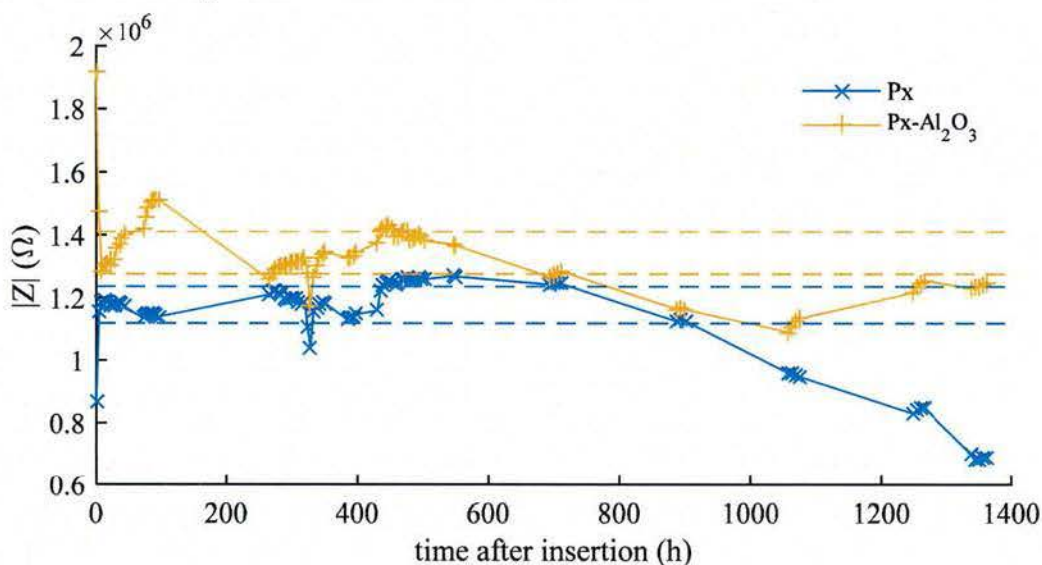


Figure 54. Impedance at 1 kHz in 1x PBS for  $20\ \mu\text{m} \times 20\ \mu\text{m}$  electrodes. Dashed lines correspond to  $\pm 5\%$  around the early impedance.

### 7.4.9 Iridium oxide stimulation electrode tests

Iridium oxide test structures described in section 7.2.4 were inserted in PBS and their impedance measured. Applying repeated cyclic voltammetry (CV) cycles between  $-0.6\ \text{V}$  and  $+0.8\ \text{V}$  (with respect to a  $\text{Ag}/\text{AgCl}$  reference electrode) activates the iridium oxide. Figure 55 shows how the impedance of electrodes of different size changes before and after 80 activation cycles. Figure 56 shows the evolution of the charge storage capacity (CSC) during the activation. The CSC increases dramatically for all electrodes, and the larger electrodes require more CV cycles to completely activate the iridium oxide.

The charge injection capacity (CIC) of these electrodes was determined by applying biphasic current pulses in 1x PBS and measuring the voltage amplitude. The maximum current that can be applied without generating voltages at the electrode exceeding the water window is used to determine the CIC. Pulses with  $200\ \mu\text{s}$  cathodic phase,  $200\ \mu\text{s}$  anodic phase and  $200\ \mu\text{s}$  interphase and a pulse repetition rate of 4 Hz yielded measured CIC that exceeds  $2\text{mC}/\text{cm}^2$  for small electrodes, and scales with area as expected from the literature.

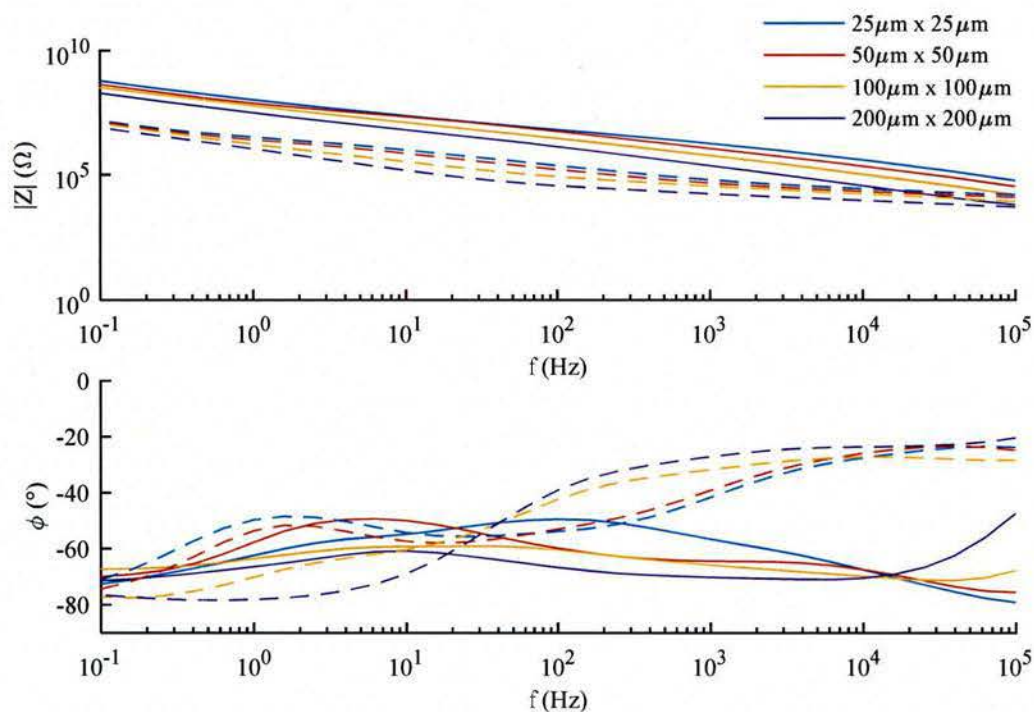


Figure 55. Bode plot of IrO<sub>2</sub> electrodes before activation (full lines) and after activation (dashed lines). Activation consisted of 80 CV cycles between -0.6V and 0.8 V.

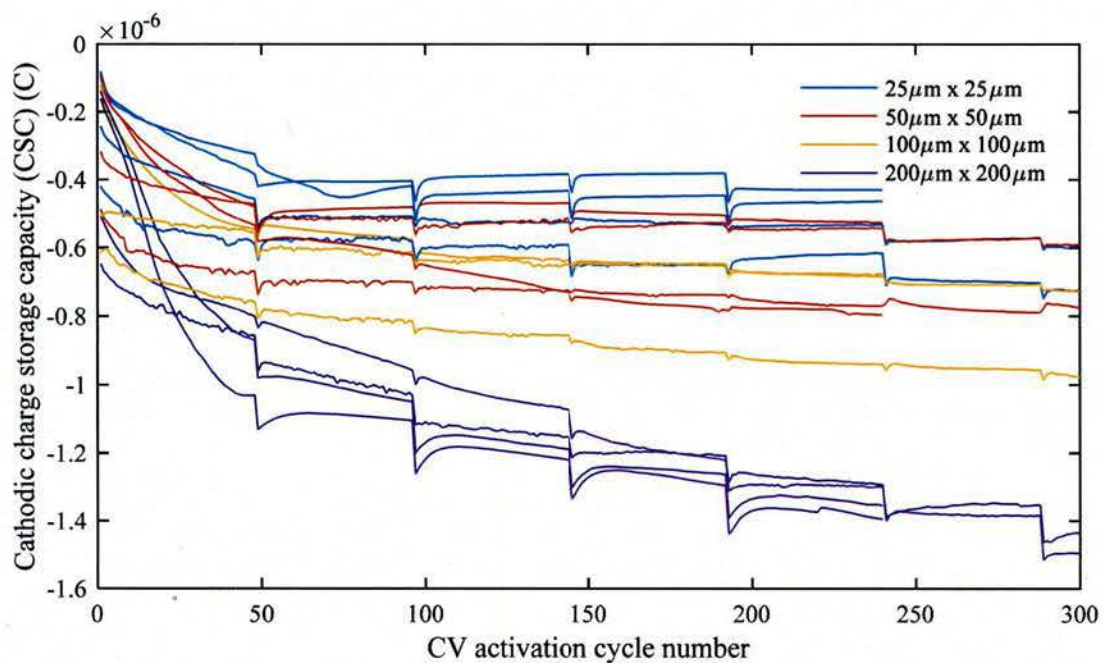


Figure 56. Evolution of the charge storage capacity of the IrO<sub>2</sub> electrodes during the CV activation. The periodic dips in the activation are artifacts of the CV measurement and do not indicate a change in the CSC. Measurements were performed on two samples.



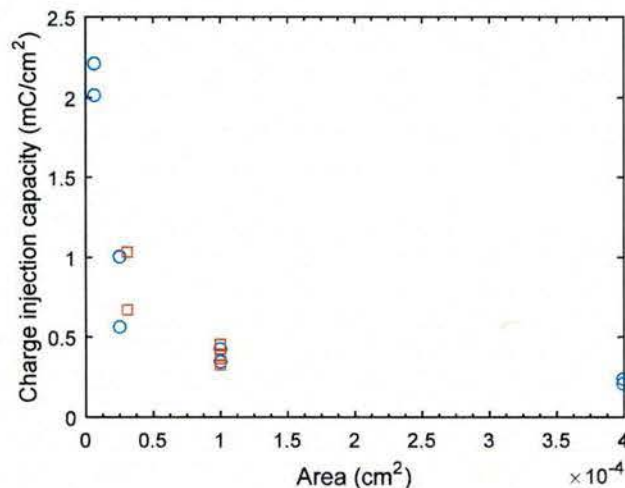


Figure 57. Charge injection capacity calculated from the voltage response to 200  $\mu$ s biphasic current pulses measured at 0 V bias in 1x PBS. Circles correspond to square electrodes and squares correspond to rectangular electrodes.

#### 7.4.10 Protruding electrode impedance tests

Test structures with protruding electrodes were fabricated with three different variants as shown in Figure 30. Initial testing was performed to assess the effect of the protrusion on the impedance. The Bode plot of the impedance of the electrodes after electrochemical cleaning (10 cyclic voltammetry cycles between -0.6 V and 0.8 V) is shown in Figure 58. The electrochemical cleaning replaces the typical  $\text{Ar}^+$  ion milling done at the end of the fabrication for other electrode samples. The protrusion reduces the impedance at 1 kHz by more than 4x for this sample, mainly because of the increased roughness of the underlying parylene.

Samples were left inserted in 1x PBS vials for over 50 days. During this time, voltage was applied to the electrodes (1 V peak-to-peak sinewave at 0.1 Hz) to mimic stimulation conditions. Occasionally the voltage stimulation was halted and the impedance was recorded. The impedance at 1 kHz over time is shown in Figure 59. While the impedance of electrodes without protrusion is larger than it is with protrusions over the same sample, the difference is not significant compared to the sample to sample variation of impedance. The impedance after electrochemical cleaning is more stable for samples with protrusion than the control samples (“no protrusion” variant), with exponential decay time constants between 3 and 10 times larger. It is likely that the initially lower impedance of the protruded samples explains this difference in impedance variation. No noticeable difference exists between the “with gap” and “no gap” variants.

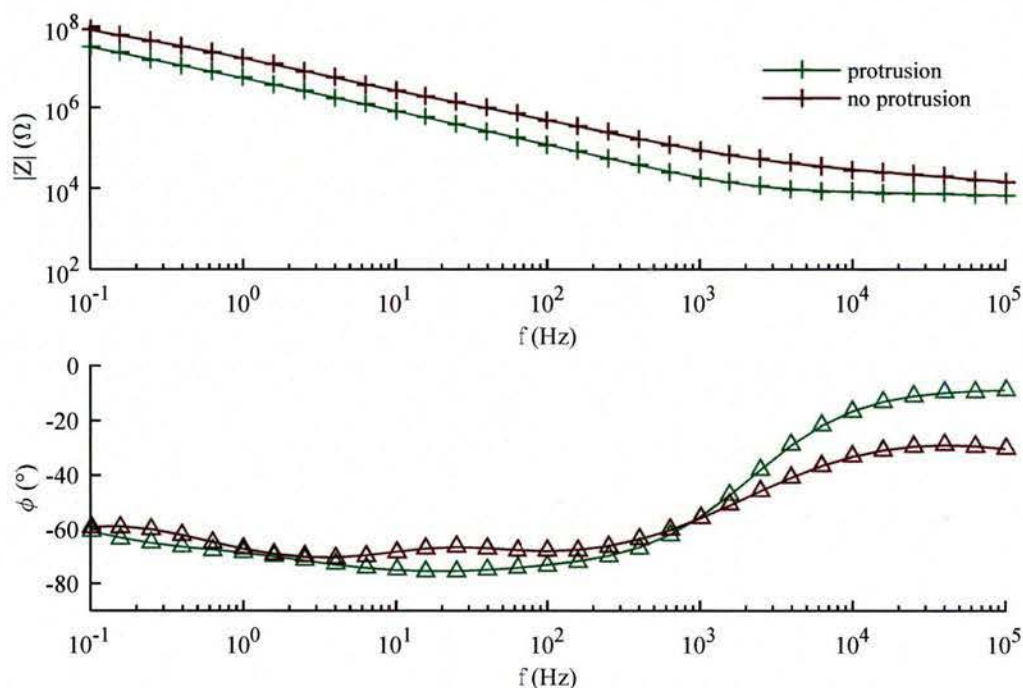


Figure 58. Bode plot of the typical impedance of test structures with  $115 \mu\text{m} \times 15 \mu\text{m}$  electrodes, with and without protrusions.

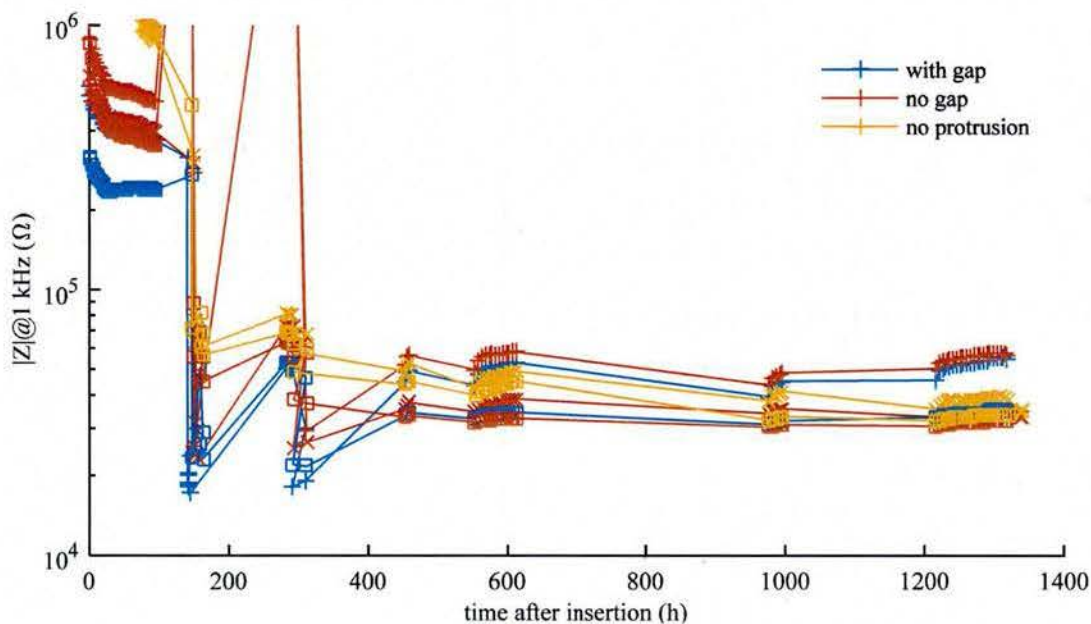


Figure 59. Impedance at 1 kHz in 1x PBS of protruding electrode test structures ( $n=2$  samples for “with gap” and “no protrusion” variants,  $n=3$  samples for “no gap” variant). Electrochemical cleaning is included in the first 300 h of measurement, so the impedance values do not accurately match the real impedance of the electrodes.



#### 7.4.11 *In vitro* probe insulation and impedance tests

Impedance test results of probes with molded needles, fabricated using the two of the bonding processes, then released and inserted in 1x PBS is presented in Figure 60. For all the samples tested, the impedance of the fully insulated self-test wire was found to be lower than that of the exposed electrode. Given that the self-test wire is located closer to the outer edge of the parylene probe than the electrode wiring, we hypothesize that leakage of the parylene insulation in the interconnect area explains the relative values of impedance observed. Therefore improved insulation of the parylene probes is required in order to achieve good recording or stimulation quality. This need for improved insulation is further motivating the parylene-NL-TiO<sub>2</sub> insulation.

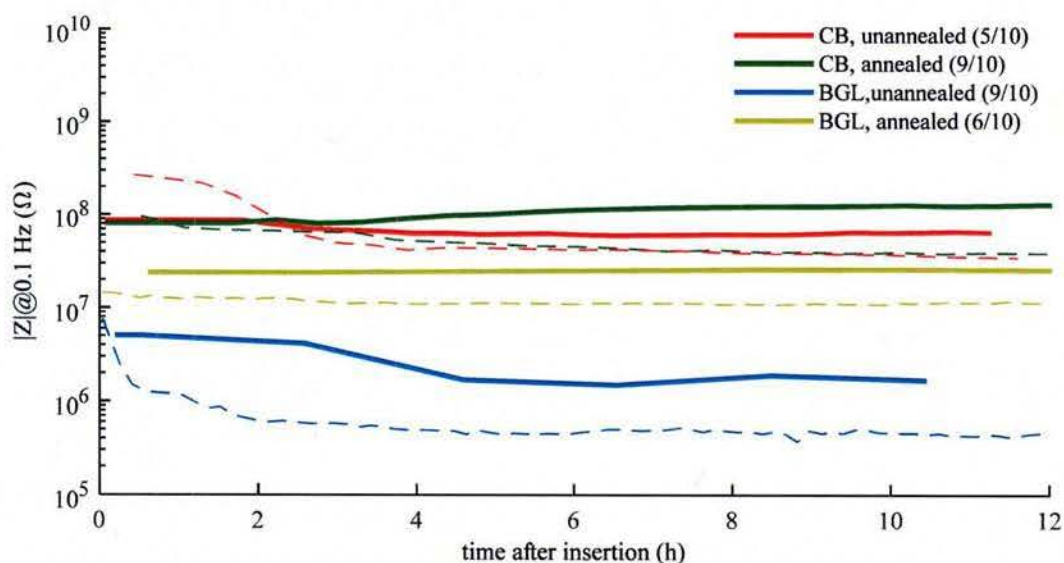


Figure 60. Average impedance of needles in 1x PBS using a platinum wire counter and Ag/AgCl reference electrode. CB indicates samples fabricated using Crystal Bond 509 adhesive; BGL indicates samples fabricated using BGL7080 adhesive; post-fabrication annealing step performed for samples as usual (3 h, 300 °C, 10 mT in N<sub>2</sub> environment). Full lines correspond to 115 μm × 15 μm electrodes; dashed lines corresponds to insulated self-test wiring. Numbers in the caption indicate the number of electrodes averaged for each sample.

*In vitro* impedance measurements were performed for parylene probes with different methods of assembly with the CMC/glucose needle:

- CMC/glucose needle molded on the probe (“molded CMC”) (*n*=1 sample)
- CMC/glucose needle molded separately and attached to the probe (“attached CMC”) (*n*=1 sample)
- No CMC/glucose needle (“no CMC”) (*n*=4 samples)

In order to improve the impedance, a low-stress needle attachment method was developed (see section 7.5.3.2), corresponding to the middle case, “attached CMC”.

The initial impedance magnitudes are shown in Figure 61. In addition to the impedance of the electrodes, a self-test loop without exposed metal is measured; its impedance is indicative of the quality of the insulation. The molded CMC probe has the lowest impedance at low frequency of all three methods, and the impedance of its self-test loop is lower than the electrode impedance. The leakage across the

insulation dominates the impedance instead of the electrochemical impedance across the exposed electrode. Cracks in the parylene layer caused by stresses during CMC molding explain the insulation failure. The attached CMC and no CMC samples have similar impedance for the electrode, indicating that the direct CMC needle attachment method does not cause damage to the insulation. The self-test loop impedance is higher for the attached CMC sample than for the no CMC samples; however, there is significant variation across the different samples tested for the no CMC case. For all methods, some electrodes achieved less than 5% variation in impedance at 1 kHz over the measurement period (12-20 h), after the first few minutes corresponding to dissolution of the CMC.

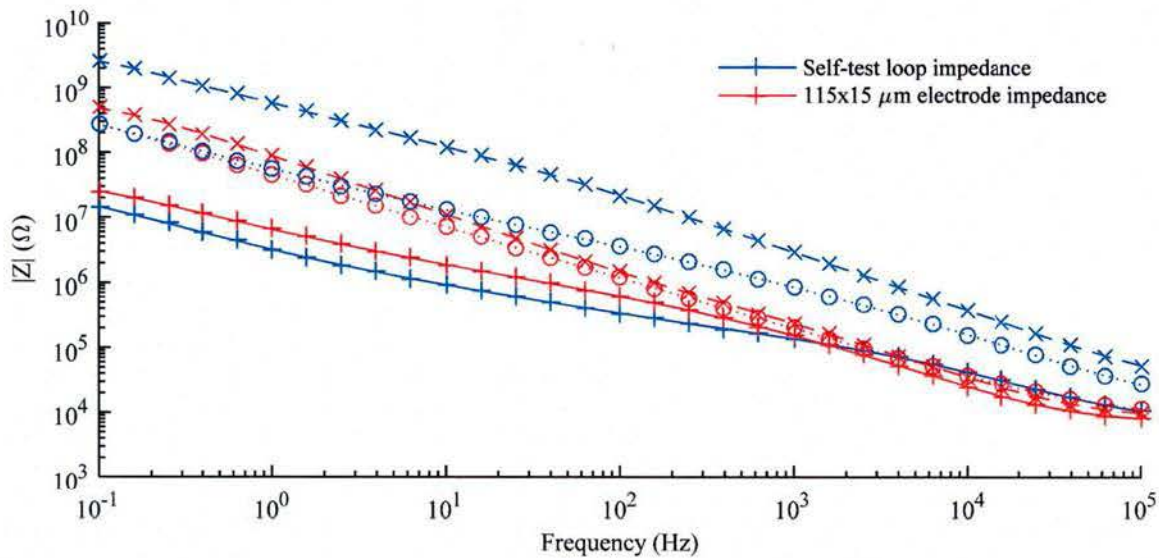


Figure 61. *In vitro* impedance of recording probe in three different assembly configurations: 1) molded CMC needle (full line), 2) low stress bonded attached CMC needle (dashed line), and 3) no CMC needle (dotted lines). The self-test loop does not have exposed metal and its impedance is indicative of insulation quality.

A 9  $\mu\text{m}$  thick parylene probe was bonded to a CMC needle and inserted in PBS. The impedance was measured for over 16 h, with results in Figure 62. The electrode impedance at 1 kHz was between 250 k $\Omega$  to 350 k $\Omega$ . The high value and variability might indicate the presence of residue on the electrode. The impedance at 1 kHz of the insulated loop was over 10x larger in value. The insulation impedance at 0.1 Hz dropped from 45 G $\Omega$  to around 15 G $\Omega$  in 2 h, after which the impedance decreased at a slower rate. Nonetheless, the insulation impedance decrease is orders of magnitude faster than measured for the test structures. The narrower insulation of the probe, or the additional stress caused by the motion of the released probe might explain the faster decay. We hypothesize that the addition of the nanolaminate insulation might also prevent some of this fast degradation.



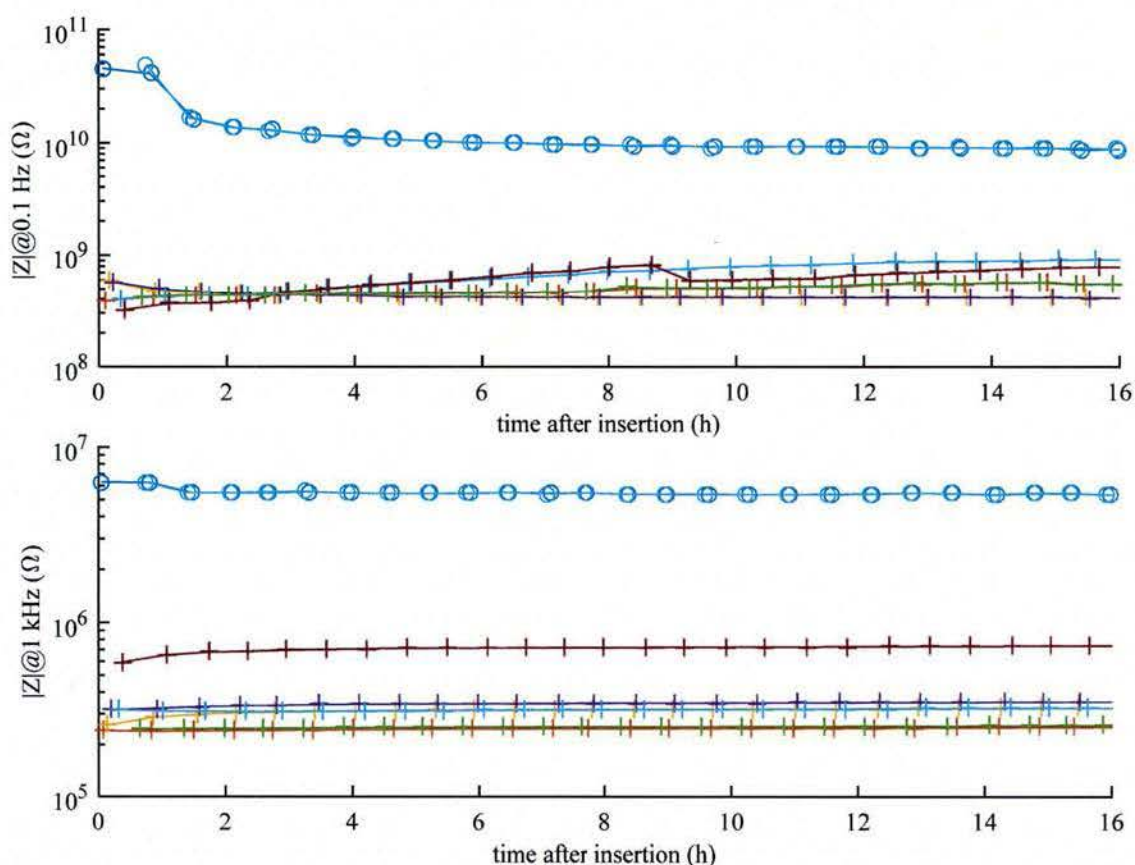


Figure 62. Impedance at 0.1 Hz (top) and 1 kHz (bottom) of a 9  $\mu\text{m}$ -thick parylene probe bonded to a CMC/glucose needle and inserted in PBS. The circle markers correspond to an encapsulated wire loop at the edge of the probe. All the cross markers correspond to  $115 \mu\text{m} \times 15 \mu\text{m}$  electrodes on the probe. Some high impedance electrodes corresponding to broken wires were removed from the plot.

## 7.5 Bio-dissolvable needles

### 7.5.1 Needle material mechanical properties

At ambient room temperature, carboxymethylcellulose (CMC) retains more water at room temperature than at higher temperatures. Thereby, the mechanical strength of CMC varies with its concentration (*i.e.*, with the amount of water retention). Since the probes will be sterilized by heating before insertion into animals, knowing the concentration of CMC as a function of time after heating is important in assessing probe strength that is obtainable during practical insertion into animals. Figure 63 shows the concentration of CMC with time after sterilization at  $110^\circ\text{C}$ .

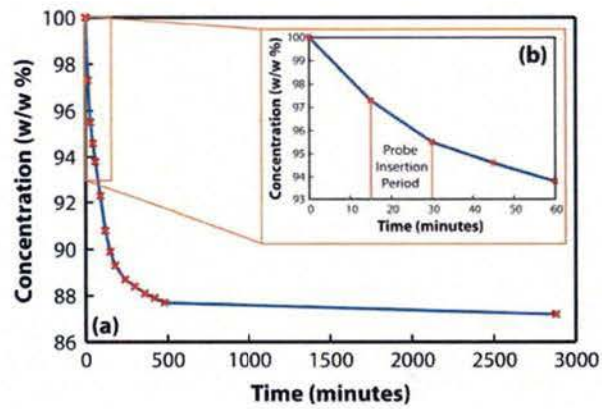


Figure 63. Concentration of CMC after sterilization. (a) Long term.  
(b) Inset showing concentration during needle insertion.

The experimental setup shown in Figure 64 generates the stress-strain relationship for material samples to obtain the mechanical properties of dissolvable polymers. CMC are 2 cm square sheets micromachined into a dog-bone structure using a miniature machine tool. The dog bone is mounted onto an Instron test machine using a custom made fixture to carry out tensile tests.

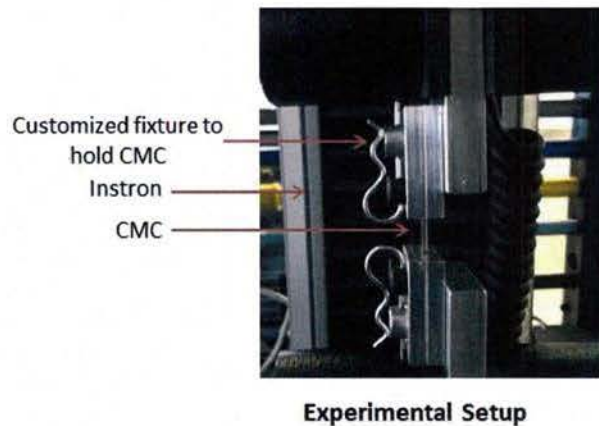


Figure 64. Mechanical stress-strain characterization testbed mounted on an Instron tensile test machine.

Figure 65 shows the mechanical properties of CMC at three concentration levels. The concentration of the probe deemed best for insertion into agar and tissue is 96.5%, i.e., 15 to 30 minutes post sterilization according to Figure 63. The Young's modulus of the CMC material is higher at higher concentration; however, the material at higher concentration becomes more brittle and has lower strain at failure. At lower concentration the material is more ductile and has lower modulus.



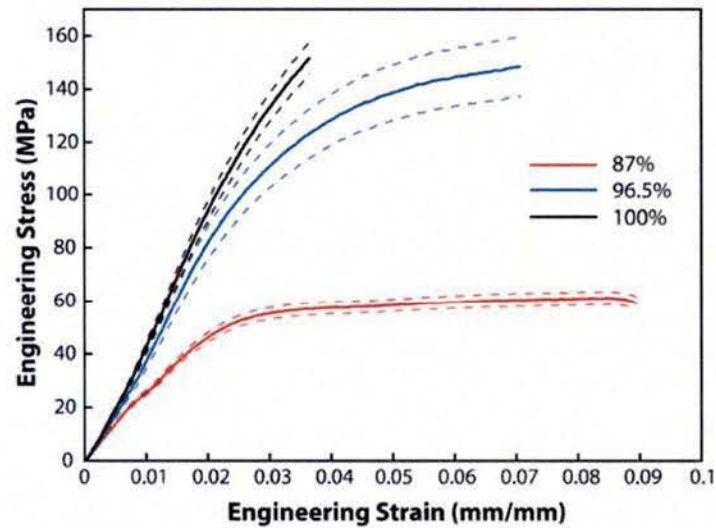


Figure 65. Stress-strain characteristics of CMC at different concentrations.

Figure 66 shows the mechanical properties of all CMC/sugar materials tested at 96.5% concentration. The CMC/sucrose combination makes the polymer matrix brittle and about 60% lower strain at failure than other combinations, which have sufficient toughness. The similarity in mechanical properties of CMC, CMC/glucose and CMC/maltodextrin allows us to choose the material for other properties (*e.g.*, better molding and faster dissolution) while not compromising the toughness of the needle.

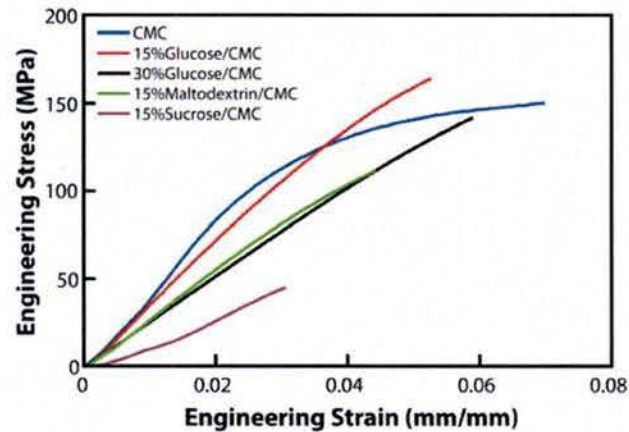


Figure 66. Mechanical properties of CMC and CMC/sugar alloys.

## 7.5.2 Needle-probe molding process

### 7.5.2.1 2D direct molding process onto probes

The schematic diagram in Figure 67 illustrates the steps involved in the spin-cast micromolding process. A resin mold placed onto the top of the transferred probe chip defines the shape of probe needle and the tab holder by acting as a reservoir in the molding process (The probe transfer method is explained in section 7.2.6). The probe needle design in Figure 68 is an inverse (negative) image of the mold opening. The resin mold has through openings having same general shape as that of the probe, but with larger features

to encompass the probe. A 15% (w/w) glucose/ 85% CMC hydrogel is dispensed on top of the transferred probe chip, then assembled and centrifuged at 10°C and 2000 rpm. The centrifugal force ensures flow of the hydrogel into the resin reservoir. Water in the hydrogel gets removed toward the open surface until it reaches a concentration of 87%, which is the equilibrium concentration at room temperature. The excess material is removed from the top surface. The parylene-Pt structures are at this point embedded within the CMC/glucose matrix. The sacrificial substrate layer is dissolved to release the probe assembly (see section 7.2.6). Liquid wax (BGL7080) is soluble in IPA and chosen to be the adhesive sacrificial layer. The CMC/glucose material is not affected by acetone or IPA.

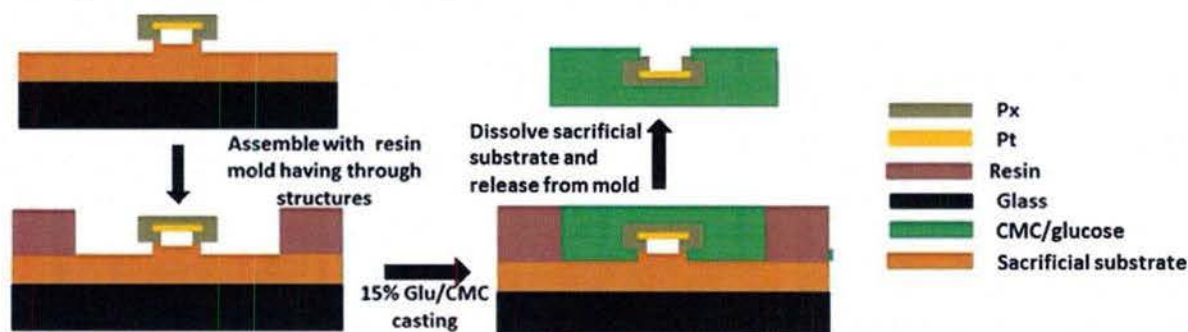


Figure 67. Schematic of the molding process.

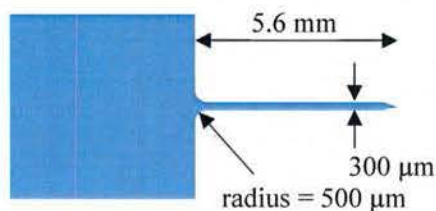


Figure 68. Needle design with handling tab, used in initial molding experiments.

The CMC/glucose : water concentration gradient that develops during the drying process, which occurs only from one side of the needle (*i.e.*, the top side is exposed to air). This gradient causes residual stress in the CMC/glucose matrix during the spin-casting process. Release of the needle-probe assembly allows the residual stress to act on the probe, causing strain in the parylene that lead to strain (crack) marks (Figure 69). Additionally, shrinkage of CMC/glucose causes excessive strain at the interface where the probe cable exits the handling tab. Usually these cracks do not extend to Pt wires, which means that the self-test loops – used a metric for successful probe-needle molding – are not broken. However, electrical impedance tests on these molded probes result in lower impedance values compared to test structures. These micro-cracks are a cause for insulation failure after molding of the needle onto the probe. The needle assembly process, discussed next, alleviates these issues and supersedes the direct molding process.

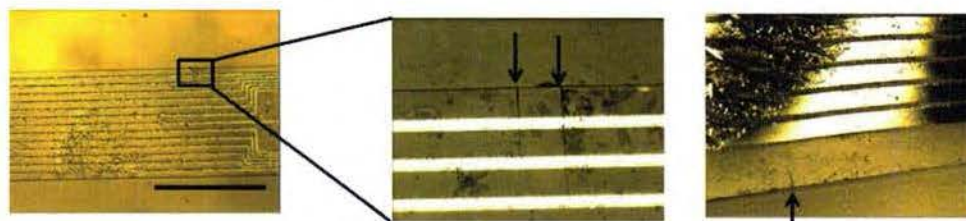


Figure 69. Strain marks (micro-cracks) in parylene insulation that occur from CMC residual stress.



### 7.5.2.2 Needle molding in a PDMS mold (with suture hole)

A PDMS mold of the needle enables the successful needle-probe direct assembly process in section 7.5.3. The PDMS molding allows creation of regular needles and needles with through holes. The cross-section schematic describing the molding process is shown in Figure 70, depicting a CMC/glucose needle design with a through-hole that is between 100  $\mu\text{m}$  to 125  $\mu\text{m}$  in diameter. The PDMS mold is the negative image of the needle shape. The through-hole enables the technique of pulling the probe through nerve tissue using a suture (as an alternative to insertion by pushing into the tissue). The assembly approach using direct bonding is shown in Figure 71. Section 7.5.3.2 presents this direct assembly approach in greater detail.

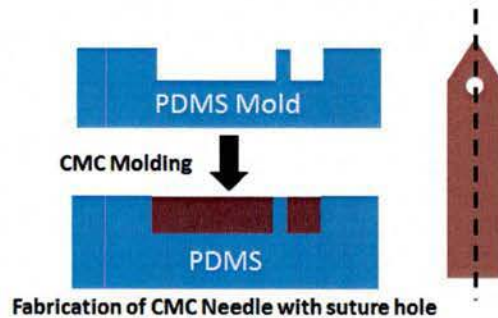


Figure 70. CMC needle molding with a suture hole.

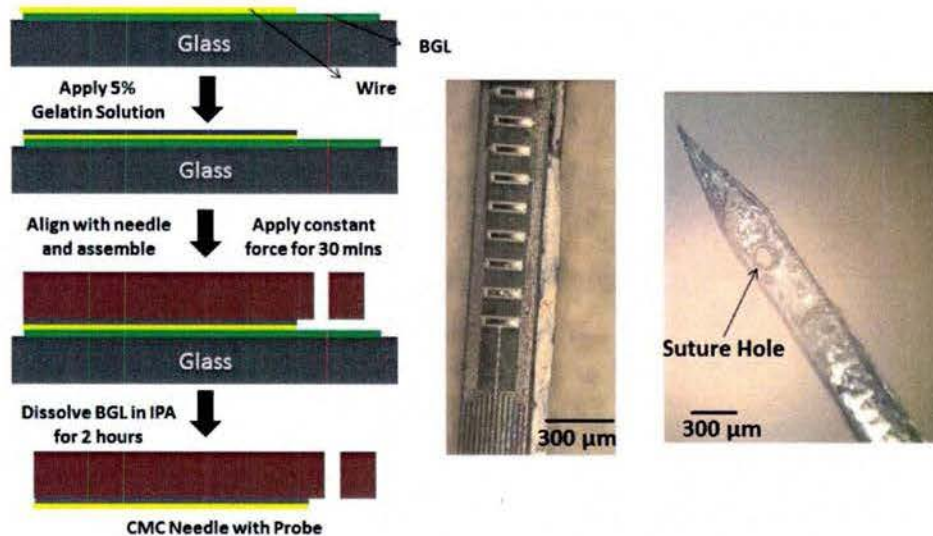


Figure 71. Assembly of CMC needle with the suture hole onto a parylene-Pt probe.

### 7.5.2.3 Multi-shank needle array

CMC/glucose multi-shank needle arrays must mate with corresponding multi-probe arrays. Figure 72 shows the design of a fabricated dual shank needle. A PMMA master mold was machined using a 1 mm tool on a micro-machining center and a PDMS production mold was fabricated. The dual shank needle molding uses a similar process to that of a single shank needle, with CMC loading steps customized for the design. Four-shank arrays are also designed and fabricated.

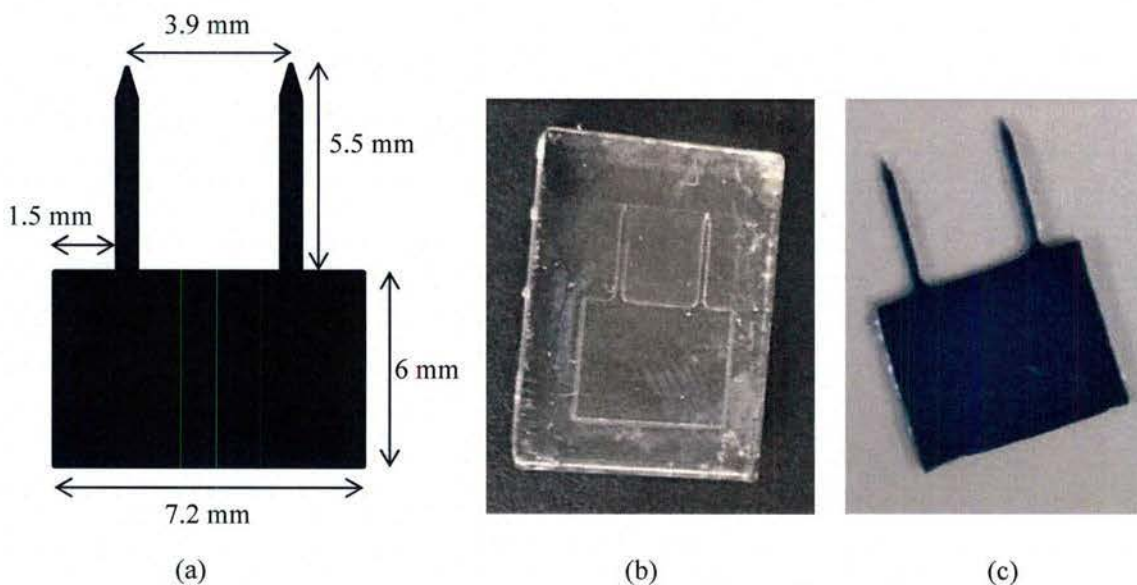


Figure 72. (a) Design of the dual shank mold, (b) PMMA master mold, (c) CMC/glucose needle array.

### 7.5.2.4 Sharp 3D tip needles (symmetric)

A symmetric sharp tip reduces any non-axial force upon insertion, which could contribute to failure of the needle due to bending and cause it deviate off the intended targeted location. The direct assembly process makes such a design practical, as it would be impossible to mold in the vertical configuration in a direct molding process with the probe. Such 3D sharp symmetric tips also reduce dimpling and reduce penetration force during insertion.

Symmetric 3D sharp needles require a more sophisticated PDMS mold. The 3D tipped needle can be bonded to the probes using the method in section 7.5.3.2. Figure 73 shows the schematic diagram of fabricating such needles and Figure 74 shows two example needles. Needle molding occurs in a vertical configuration in the centrifuge as compared to the horizontal configuration for needles with 2D wedge tips. Separating the needle molding and the probe fabrication through the direct assembly process, discussed in the next section, enables greater flexibility in design of both needles and probes and increases the design space allowing for better needle designs that could not be fabricated if they had to be micromolded along with the probe.



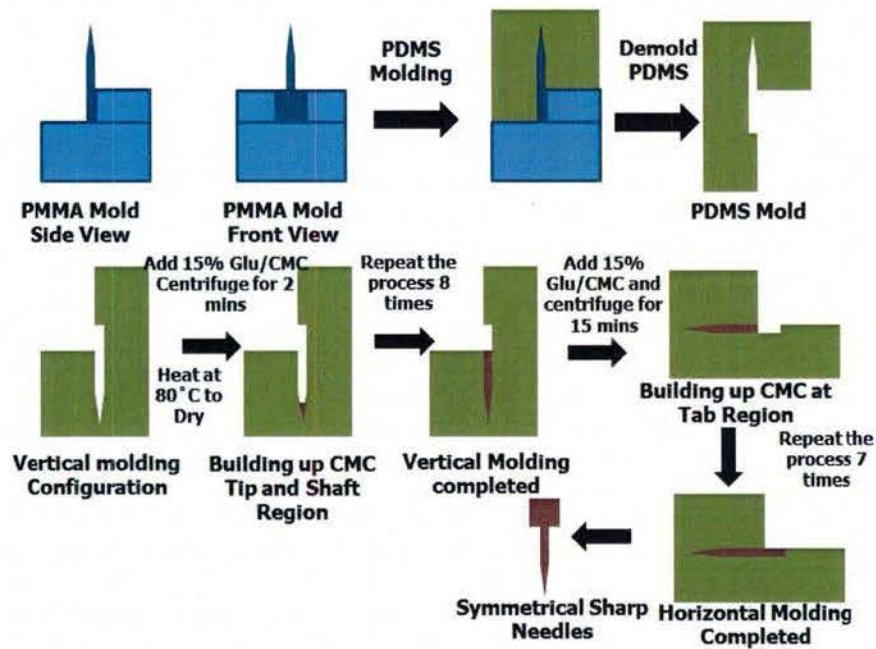


Figure 73. Master mold and fabrication steps for CMC/glucose needles with symmetric sharp 3D tips using a combination of vertical and horizontal molding.

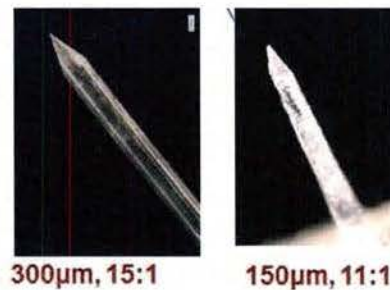


Figure 74. 85% CMC/15% glucose needles with symmetric 3D sharp tips having widths and aspect ratios as noted.

### 7.5.3 Needle-probe assembly

A direct needle-probe assembly method addresses the issue of excessive stress caused by drying of the CMC/glucose needle. Needles are molded separately and then bonded to the parylene-Pt probe to ensure that release of residual stress and shrinkage of the needle and tab do not affect the probe insulation or wiring integrity. Additionally, needle-probe bonding expands the needle design space and enables use of needles with sharp 3D pointed tips instead of less sharp 2D wedge tips. The technique also enables design of needles with special features such as creating a hole in the needle enabling a suture to pull the needle through tissue.

Bonding of the needle to the probe substrate employs a Besi M9A device bonder (BE Semiconductor Industries N.V., Duiven, The Netherlands) to provide repeatability and to reduce manual intervention. Two assembly methods, described in the following subsections, were tested.

### 7.5.3.1 Method of wetting needle surface with dip-in adhesive

In this method, depicted in Figure 75, the CMC/glucose needle is dipped into a liquid adhesive, and then subsequently bonded to the probe substrate. The conventional Besi M9A vacuum port does hold the needle; the needle sticks to the adhesive and force from the vacuum port is not sufficient to pull the needle away from the adhesive layer. Hence, a vacuum channel manifold was made to increase the vacuum surface area and hence increase the force holding the needle.

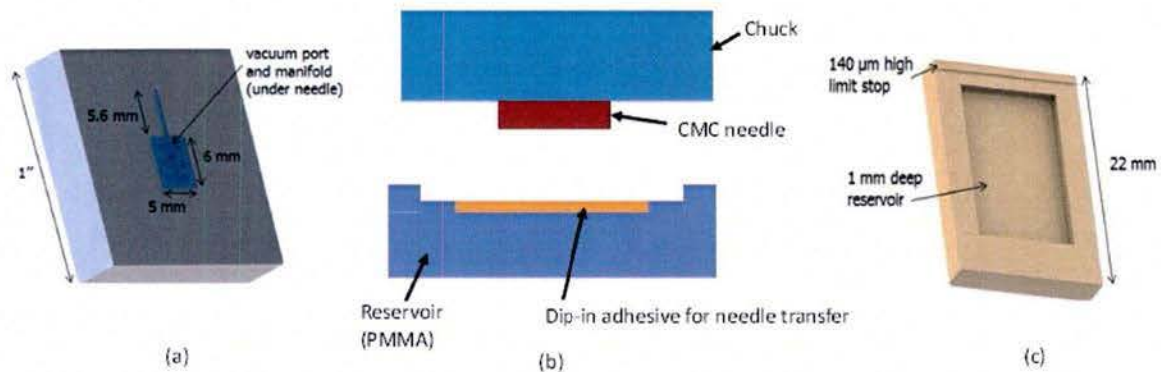


Figure 75. Method to wet needle with adhesive for subsequent bonding. (a) Solid model of the custom vacuum chuck holding needle. (b) Side view schematic of CMC needle over dip-in reservoir. (c) Solid model of the reservoir.

The following experiments were conducted to explore options to transfer adhesive to CMC in a repeatable manner:

1. Water as adhesive: When water is absorbed by CMC, it forms an adhesive gel. However, water doesn't wet shallow wells for both acrylic and brass wells (200  $\mu\text{m}$  deep). When deeper wells as shown in Figure 75(c) are used, excessive water wicks to around the surface of the CMC needle making it an unrepeatable process.
2. Gelatin as adhesive: Low concentration gelatin (5%) creates similar problems as seen with water. Higher concentration (15% or 20%) gelatin gel is first heated to 50°C and then spin cast to fill the reservoirs. However, when the needle comes in contact with the gelatin gel, the probe sticks to gel and gets dislodged from the vacuum chuck. As an alternative to vacuum, BGL7080 liquid wax to stick the CMC needle to the chuck was attempted, ensuring that the needle adheres well to the chuck. However, the gelatin behaves like a strong rubber gel that doesn't separate easily, leading to large quantities of gel being transferred to CMC probe. In some cases, the entire gelatin mass from the reservoir is stuck to the probe.
3. CMC/glucose hydrogel as adhesive: Low concentration CMC/Glucose (up to 10%) does not wet the CMC and has similar problems as water and low concentration gelatin. However, a 15% gel can be cast in a centrifuge within shallow wells from 60  $\mu\text{m}$  to 200  $\mu\text{m}$ . The reservoir part is designed with a limit stop to limit the depth that the needle inserts into the well. A 200  $\mu\text{m}$  well is used with a 140  $\mu\text{m}$  stopper to ensure only the first 60  $\mu\text{m}$  in thickness of CMC comes in contact with the gel. However, the transfer of hydrogel to CMC is not repeatable and the hydrogel coalesces rather than distributing uniformly. Other experiments included well designs with removal of the limit stop combined with 30  $\mu\text{m}$ , 60  $\mu\text{m}$  and 100  $\mu\text{m}$ -deep reservoirs. The wells were filled in a centrifuge. The 30  $\mu\text{m}$  wells had too little CMC and dried out very quickly. The



remaining two wells did enable successful transfer of gel to the needle, but there was considerable CMC on the side of needle rather than just at the bottom of needle.

4. Other screening experiments included using a soaked filter paper to transfer adhesive to the CMC needle, however the filter paper sticks to the CMC strongly and cannot be separated.

These experiments using the method of dipping the CMC needle into a well with water or hydrogel is not repeatable and the amount of adhesive transferred cannot be controlled.

#### 7.5.3.2 Method of casting adhesive on a PDMS needle mold/transfer holder

The second needle-probe assembly method employs the process flow depicted in Figure 76. A PDMS transfer holder holds the CMC/glucose needle during spin casting of gelatin adhesive. The PDMS holder is the same mold that is used to cast the CMC/glucose to fabricate the needle.

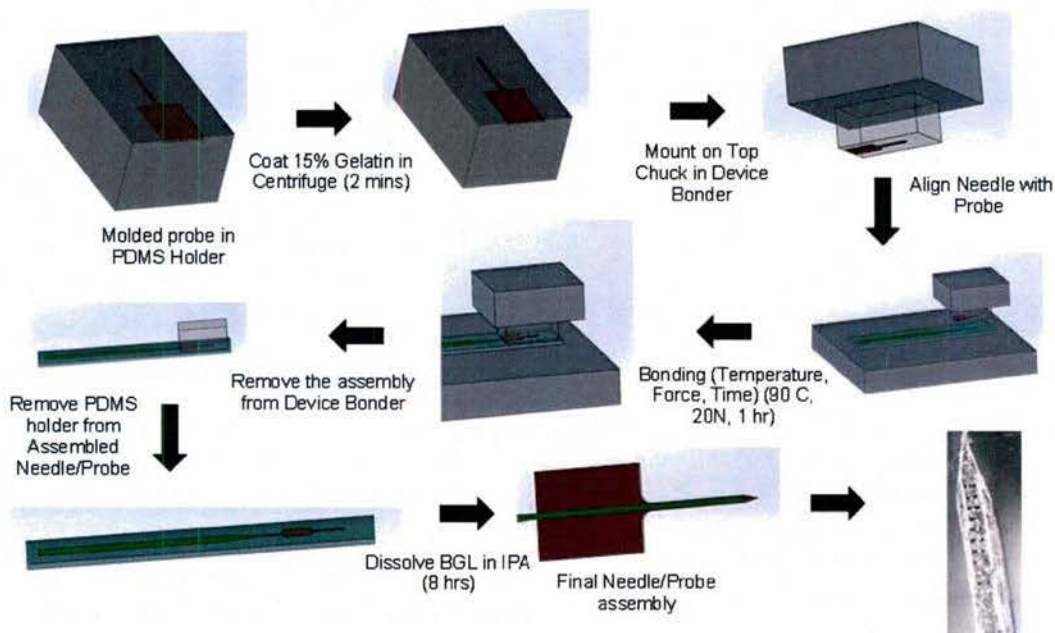


Figure 76. Needle-probe bonding method using a PDMS needle holder and 15% gelatin as adhesive layer

A thin layer of 15% gelatin liquid is cast in the centrifuge for 2 min over the needle. The cast film is heated to 50°C to create the 15% gelatin liquid. The PDMS holder with the coated CMC/glucose needle is mounted on the vacuum chuck in the device bonder, aligned with the probe using the camera alignment system, and then bonded together. The conditions that can be varied in the device bonder are temperature, pressure, and time. Due to limitation in the availability of test structures, we kept the pressure and time in the device bonder fixed and conducted bonding experiments at temperatures of 60°C, 90°C and 120°C. At 120°C, a large number of bubbles form in the CMC/glucose that could be due to water molecules evaporating as seen in Figure 77(a). At 90°C, the probe-CMC assembly is successful and repeatable in the needle regions in all five of the trials. However, the bonding process is not repeatable in the handling tab region where the width of the probe cable is larger, failing in the handling tab region for two out of the five trials. Delamination of the tab from the probe is evident as shown in Figure 77(b). At 60°C, the probe fails to bond CMC/glucose in most cases in both the handling tab and needle regions. The delamination occurs

after release in IPA as confirmed by observing the tracks left behind by the probe in the CMC/glucose after it delaminates, as shown in Figure 77(c).

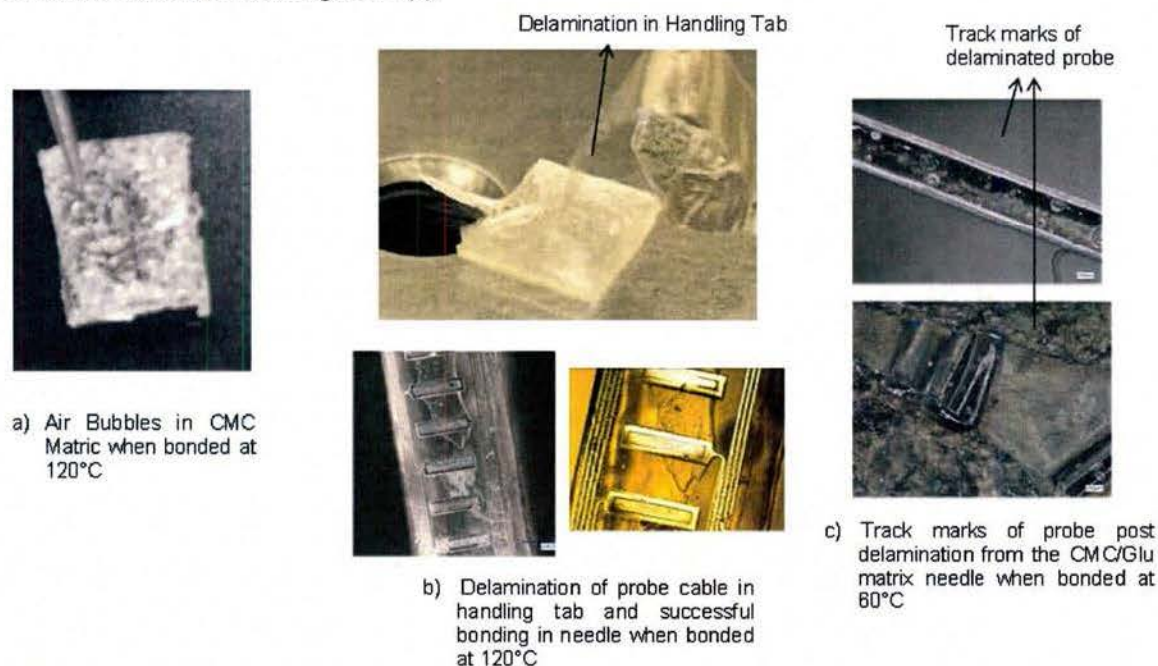


Figure 77. Needle-probe bonding method using a PDMS needle holder at different bonding temperatures

A design of experiment was carried out to study the bonding of 85% CMC : 15% glucose needles to parylene probe test structures at different values of bonding temperature and force. Parylene-only test structures were specifically made for these feasibility studies by depositing and patterning parylene directly onto BGL7080 wax coated glass slides. The casting adhesive is 15% gelation hydrogel. Bonding effectiveness increases at higher temperature (*i.e.*, 80°C) as compared to lower temperature. The bonding force level, varied from 0.5 kg to 2 kg, has no significant impact on bonding. Wrinkles and partial delamination occur at most conditions, as indicated in the SEM images in Figure 78. The qualitative results for bonding at different temperature conditions are summarized in Table 7.

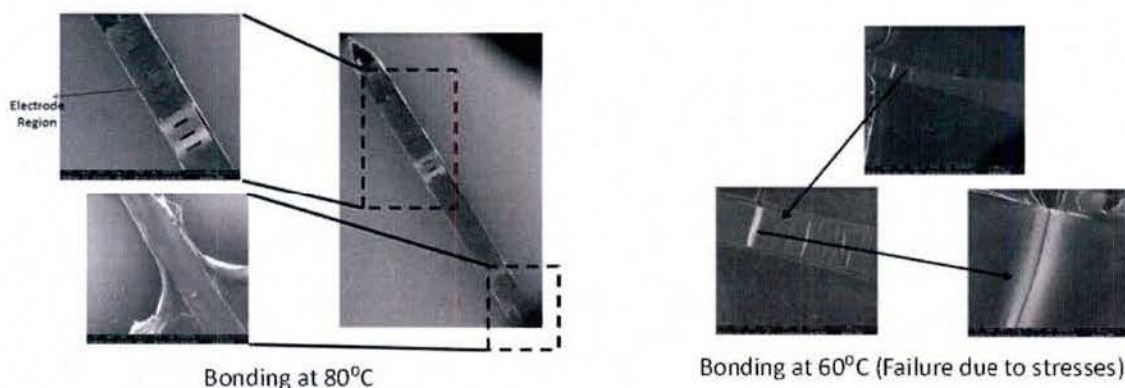


Figure 78. Needle/probe assembly results at 60°C and 80°C. Wrinkles are observed at both temperature values; however significant delamination is observed at 60°C.



Table 7. Bonding results at different temperatures.

Temperature	Number of Experiments	Bonding Results		Wrinkles/Low Radius Curvature
		Needle	Tab	
85°C	1	success	success	yes
80°C	3	success	success	yes
75°C	1	success	success	yes
70°C	1	success	success	yes
60°C	2	fail	fail	---

### 7.5.3.3 Gelatin probe-needle interlocking method

CMC-glucose and gelatin does not adhere well to parylene-C via the assembly process in the last section, as is evident based on the partial probe delamination from the needle leading to wrinkling. A method to interlock gelatin layers between the probe and needle is hypothesized to assist in successful bonding without delamination. A thin-film coating of gelatin is coated on top of parylene probes on a Si handle substrate. The probe structures are then transferred to a BGL-coated glass slide resulting in a gelatin layer underneath the parylene probe as shown in Figure 79(a). This gelatin layer is approximately 200 nm thick and designed to fuse with the gelatin layer on the needle surface during the bonding process to create a mechanical interlock. However, even in this scenario parylene structures delaminated from the needle leaving the imprint trace behind as shown in Figure 79(b). The non-uniform and very thin coating of gelatin is insufficient to create a mechanical interlock.

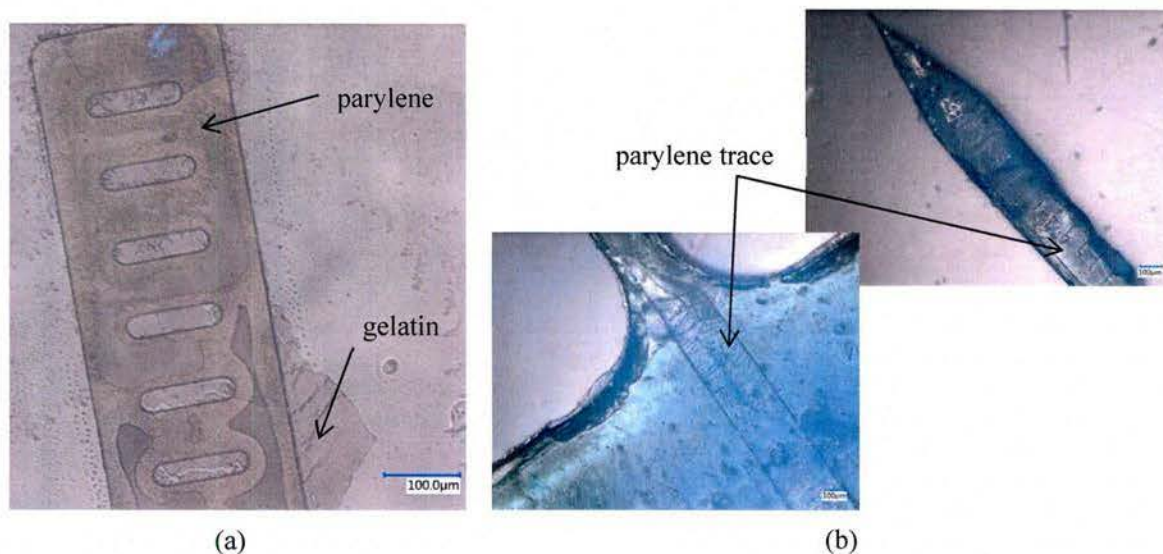


Figure 79. (a) Parylene structure on a BGL 7080-coated glass slide, with a thin-film of gelatin coating underneath the parylene for mechanical interlocking. (b) Results after probe-needle assembly.

#### 7.5.3.4 Adhesion improvement using O<sub>2</sub> plasma

To overcome the adhesion challenge between the CMC/glucose needle and parylene probe as discussed in the previous sections, O<sub>2</sub> plasma modifies the parylene-C surface making it more hydrophilic. Droplet tests performed with DI water confirm hydrophilicity is maintained for sufficient time to perform the binding process (Figure 80). Hydrophilic parylene-C adheres well to gelatin in the needle bonding process, and is the adhesion solution that enables successful needle-probe assemblies.

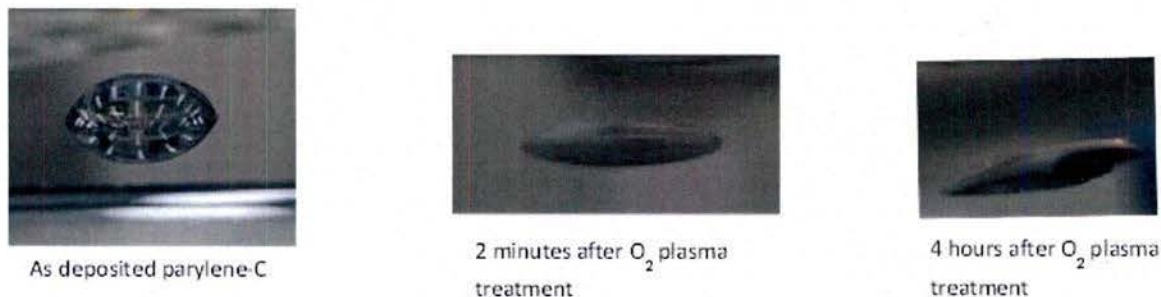


Figure 80. DI water droplets on parylene-C to illustrate hydrophobicity as deposited and hydrophilicity after exposure to O<sub>2</sub> plasma.

For test trials, “dummy” parylene-only probes test the effectiveness of O<sub>2</sub> plasma on needle probe adhesion. This O<sub>2</sub> plasma treatment increases the adhesion between the CMC/glucose needle and the parylene-Pt probe. The surface of the needle was wet with a 10% gelatin coating. 20 N force (~500 MPa) was applied for 45 min at 80° C to complete the bonding process. The BGL7080 liquid wax sacrificial transfer layer was dissolved in IPA (8 h) to release the probe-needle assembly from the substrate. The needle adheres to BGL7080 during the bonding process. The increase in release time over a probe alone is attributed to the longer lateral distance for IPA to dissolve the BGL underneath the needle.

Functional probes with two 4.5  $\mu\text{m}$ -thick parylene layers (9  $\mu\text{m}$  total probe thickness) help suppress the wrinkles observed in thinner 2.2  $\mu\text{m}$ -thick probes (4.4  $\mu\text{m}$  total probe thickness, as in Figure 78). Adhesion results of needles onto the 9  $\mu\text{m}$ -thick parylene-Pt probes (Figure 81) show the fidelity of the assembly at different regions in the needle and handling tab regions.

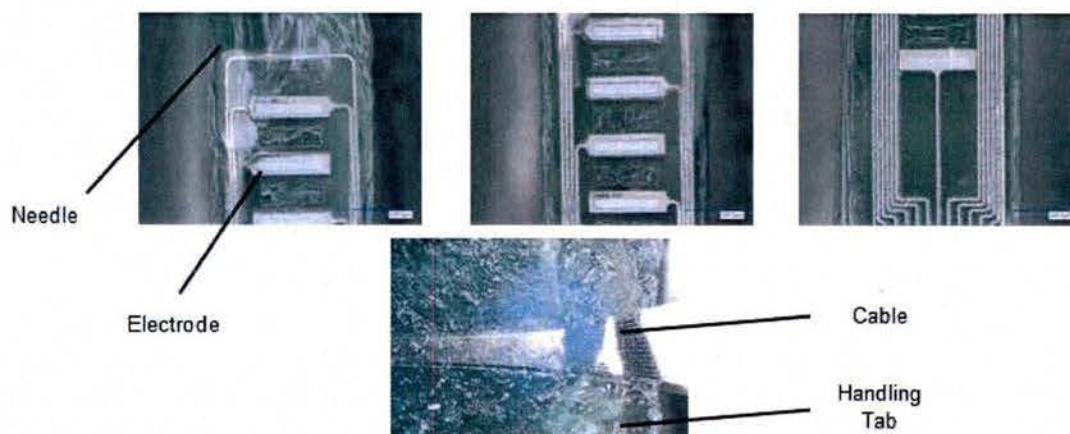


Figure 81. 85% CMC/15% glucose needle/probe assemblies. Probes comprise two 4.5  $\mu\text{m}$ -thick parylene layers surrounding the platinum wiring (9  $\mu\text{m}$  total thickness). Blue dye is added to the CMC/glucose matrix to enhance contrast.



### 7.5.3.5 Complete probe-needle assembly with handle/platform

One of the prominent failures on the needle-probe assemblies is the physical damage caused to the cables during manipulation and handling. Manual handling is exacerbated by the cable curling post release (Figure 82(left)), making it difficult to perform coverlay bonding and assembly with the ZIF-clip connector. The curling arises from residual stress gradients in the parylene-Pt layers. Curling is mitigated with the thicker (9  $\mu\text{m}$  thick) parylene-Pt probes, as shown in Figure 82(center). A rigid frame for probe handling along with a mating platform for mounting purposes is introduced in order to minimize handling issues after needle-probe release from the transfer substrate (Figure 82(right)). The frame is attached to the CMC/glucose handling tab and coverlay before it is released from the BGL7080-coated substrate. Upon release of the assembly, the frame serves as a handle and helps eliminate damage from manual handling of the cable and CMC tab.

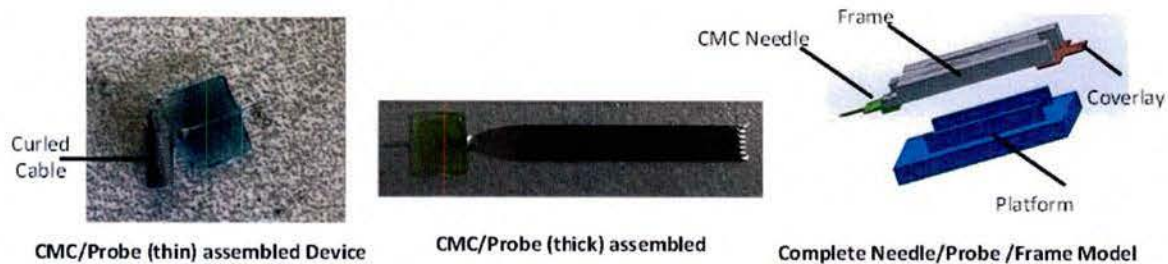


Figure 82. Cable handling issues. Left: Curling of a 4.5  $\mu\text{m}$ -thick parylene-Pt probe due to the residual stress gradient. Center: Relatively flat probe cabling in a 9  $\mu\text{m}$ -thick parylene-Pt probe. Right: The rigid frame and mounting platform alleviate manual handling issues.

## 7.5.4 Insertion into agarose phantom

### 7.5.4.1 Force measurement setup

Measurement of insertion force levels present in the brain is challenging, as conventional load cells do not have the necessary response time and sensitivity to measure these levels accurately. Load cells with adequate sensitivity do not have high enough load capacity to avoid damage upon needle insertion. A flexural based deflection method, as shown in Figure 83, provides a solution, where force is extracted from displacement measurements using a laser interferometer. The flexural beam deflects when the probe is inserted into the tissue section or surrogate agar model. The laser interferometer has a resolution of 1 nm and noise level of around 20 nm.

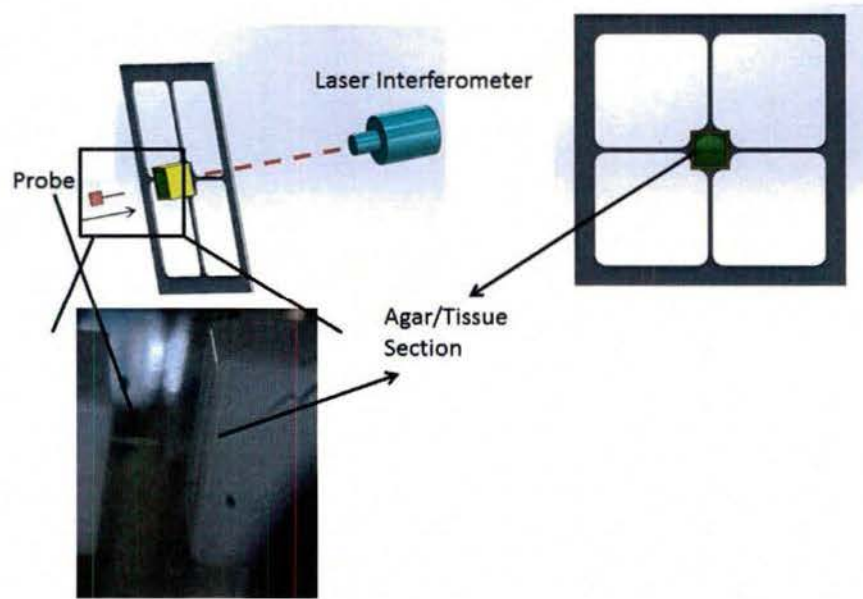


Figure 83. Custom-made flexural beam sensor for measuring needle insertion forces

Substrate deflection during insertion is generally more than  $1\ \mu\text{m}$ , corresponding to sensor sensitivity to measure forces to better than 2% accuracy. Separate calibration measurement of the stiffness of the beam is obtained using a load cell as shown in Figure 84(a). Figure 84(b) is a force-displacement plot indicating the stiffness of flexural beam.

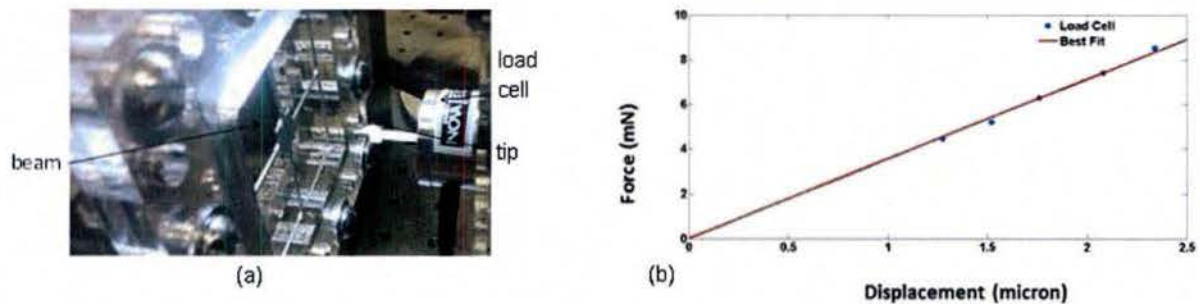


Figure 84. (a) Calibration by pressing a tip attached to a load cell to deflect the flexure. (b) Calibration curve for determining the stiffness of beam ( $3.52\ \text{mN}/\mu\text{m}$ ).

#### 7.5.4.2 Preliminary insertion studies

Figure 85 gives results of CMC/glucose needle insertion force into surrogate agar substrate (0.8% w/w) at three insertion speeds: 5 mm/s, 15 mm/s and 25 mm/s. The needle is  $240\ \mu\text{m}$  wide,  $150\ \mu\text{m}$  thick and 5.5 mm long. The insertion depth is around 4.5 mm, however data at distances greater than 3.5 mm are removed since the needle decelerates in that regime as an artifact of the setup. At lower insertion speed, the insertion force is lower owing to viscoelastic behavior of the agar model. There are two distinct regions: (1) pre-penetration elastic deformation of the tissue at distances below 0.4 mm where the force increases linearly for all velocities and (2) post-penetration where there is a slight decrease in force due to elastic recovery and then the force increases again as the probe shank progresses further into the agar.



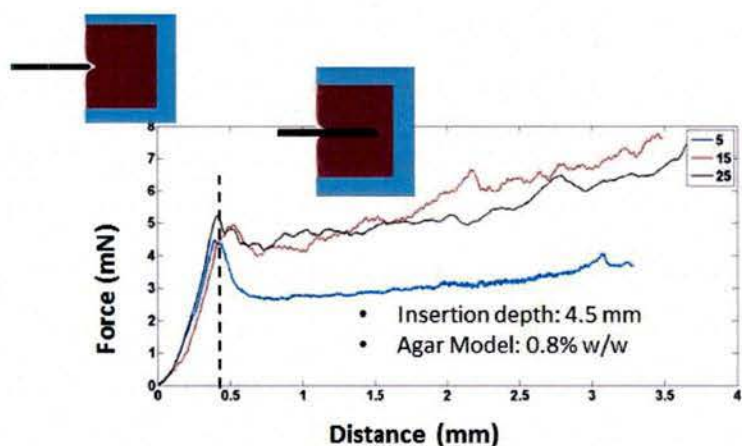


Figure 85. Preliminary insertion force measurements at different velocities.

This preliminary study shows that the probe can be inserted even at low speeds and at low force. A more comprehensive study of the needle design space for width, thickness, insertion speed, apex angle and tip sharpness employed hard polymer needles as surrogates for CMC/glucose needles to create a baseline of information related to the insertion of various shaped needles of the same scale as the probe needles. The best insertion results then inform the shape of the molded CMC/glucose needles. The surrogate needles are micromachined from a 100  $\mu\text{m}$ -thin PMMA sheet.

Figure 86 is a sample force-insertion profile obtained for a 300  $\mu\text{m}$ -wide probe with a 30° apex angle for speeds of 1, 3, 5, 10, 15, and 20 mm/s. The overall force increases as the needle penetrates into the agar. The force is larger as the insertion speed increases. Dimpling occurs in the first 350  $\mu\text{m}$ , transitioning at about the same distance for all the speeds. However, at higher speeds, the maximum dimpling force is higher; this effect is probably caused by strain hardening. Post dimpling there is reduction of force seen in all the force profiles. The rate of increase of force in the next region, where the needle tip starts to penetrate into the agar, is roughly constant with distance (*i.e.*, insertion force is roughly linear with displacement). In the final region, where the needle tip is completely inside the agar, the rate of increase in force is also roughly constant, but at a lower value than in the previous region.

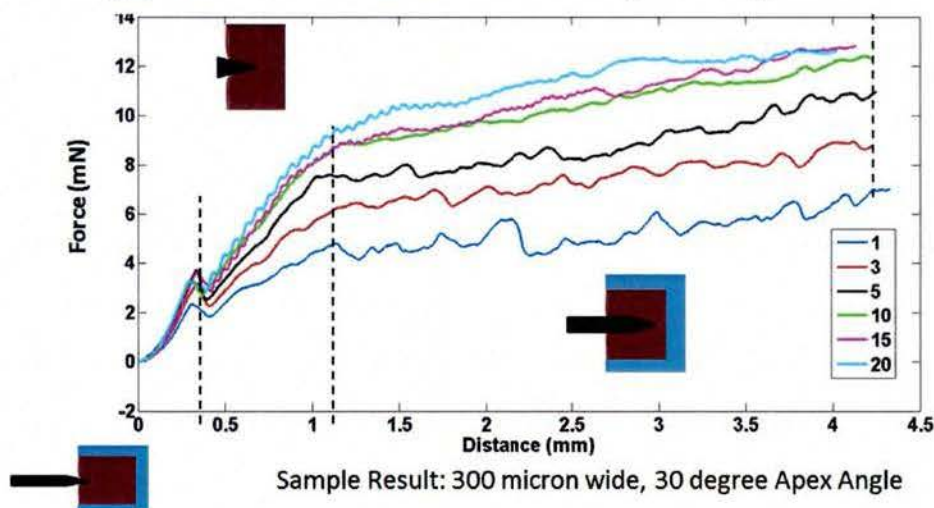


Figure 86. Sample force profile for surrogate PMMA needles penetrating agar. Varying insertion speeds are given in the legend in units of mm/s.

Similar tests were carried out with 130  $\mu\text{m}$ -wide and 200  $\mu\text{m}$ -wide probes with different apex angles, as shown in Figure 87. These probes showed a similar trend with respect to insertion speed. All the probes could be inserted at tested speeds from 1 mm/s to 20 mm/s. Forces are higher at higher insertion speeds for all probe sizes.

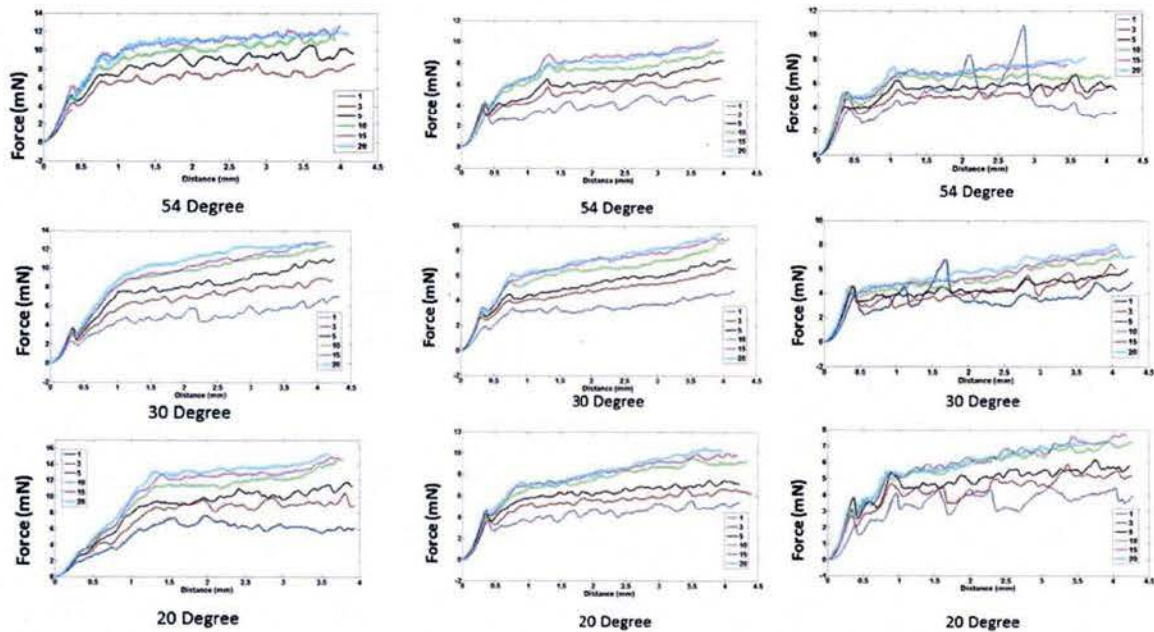


Figure 87. Insertion force profiles for PMMA probes with widths of 300  $\mu\text{m}$  (left), 200  $\mu\text{m}$  (middle), and 130  $\mu\text{m}$  (right). The apex angles are annotated below each plot. Varying insertion speeds are given in the legend in units of mm/s.

## 7.5.5 Insertion into sciatic nerve tissue

### 7.5.5.1 Surrogate needle insertion studies

For these tests, fresh sciatic nerve tissue is extracted from goat within 3 hours after the animals had been killed. The nerve tissue is cut into appropriate length and potted between 25% gelatin as shown in Figure 88. The gelatin ensures that tissue is held in place during insertion without requiring any mechanical components to hold the nerve. The setup also provides flexible boundary conditions that allow the tissue to compress and dimple which is typically seen during tissue insertion.

Figure 89 shows the force vs. distance profile of a surrogate 2D needle being inserted into sciatic nerve tissue at two different speeds (25 mm/s and 35 mm/s). The brass alloy 360 needle is 200  $\mu\text{m}$  thick, 300  $\mu\text{m}$  wide, with a 40° apex angle at the tip. The needle has a wedge shaped tip with the wedge as wide as the needle shank (*i.e.*, 300  $\mu\text{m}$ ). Multiple insertions were carried out at each speed. At each speed, no discernible change in force profile could be identified, indicating that the needle failed to insert into the tissue. Also, no stab wounds were observed under microscope examination. The needle dimples the nerve tissue and, in conclusion, a sharper tip is required for insertion.

A prototype needle design with a sharper tip has, along with an apex angle, a side angle to create a 3D sharp tip. The prototype needle is 330  $\mu\text{m}$  wide, 200  $\mu\text{m}$  thick and with a reduced wedge width of 30  $\mu\text{m}$ . The apex angle is 30° and side angle is 12°. Photos of the needle in Figure 90 verify the design geometry.



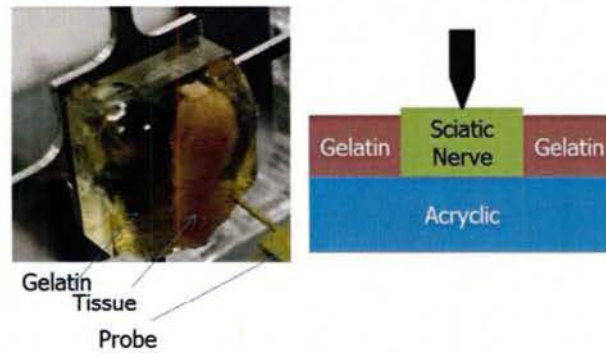


Figure 88. Photo (left) and schematic (right) showing insertion of a brass needle into *ex vivo* sciatic nerve tissue.

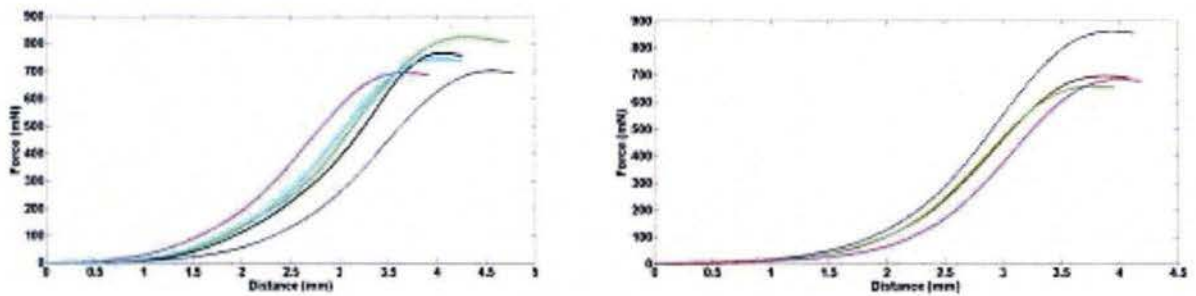


Figure 89. Force-insertion distance profile into sciatic nerve tissue. Left: 25 mm/s. Right: 35 mm/s. X-axis range is 0 to 5 mm. Y-axis range is 0 to 900 mN.

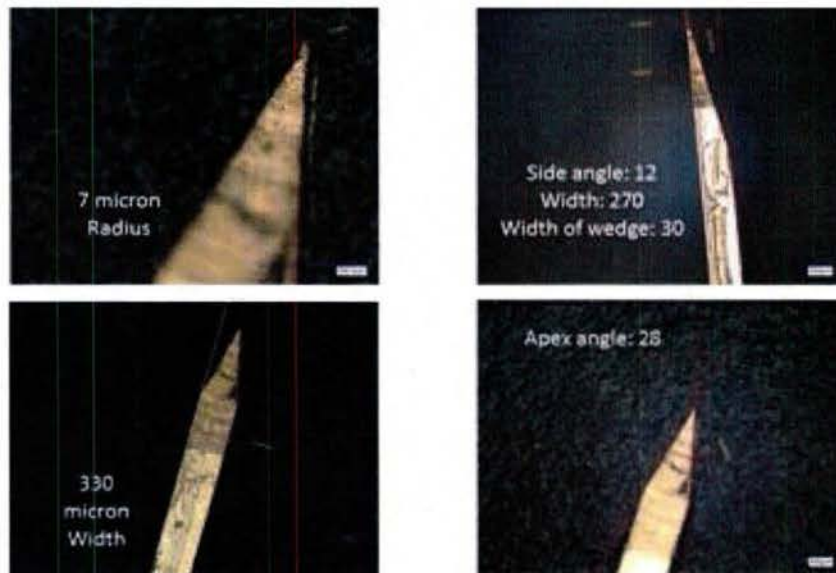


Figure 90. Side views of the prototype 3D brass needle for geometric characterization.

Figure 91 is the force profile during 15 mm/s insertion of the brass needle into the sciatic nerve tissue. The probe penetrates the tissue and inserts successfully. Multiple trials at the same speed demonstrate that the insertion is repeatable. Significant 800  $\mu\text{m}$ -deep dimpling occurs prior to tip penetration into the tissue. These results show the necessity of a sharp 3D tip.

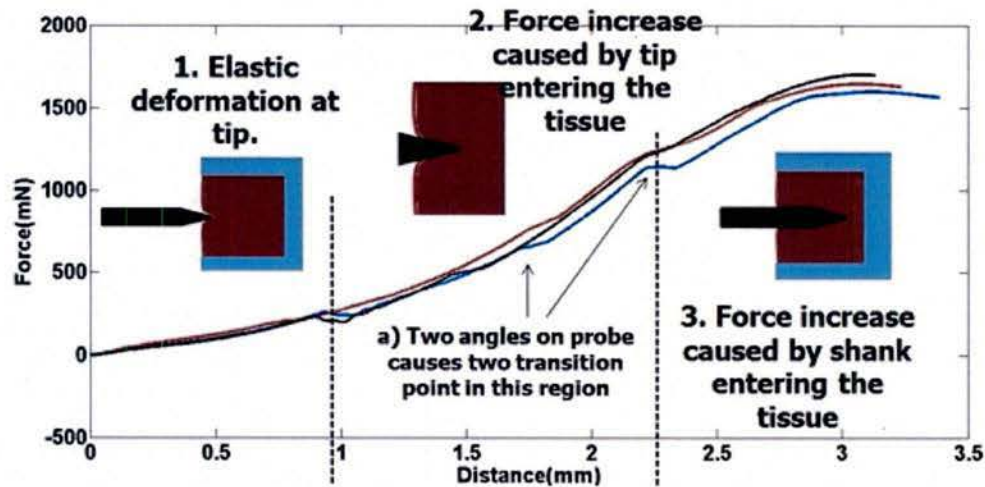


Figure 91. Force profile during insertion of a brass needle with 3D tip geometry into sciatic nerve tissue.

#### 7.5.5.2 CMC/glucose needle insertion

Figure 92(top) shows the optical image of a CMC/glucose needle molded with a 3D tip to facilitate insertion into tissue. Insertion with CMC needles was carried out to validate the hypothesis that the 3D sharp tips would enable insertion with CMC similar to the brass surrogate needle. Figure 92(bottom) shows the force profile during insertion at insertion speeds of 5 mm/s and 25 mm/s. The slip profiles illustrate that the CMC needles insert into the tissue with similar dimpling as the brass surrogate. The tip geometry is the primary factor governing insertion rather than the needle material.

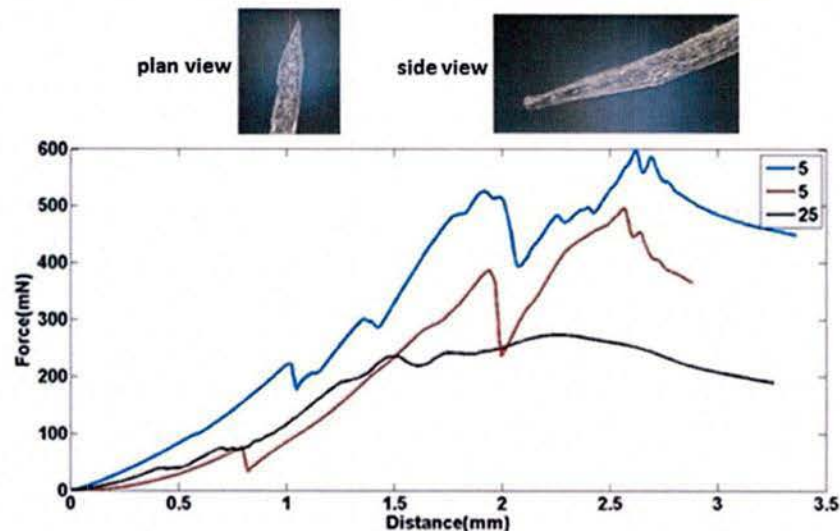


Figure 92. Optical images (top) and force profile (bottom) during insertion of CMC needle with a 3D tip. Speeds are 5 mm/s and 25 mm/s.



### 7.5.5.3 Surrogate phantom model insertion experiments

Experiments on nerve tissue show wide variation in the force profile. In addition, it is logistically difficult to obtain fresh sciatic nerve tissue regularly. Therefore, experiments were carried out using three different materials as possible surrogate phantoms to the sciatic nerve tissue for further insertion modeling studies. The first surrogate material system is a 350  $\mu\text{m}$ -thick PDMS layer layered on top of a 7% agarose gel. The second surrogate material system is a 10% mix ratio PDMS cast as a uniform layer. The third surrogate material system is a 10% mix ratio PVS (poly vinyl siloxane) cast as a uniform layer. From Figure 93, comparing the three force profiles, the PVS phantom has an insertion force profile closest to sciatic nerve tissue. However, the mechanism of penetration during insertion of such elastomer might be different from that of tissue. Hence, further validation studies are necessary before PVS should be chosen as a phantom model for sciatic nerve tissue.

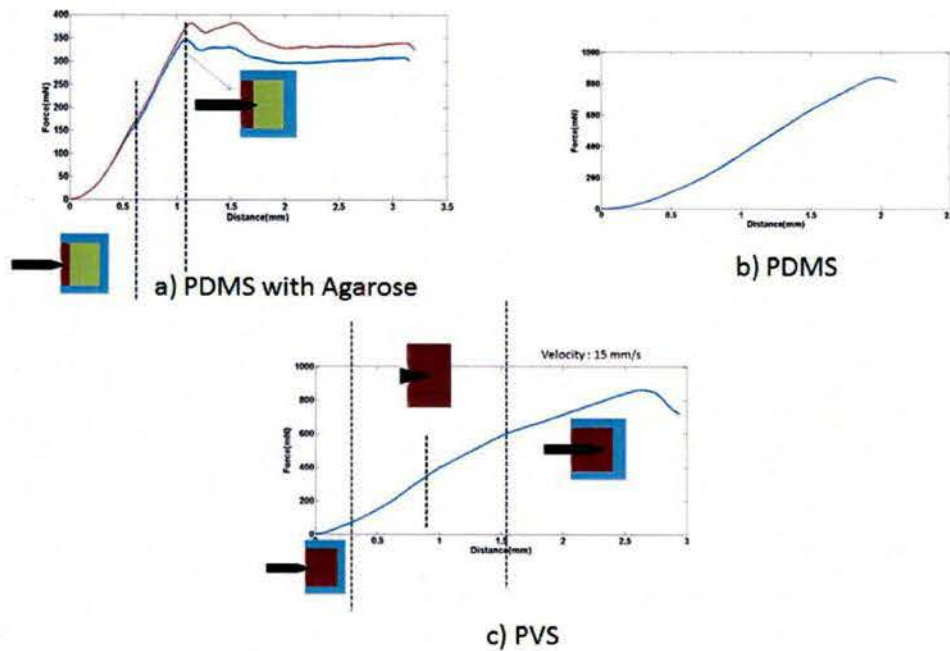


Figure 93. Force profiles of needle insertion into three different phantom models. (a) PDMS with agarose. (b) 10% mix ratio PDMS. (c) 10% mix ratio PVS.

### 7.5.5.4 Needle-probe assembly insertion and probe retention

Three trials tested insertion of CMC/glucose needles with attached wired probes into sciatic nerve tissue. The platinum wiring within the probe includes a self-testing feature comprising a closed electrical loop that allows *in situ* measurement of resistance during insertion to check wire continuity. Figure 94 shows the schematic of the insertion setup (left) and an optical image of the probe side profile and tissue while it is being referenced from the surface of the tissue (right).

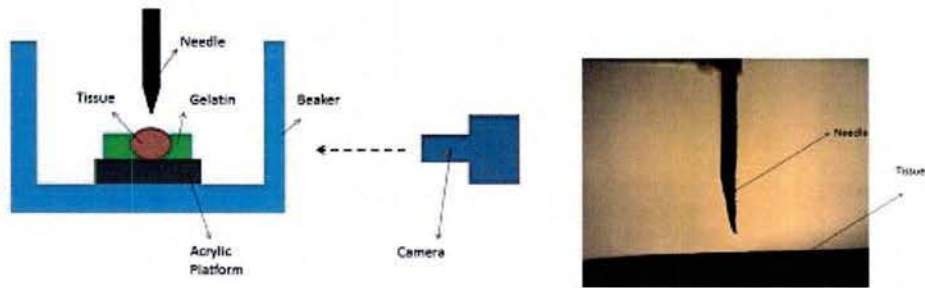


Figure 94. Schematic of the insertion setup (left) and optical image showing the reference of needle with the tissue (right).

Figure 95 provides the measurement results of electrical current through the loop before, during, and after insertion for one of the trials. The non-zero and relatively constant current at all time-points demonstrates that the probe wiring remains intact during insertion and provides an initial validation of the insertion procedure. Drops of water added at the top of the CMC/glucose needle where it penetrated the tissue accelerate the needle dissolution.

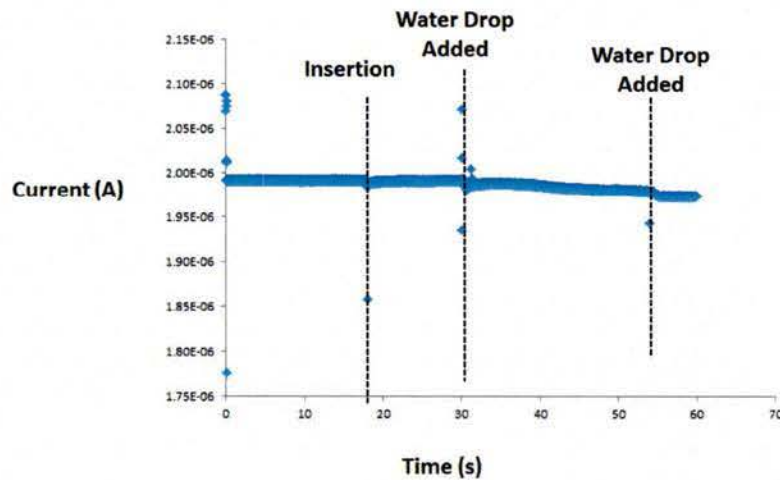


Figure 95. Measurement of electrical current during and post insertion.

The CMC needle creates a stab wound, as shown at the tissue surface in the microscope optical images in Figure 96. The CMC is dyed to enhance the contrast between the tissue and the needle. The needle penetrated the tissue and the wires are seen at the surface of the probe. It is not possible to see into the tissue using an optical microscope.



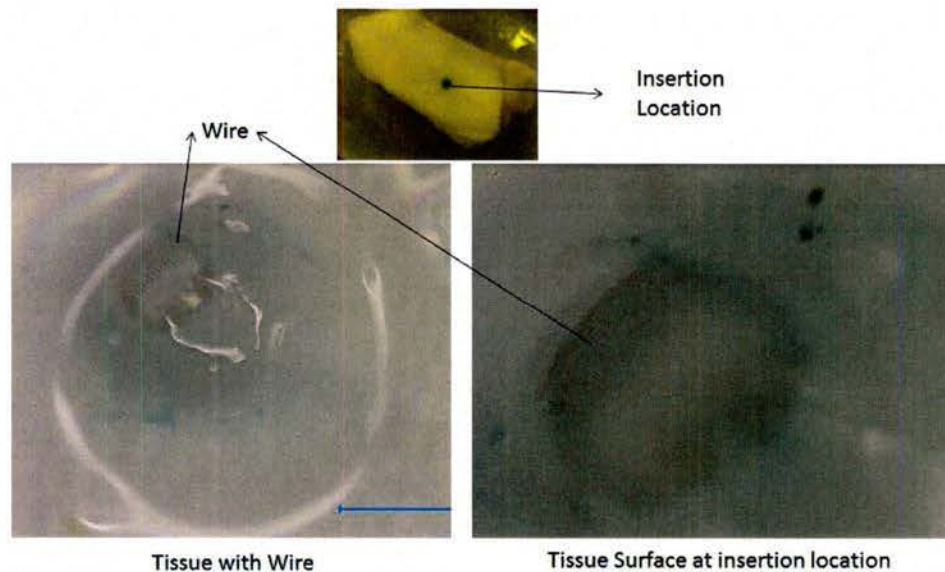


Figure 96. Optical Image of stab wound post insertion with wires.

In order to confirm that the probe can be successfully inserted into the peripheral nerve tissue using a CMC/glucose delivery needle, nano-resolution computer tomographic (Nano-CT) imaging is used post insertion. Nano-CT imaging provides contrast between the tissue and Pt wires for tissue depths up to 3 mm. The orientation in which CMC needle is inserted with respect to the tissue as well as the viewing direction in the Nano-CT instrument is illustrated in the schematic in Figure 97. A 15 mm-long and 4 mm to 5 mm-wide tissue sample is used for this insertion study. The CMC needle is mixed with a dye (India ink) to determine the location of insertion in order to align the instrument, as contrast between natural CMC and tissue is negligible. The insertion speed is set at 15 mm/sec and the nominal depth of insertion is 3 mm. The thickness of needle is 200  $\mu\text{m}$  and width of 300  $\mu\text{m}$ . The needle has a 3D tip with an apex angle of  $30^\circ$  and side angle of  $12^\circ$ . Post insertion, the tissue is frozen at  $-20^\circ\text{C}$  overnight. The tissue length is cut down to approximately 3 mm as shown by the dotted lines in Figure 97 in order to get appropriate contrast during CT imaging.

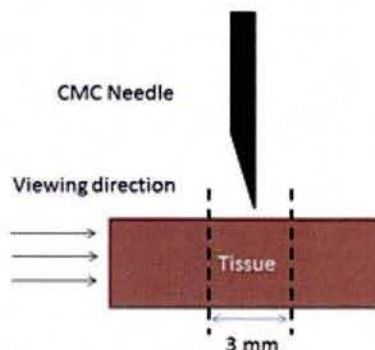


Figure 97. Schematic indicating the orientation of the needle with respect to the tissue sample and the viewing direction in the Nano CT equipment.

Figure 98 shows the optical and the Nano-CT image at the region of interest. At the top of the image, the Pt wires can be seen protruding above the surface of the tissue. Some dimpling curvature appears at the location of insertion. The wires appear to terminate at the tissue surface as the contrast between the Pt/air is different from Pt/tissue.

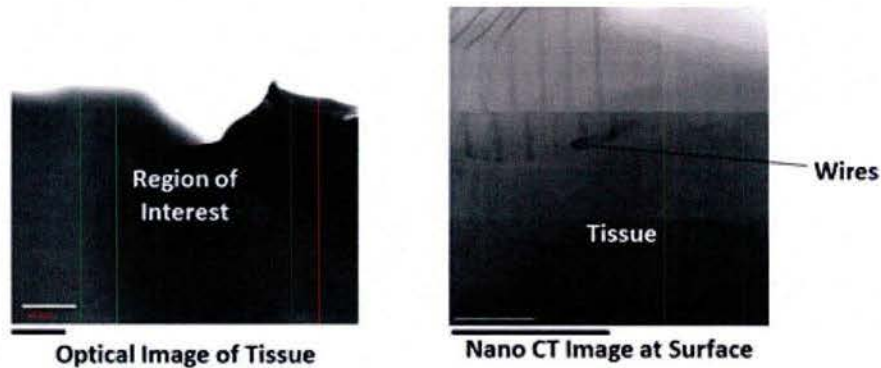


Figure 98. Left: Optical image showing region of interest. Right: Nano-CT image at the tissue interface (scale bars: 100  $\mu\text{m}$ ).

In order to see the wires inside the tissue, only tissue is imaged, eliminating air in the background. Figure 99 is a set of representative Nano-CT images inside the tissue. The needle schematic in Figure 99 describes the orientation with respect to the Nano-CT image. The electrodes, loops and the wires are visible just above the electrodes. The image is taken as a collage by stitching smaller images, and there is some misalignment in the collage image. However, the imaging verifies that the CMC needle successfully delivers the probe inside the nerve tissue. Note that the wiring does not take a rigid shape after insertion, but rather conforms to the tissue as it closes around the stab wound after needle dissolution.

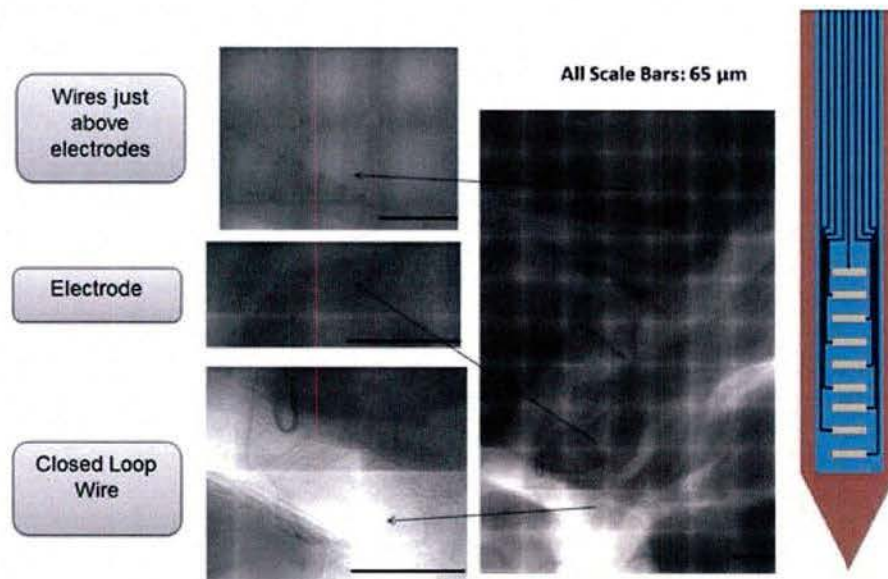


Figure 99. Nano-CT image showing wires, electrode and self-test loop. The right-hand-side schematic needle image shows the orientation of the needle w.r.t the Nano-CT image.



## 7.5.6 Experimental force modeling

### 7.5.6.1 Isolating different insertion force regimes

Figure 100 shows the experimental design to isolate different force regimes in order to analyze different forces associated during the insertion process. This approach is performed to better understand the relative contribution of different forces involved, and how they change with respect to different insertion conditions. Further, the measurements also provide an understanding of which forces are in effect during vibration assisted insertion when the other insertion conditions remain the same. A model of fixed thickness (3 mm) phantom tissue (2% agar) is used and insertion of a PMMA needle is performed. The insertion profile elucidates different force regimes and in particular it demonstrates separation of the friction force from the cutting force, which will help model the vibration assisted insertion.

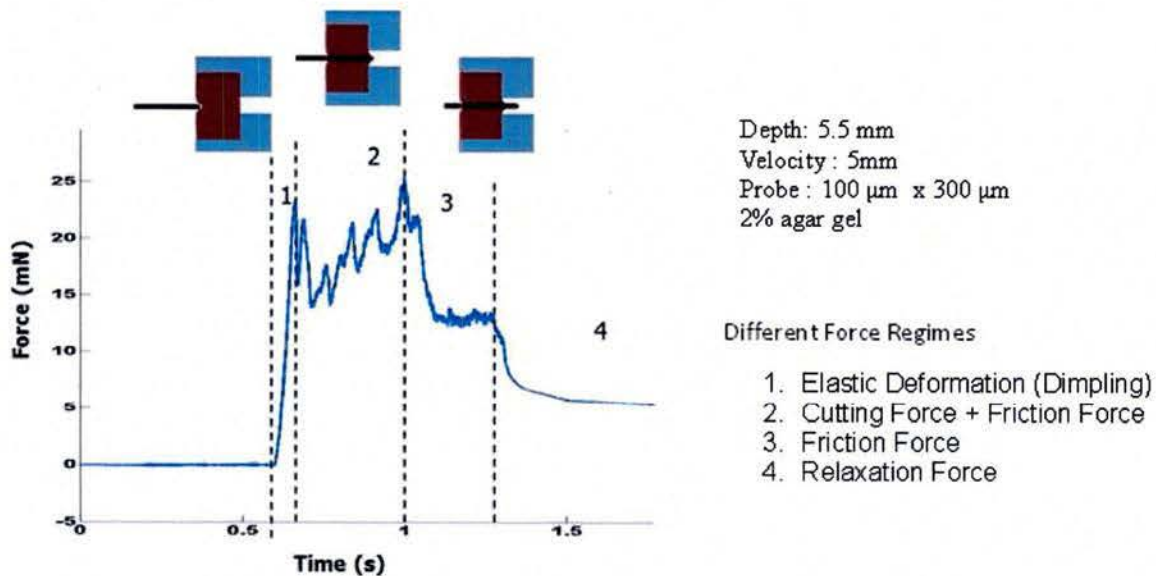


Figure 100. Experimental design to analyze and determine different force regimes during insertion process.

### 7.5.6.2 Repeatable preparation of agarose as a phantom model

Agarose phantom models for the prior insertion studies employed a manual cutting method to create a surface without 'skin'; however, this method resulted in an uneven surface with non-uniform substrate thickness. A new method, shown in Figure 101, creates a phantom model of agarose with a uniform thickness and smooth flat surface without formation of any stiff 'skin' at the top surface. Once the hot agarose solution is poured into the ABS container, the exposed surfaces are covered with glass slides to prevent further evaporation of moisture from the surfaces. The glass slides also ensure that the surfaces form uniformly and without defects. Informal repeatability tests, with example results shown in Figure 102, include both regular insertion tests and tests with fixed thickness of agarose.

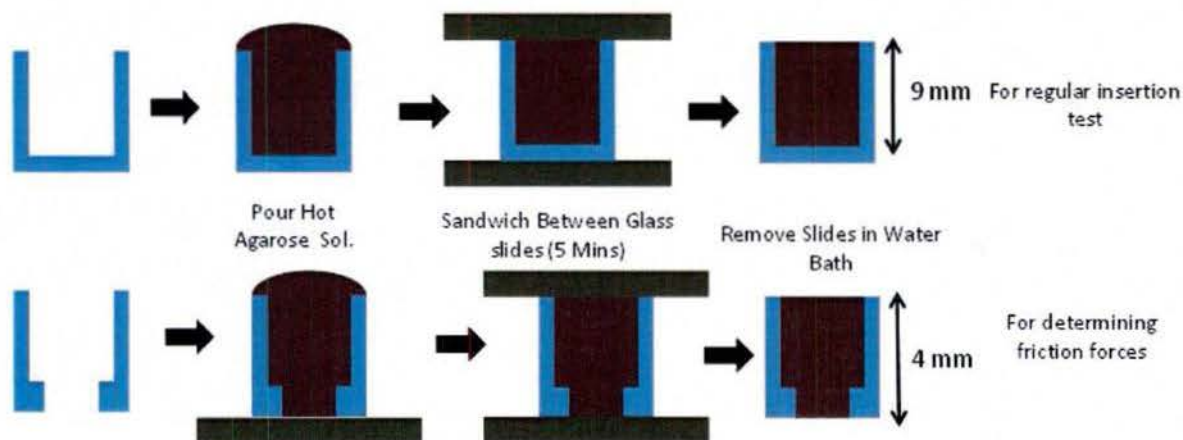


Figure 101. Modified agar sample preparation for both regular insertion tests and also for fixed thickness agarose tests.

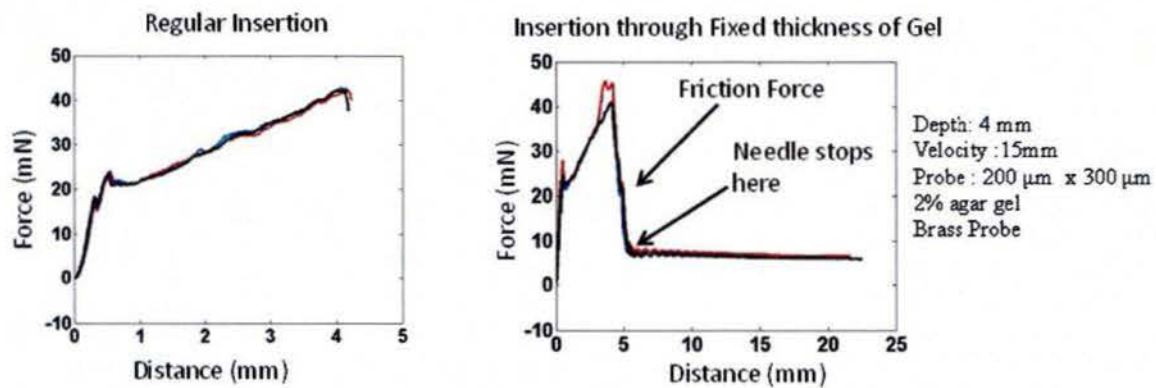


Figure 102. Example repeatability studies to evaluate the new sample preparation method.

### 7.5.6.3 Insertion force evaluation at different insertion velocity

Needle insertion into agarose substrate samples of three thicknesses (2 mm, 2.5 mm and 3 mm) at 15 mm/s provides a means to extract friction forces during insertion by performing needle penetration completely through the known thickness of agarose. The resulting force profiles in Figure 103(left) overlap up until the needle exits from the other side of the agarose sample, showing a linear relationship between friction force and agarose thickness, which was expected. The force profile after the needle exits the agarose surface is nearly horizontal and shows that it is a good indicator of the friction forces and the values are again proportional to thickness of agarose.

In Figure 103(right), the force profile of needle insertion into a 3 mm-thick agarose sample quantifies the effect of needle velocity on friction force. The friction force is the same (around 7.7 mN/mm) at 15 mm/s and 25 mm/s, while at 5 mm/s the friction force is lower (around 5.7 mN/mm). When there is a tissue dragging phenomenon, the tissue may tear but in turn reduces the contact surface area and could be the cause of lower friction at lower insertion speeds. However, once a sufficiently high velocity is obtained, the absence of the tissue dragging effect leads to a constant friction force as is evident by similar slopes during needle insertion at velocities of 15 mm/s and 25 mm/s.



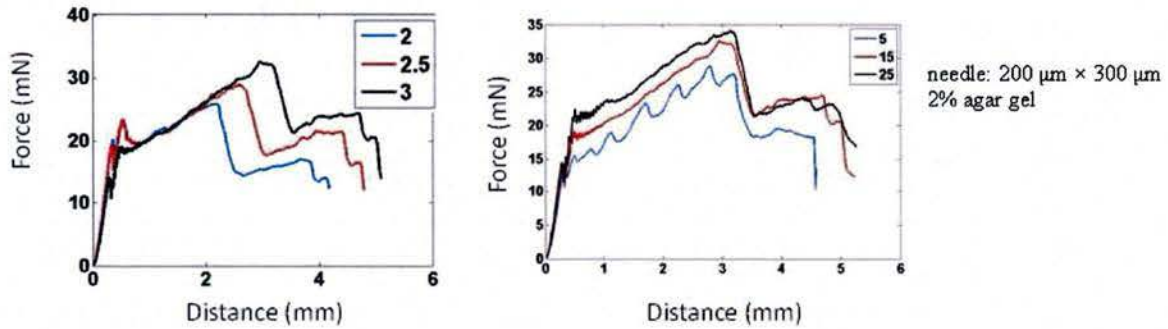


Figure 103. Force vs. insertion distance profiles to extract needle sidewall friction forces. Left: needle insertion at 15 mm/s into agarose sample thicknesses of 2 mm, 2.5 mm and 3 mm. Right: needle insertion into a 3 mm-thick agarose sample with speeds of 5 mm/s, 15 mm/s and 25 mm/s.

In order to model the cutting (shear) forces from tip penetration, a mechanistic model is developed similar to that used in machining processes. The cutting forces are correlated to either the area of the incision made by the needle tip or, in case of elastic tissue, cutting forces are correlated to the width of the tear made during incision. Two insertions are made one following after the other in the same location, with the difference in the force profile equaling the tearing/cutting force. From the result in Figure 104, the magnitude of the zero-slope force profile of Y-Y' is considered as the shearing/cutting force (around 13 mN in this case). However, this method needs further validation with more experimentation to check if such a mechanistic modeling properly captures the shearing/cutting process.

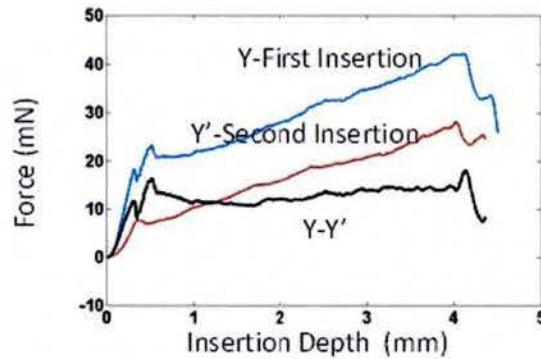


Figure 104. Extraction of cutting force via successive insertion on the same spot for force modeling.

Figure 105 shows the force signature during tip insertion and the variation of mechanistic slope parameters K1 and K2 associated with elastic deformation and tip penetration respectively. These graphs support the overall force modeling by curve fitting relations to needle velocity and needle geometry. The forces obtained at needle velocities from 0.5 mm/s to 20 mm/s indicate that the slope parameters increase with an increase in velocity, which is attributed to the viscoelastic behavior (strain rate hardening) of the agarose sample.

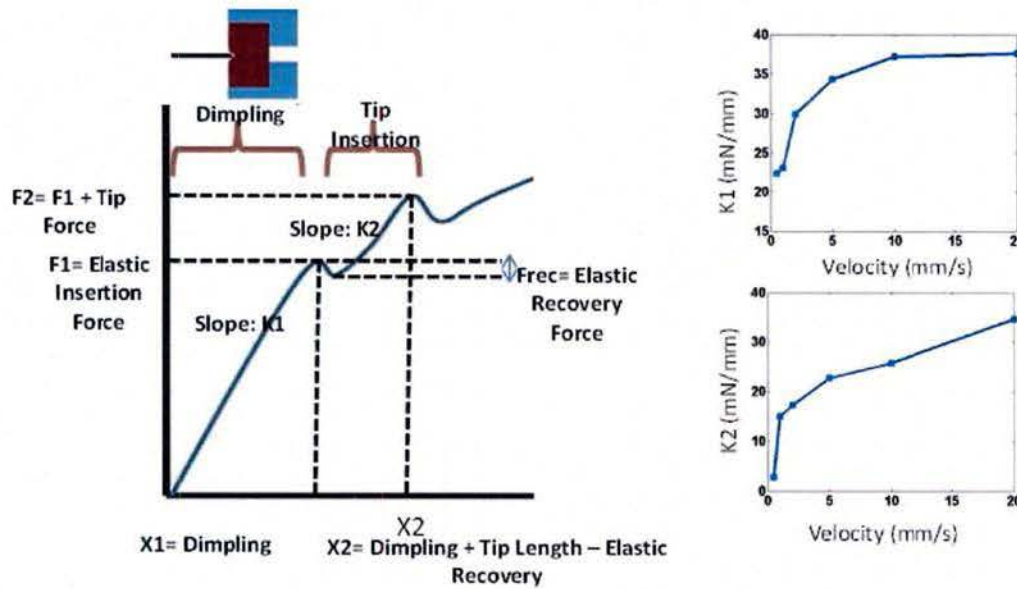


Figure 105. Modeling of tip insertion force including dimpling during elastic deformation.

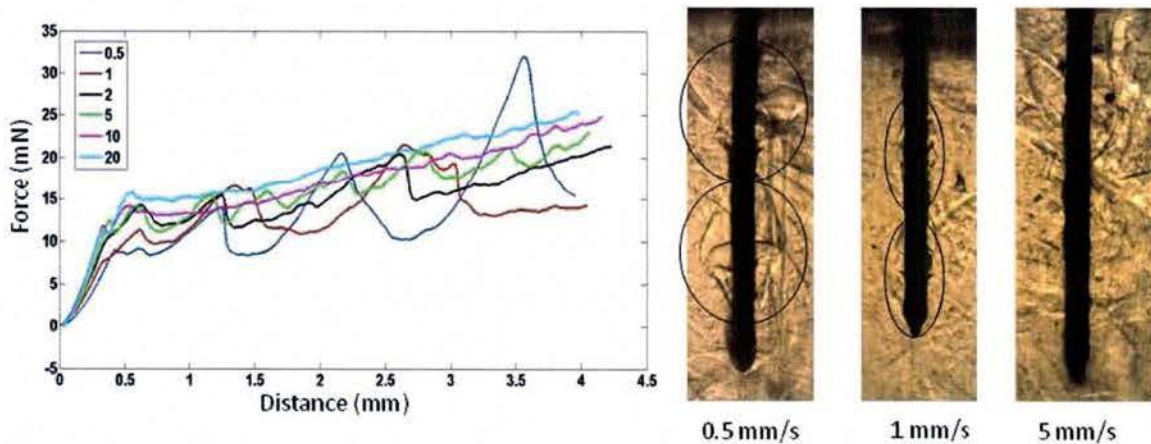


Figure 106. Relationship between measured force profile (left) and observed tissue damage on phantom tissue (right) at different velocities (inset legend in units of mm/s).

#### 7.5.6.4 Correlating insertion forces with phantom tissue damage

Insertion experiments were recorded using a side view camera in order to understand the 'tissue dragging' effect at low speeds and to validate optically the force effects seen in the force-distance plots. The results are recorded in Figure 106. The needle sticks to the agarose and creates a large volume of damage to the surrounding agarose at low speeds. As the speed is increased, such damage to surrounding agarose decreases and is not observed at speeds above 5 mm/s. The damage to the agarose is correlated to the peak-to-peak magnitude of the force waveform and inversely correlated to the frequency of the force waveform after tip insertion. The larger the peak-to-peak force amplitude, the lower is the spatial frequency and the larger is the damage to the agarose surrounding the needle. Hence, lower average forces do not necessarily correspond to lower agarose damage, and the peak-to-peak amplitude of the waveform plays an important role in determining the damage in the surrounding agarose. After reaching a sufficiently high needle velocity, oscillations in the force profile disappear and damage to surrounding material is no longer



observed. Therefore, there is a 'sweet spot' in terms of optimal insertion velocity where agarose damage is minimized and simultaneously where the forces are not high enough to cause failure of the needle due to bending or breaking.

### 7.5.7 Vibration assisted insertion

As discussed in section 7.5.6.4, at low insertion speeds into phantom tissue (agarose), the needle drags the tissue and creates a large volume of damage to the surrounding tissue. As the speed is increased, such damage to surrounding tissue decreases and is no longer observed above 5 mm/s. Literature suggests that at low speeds the 'tissue dragging' effect can be reduced if the insertion device is oscillated at high frequency such that the oscillating speed is much larger than the linear speed.

A piezoelectric stack actuator (piezo-actuator) was explored in an attempt to assess vibration assisted insertion. Due to dynamics of the piezo-actuator, the displacement at the tip varies with respect to the frequency for a given voltage. Hence, it is important to compensate for the dynamic effect of the piezo-actuator by modifying the drive voltage at each frequency to ensure equal displacement at all frequencies. Assuming the piezo-actuator stack has a linear drive voltage relationship when the frequency is fixed, the compensated voltage is proportional to the inverse of the frequency response function (FRF) of the piezo-actuator stack when the drive voltage is constant. However, since the displacement-voltage relation is not perfectly linear, multiple iterations are necessary to obtain a flat FRF with the compensated voltage as shown in Figure 107.

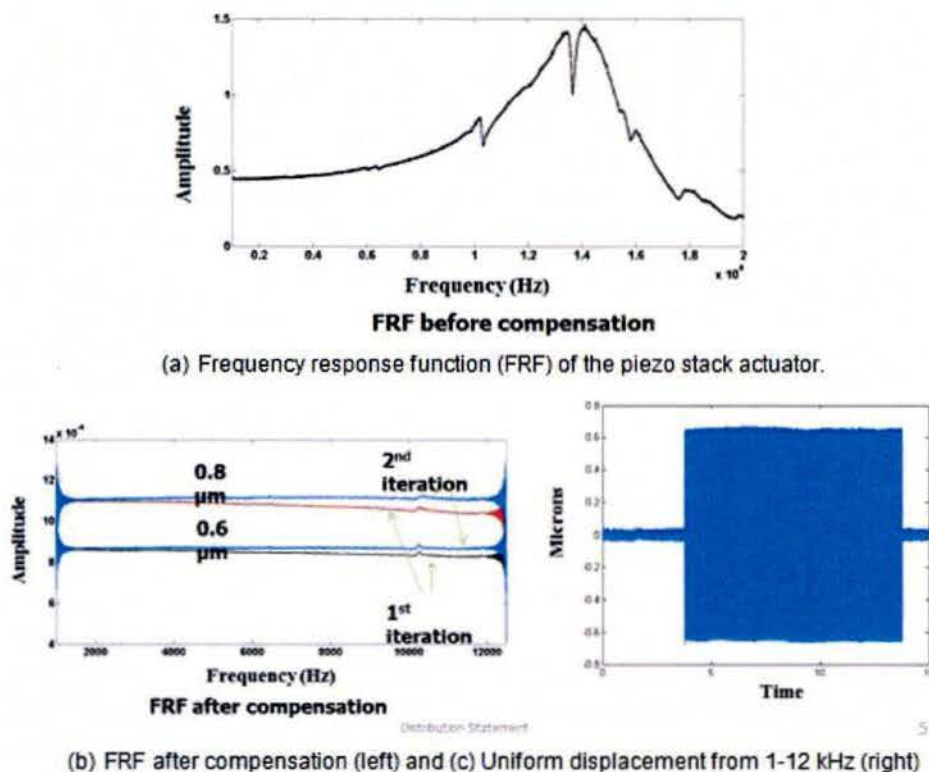


Figure 107. Compensation using frequency response function (FRF) data to obtain same displacement for all frequencies. (a) Uncompensated frequency response function under constant drive voltage. (b) Compensated frequency response function. (c) Displacement with a compensated chirp drive.

However, the maximum displacement of 1.2  $\mu\text{m}$  peak-peak from the piezo-actuator is too low at even at 10-13 kHz to cause a change in insertion force as compared to static insertion forces as shown in Figure 108. Similar results occur at 1 kHz, 2 kHz and 5 kHz vibrational drive frequencies.

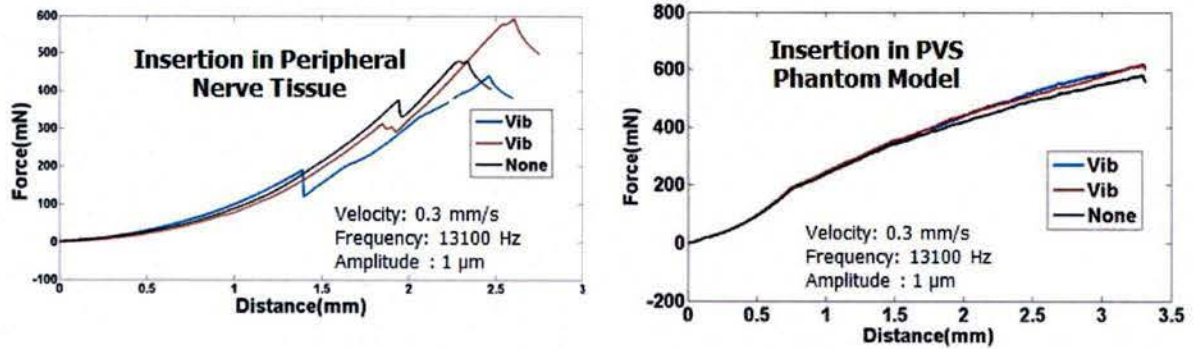


Figure 108. Insertion force comparison with and without vibration assistance in both sciatic nerve tissue and PVS phantom model.

Bolt-clamped Langevin type transducers (BLTs) may obtain higher amplitudes at ultrasonic frequencies and provide sufficient displacements necessary for reducing the insertion force. BLTs offer high displacement at high frequencies that are not simultaneously possible with piezo-actuator stacks. However, these transducers provide high displacement only at their resonant frequency, which makes them effective only at a single frequency. Hence, different transducers are required for different frequencies to conduct a study on effect of vibration frequency on insertion force. A laser interferometer (SIOS Meßtechnik GmbH) is used to measure the displacement of the transducer and obtain the frequency response function. A high current and high power amplifier obtains the relatively large displacement deemed necessary for vibration assisted insertion.

A shift in resonant frequencies is observed due to imperfect (*i.e.*, not fixed) boundary conditions. At high vibrational amplitudes, the clamping force provided by screws is not sufficient to hold the transducer properly. Dual resonant frequencies were observed at 32.8 kHz and 46 kHz. The amplitude at 46 kHz is higher than at 32.8 kHz for the same input voltage. Insertion experiments on 0.8% agarose and 1.5% agarose models were carried out at low insertion speeds (0.25 mm/s). The maximum tip velocity due to oscillation was measured at 120 mm/s at 32.82 kHz with a resonant bandwidth of 200 Hz. The results in Figure 109 show that no reduction in the 'tissue dragging' effect occurs when insertion was carried out using vibration assistance using this setup.

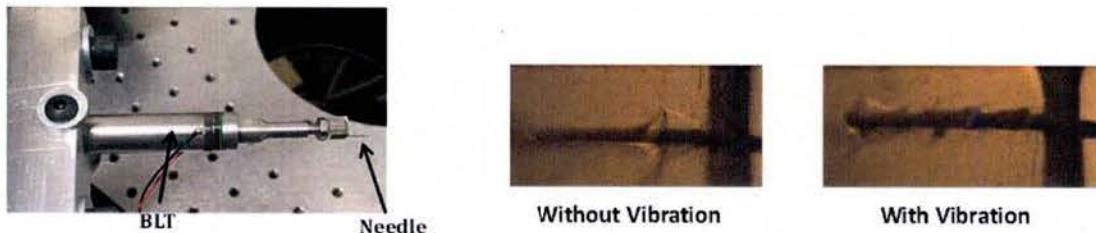


Figure 109. Needle mounted on BLT transducer for characterization and insertion. Insertion results in agarose gel do not show any improvement in tissue dragging using vibration assisted insertion.



However, we believe that due to the imperfect boundary conditions, we still do not have high enough amplitudes that are necessary to reduce the 'tissue dragging' effect. Further insertion experiments at higher vibration displacements need to be carried out using better clamped fixtures that can sustain such high vibrations.

## 8 Conclusions

Overall, the project achieved success in its major goal to provide a coupled design and fabrication technology for PNS multi-probe arrays that supports both recording and stimulation, is selective to specific fascicles, is scalable in electrode count and location to cover the entire cross section of major branches of the vagus nerve, has low invasiveness after insertion relative to competing intrafascicular probes, and whose functionality is validated through *in vitro* and *ex vivo* testing.

ALD interleaved alumina-titania nanolaminate achieves higher probe yield than parylene insulation alone and excellent (high) leakage resistance performance with a 4 month time constant from the starting leakage resistance of 26 G $\Omega$  at 37°C, which provides about two years of service above 1 G $\Omega$  leakage. Importantly, only the ALD ceramic encapsulated wiring was able to survive stimulation voltage cycling outside of the water window without bubbling creating damage to the probe. This success of ALD nanolaminates to insulate wiring in parylene substrates warrants further exploration of the materials and process space toward even better performance. Probe longevity beyond ten years is a useful mid-term research target, requiring about a five-fold improvement over the state-of-the-art performance in this project. Furthermore, future yield studies should measure a statistically relevant number of released flexible probes to generate confidence in their performance in practice.

The assembly method of attaching pre-molded dissolvable needles to probes that are transferred to a sacrificial handle substrate is successful in creating a viable path toward production of these custom probes for neural applications. Decoupling the needle molding from the probe fabrication enables the pre-molding of sharp 3D-tipped needles that prove essential for low-force insertion into tissue. The probe-needle assembly experiments in this project ended with successful feasibility tests. A logical next step is to perform more comprehensive yield tests.

The process flow to make iridium oxide (and platinum) protruding electrodes on the flexible parylene probes succeeded. A possible future next step is to develop a multi-level parylene process that enables taller protruding electrodes. Any such development should incorporate *in vivo* neural recording (and stimulation) tests to compare efficacy between regular and protruding electrodes in practice.

Needle insertion methods indicate that relatively high speeds (*e.g.*, 10 mm/s) minimize damage in an agarose phantom tissue model. Low insertion speeds (*e.g.*, below 5 mm/s) gives rise to stick-slip conditions that create tissue damage. Very high speeds (*e.g.*, above 10 mm/s) does not create tissue damage, but does increase overall insertion forces. The optimal insertion speed is around 10 mm/s for the needles fabricated in this project. A next step is to assess damage in true neural tissue as a function of needle insertion speed using best-in-class 3D-tipped needles.

The most likely potential consumers of these probe results will be researchers who wish to use advanced electrical recording and stimulation probes for electropharmaceutics and other forms of functional stimulation, with a path toward chronic applications. During the course of this project, our research team engaged with three neural researchers:

- Professor Aryn Gittis at Carnegie Mellon University for use of the probe technology for neural studies in rats

- Professor Rob Gaunt at the University of Pittsburgh on design of multi-shank PNS probes for eventual test in a cat model
- Professor Charles Horn at the University of Pittsburgh, connected to studies of PNS stimulation to control nausea

All of these interactions are continuing.

## 9 Patents and Invention Disclosures

- Invention Disclosure, “Nanolaminate insulated probes for neural recording and stimulation”, Inventors: Gary Fedder, Xiao Chuan Ong, Mats Forssell, Burak Ozdoganlar, Rakesh Khilwani, submitted June 30, 2017.
- Invention Disclosure, “Protruding neural electrodes”, Inventors: Gary Fedder, Xiao Chuan Ong, Mats Forssell, Burak Ozdoganlar, Rakesh Khilwani, in preparation.

## 10 Publications

### 10.1 Journal papers

- [1] Rakesh Khilwani, Peter J Gilgunn, Takashi DY Kozai, Xiao Chuan Ong, Emrullah Korkmaz, Pallavi K Gunalan, X Tracy Cui, Gary K Fedder and O Burak Ozdoganlar, " Ultra-miniature ultra-compliant neural probes with dissolvable delivery needles: design, fabrication and characterization," *Biomedical Engineering*, December 2016, 18:97.
- [2] Xiao Chuan Ong, Rakesh Khilwani, Mats Forssell, O Burak Ozdoganlar, Gary K. Fedder, “A transfer process to fabricate ultra-compliant neural probes in dissolvable needles,” *Journal of Micromechanics and Microengineering*, February 2017, 27:3.
- [3] Mats Forssell, Xiao Chuan Ong, Rakesh Khilwani, O. Burak Ozdoganlar, and Gary K. Fedder, “Insulation of multilayer parylene and ceramic films in saline solution”, In preparation

### 10.2 Thesis

The project funded the work of three Ph.D. students: Xiao Chuan Ong, Rakesh Khilwani, and Mats Forssell. All are continuing toward their degree and so no theses are available at time of this report.

### 10.3 Conference Papers

- [4] Xiao Chuan Ong, Mats Forssell, and Gary K. Fedder, “Processing of platinum electrodes for parylene-C based neural probes,” in *Proc. of the IEEE 29<sup>th</sup> Int’l Conference on Micro Electro Mechanical Systems*, Shanghai, China, Jan. 24-28, 2016 (4 pages). Paper presented as a poster and archived in IEEE Xplore.
- [5] Xiao Chuan Ong, Amanda Willard, Mats Forssell, Aryn Gittis, and Gary K. Fedder, “A silicon neural probe fabricated using DRIE on bonded thin silicon,” in *Proc. of the IEEE 38<sup>th</sup> Int’l Conference of the IEEE Engineering in Medicine and Biology Society*, Orlando, FL, Aug 16-20, 2016 (4 pages). Paper presented as a poster and archived in IEEE Xplore.